Measurement of Longitudinal Double Spin Asymmetries and Spin Structure Functions of the Deuteron in the CLAS EG1b Experiment

Nevzat Guler, Sebastian Kuhn

Analysis Note Submitted to CLAS Collaboration

December 1, 2012

ABSTRACT

This CLAS Analysis note describes the analysis and final results for the large data set collected by the EG1b experiment on deuterium. Longitudinally polarized electrons at energies 1.6 - 1.7, 2.3-2.5, 4.2 and 5.7 GeV were scattered from longitudinally polarized ND_3 targets. The double spin asymmetry $A_{\parallel}$ for the deuteron has been extracted in the valence region from these data as a function of W and Q^2 with unprecedented precision. The virtual photon asymmetry A_1 and the spin structure function g_1 can be calculated from these measurements by using parametrization to the world data for the virtual photon asymmetry A_2 and the unpolarized structure functions F_1 and R. The large kinematic coverage of the experiment (0.05 GeV^2 $<$ Q^2 $<$ 5.0 GeV^2 and 1.08 GeV $< W <$ 3.0 GeV) helps us to better understand the spin structure of the nucleon, especially in the transition region between hadronic and quark-gluon degrees of freedom. The results on A_1, g_1 and the first moment Γ_1^1, as well as the higher moments Γ_1^3 and Γ_1^5, using the entire data set for the deuteron, are presented in this note. In addition, parameterizations of the world data on the asymmetries and the spin structure functions are studied to create and refine the models on these quantities that can be used in various applications. Finally, the neutron asymmetries are extracted from the combined proton and deuteron data.

TABLE OF CONTENTS

LIST OF TABLES

LIST OF FIGURES

CHAPTER I

DATA ANALYSIS

This note describes the analysis of the EG1b experiment, focusing specifically on the deuteron data. Below, we list all the analysis steps taken to go from the raw data to the physics results. The EG1b proton data analysis and this analysis share many aspects. Therefore, for those common parts of the analysis, we are going to refer to the recently submitted proton analysis note [1] and only describe any differences. The following list enumerates the step by step analysis procedures and the items with bold-face will be described in more detail in the subsequent chapters.

1. **EG1b Run summary**
2. Data calibration and reconstruction
3. Helicity pairing
4. Quality checks and data selection - event rates, beam charge quality, effects of beam charge asymmetry, polarization and asymmetry checks, faraday cup corrections, raster.
5. **Data binning**
6. Particle identification - electron cuts, status flag, trigger bit, vertex cut, CC cut, EC cuts, additional kinematic cuts, sector 5 correction.
7. Geometric and timing cuts on the Cherenkov signal
8. Fiducial cuts
9. Kinematic corrections - raster correction, average vertex position, torus current scaling, beam energy correction, multiple scattering and magnetic field corrections, energy loss correction, momentum correction, patch correction, overall effect of kinematic corrections.
10. **Dilution factors**
11. Pion and pair symmetric background corrections
12. **Extraction of the beam $\times$ target polarization**

13. **Polarized background correction**
14. **Radiative corrections**
15. **Combining data**
16. **Models**
17. **Propagation of statistical errors for physics quantities**
18. **Systematic errors** - background corrections, dilution factor, beam x target polarization, radiative corrections, models
19. **Final results for the deuteron**
20. **Data parameterizations to model the world data**
21. **Extraction of the neutron structure functions from the combined proton and deuteron data**

A list of common variables often used for the description of an electron-nucleon scattering event is given in the following equations. It should be noted that the beam axis is defined in the $\hat{z}$-direction and the polar scattering angle is labeled as θ while the azimuthal angle is represented by ϕ.

$$Q^2 = -q^2 = 4EE' \sin^2 \frac{\theta}{2} = 2EE'(1 - \cos\theta) \tag{1}$$

$$\nu = E - E' = \frac{p \cdot q}{M} \tag{2}$$

$$W = \sqrt{(p+q)^2} = \sqrt{M^2 + 2M\nu - Q^2} \tag{3}$$

$$x = \frac{Q^2}{2p \cdot q} = \frac{Q^2}{2M\nu} \tag{4}$$

$$y = \frac{p \cdot (k - k')}{p \cdot k} = \frac{E - E'}{E} = \frac{\nu}{E} \tag{5}$$

$$\gamma = \frac{2Mx}{\sqrt{Q^2}} = \frac{\sqrt{Q^2}}{\nu} \tag{6}$$

$$\tau = \frac{\nu^2}{Q^2} = \frac{1}{\gamma^2} \tag{7}$$

$$\epsilon = \left(1 + 2(1+\tau)\tan^2(\theta/2)\right)^{-1} \tag{8}$$

$$\eta = \frac{\epsilon\sqrt{Q^2}}{E - \epsilon E'} \tag{9}$$

$$D = \frac{1 - \epsilon\frac{E'}{E}}{1 + \epsilon R} \tag{10}$$

where Q^2 is the squared four-momentum and ν is the energy of the virtual photon, W is the mass of final hadronic state, x is the Bjorken scaling variable and ϵ is the relative flux of the two polarization states of the virtual photon (ratio of longitudinal polarization to the transverse polarization). D is the depolarization factor that represents how much of the incoming lepton's polarization is transferred to the virtual photon. R is the ratio of longitudinal to transverse virtual photo absorbtion.

To summarize the overall analysis procedure: The double spin asymmetry $A_\parallel$ is obtained from the measured experimental asymmetry A_{raw} via,

$$A_\parallel = \frac{C_1}{f_{RC}}\left(\frac{A_{raw}}{F_D P_b P_t}\, C_{back} - C_2\right) + A_{RC} \tag{11}$$

where $P_b P_t$ is the product of beam and target polarizations, F_D is the dilution factor, which accounts for the scattering from the unpolarized components of the target, C_{back} represents the pion and pair symmetric background corrections, f_{RC} and A_{RC} take care of the radiative effects while C_1 and C_2 corrects for the contributions from the polarized background. The experimental asymmetry A_{raw} is defined by:

$$A_{raw} = \frac{n^- - n^+}{n^- + n^+} \tag{12}$$

where n^- and n^+ are determined by counting the inclusive scattering events for each helicity state and normalizing with the accumulated (live-time gated) beam charge (N_e) for that helicity state:

$$n^- = \frac{N^{\uparrow\downarrow}}{N_e^{\uparrow\downarrow}} \quad ; \quad n^+ = \frac{N^{\uparrow\uparrow}}{N_e^{\uparrow\uparrow}} \tag{13}$$

with arrows indicating the relative spin orientations of the electron and the target nucleus (or nucleon). The quantity A_{raw} is extracted for each kinematic bin in Q^2 and W in the resonance region and above, for each beam energy and detector setting separately.

I.1 EG1B RUNS

During the experiment, a longitudinally polarized electron beam of various energies ranging from 1.6 GeV to 5.7 GeV was incident on longitudinally polarized proton

(NH_3) and deuteron (ND_3) targets. This ensures a good coverage of the entire resonance region and above: 1.08 GeV $< W <$ 3.0 GeV; 0.05 GeV^2 $< Q^2 <$ 5.0 GeV^2. In order to increase the kinematic coverage, the torus current was also switched between inbending and outbending settings for some beam energies. In addition to the NH_3 and ND_3 targets, data on the ^{12}C target and the empty target (with only liquid Helium) were also collected for each beam energy and torus setting. These runs were used to estimate the unpolarized background contribution to the data. Occasional runs were also taken on pure ^{15}N target and used to monitor the effectiveness of the background removal procedure using the ^{12}C runs. Table 1 provides a simple summary of all runs taken together with corresponding beam and torus settings. Based on Table 1, we separated the data into different configurations and analyzed each set separately. We analyzed 11 different data sets for both ND_3 and NH_3 targets, which are listed in Table 2. At the end, the results from these sets were combined, as detailed later in this document

TABLE 1: EG1b run sets by beam energy and torus current.

Run Numbers	Beam Energy(GeV)	Torus Current(A)
25488-25559; 25669-26221	1.606	+1500
26222-26359	1.606	−1500
28512−28526	1.723	+1500
27644-27798; 28527-28532	1.723	−1500
27205-27351	2.286	+1500
28001-28069	2.561	+1500
27799-27924; 27942-27995	2.561	−1500
27936-27941	2.792	−1500
28074-28277; 28482-28494; 28506-28510	4.238	+2250
28280-28479; 28500-28505	4.238	−2250
27356-27364; 27386-27499	5.615	+2250
27366-27380	5.615	−2250
27069-27198	5.725	+2250
26874-27068	5.725	−2250
26468-26722; 26776-26851	5.743	−2250

TABLE 2: Analyzed data sets by target, listing the beam energy E_B and the torus current I_T. Throughout each data set, there are also occasional ^{12}C and empty target runs, used for background analysis.

$ND_3[E_B(\text{GeV}), I_T(\text{A})]$	$NH_3[E_B(\text{GeV}), I_T(\text{A})]$
1.606, +1500	1.606, +1500
1.606, −1500	1.606, −1500
1.723, −1500	1.723, −1500
2.561, +1500	2.386, +1500
2.561, −1500	2.561, −1500
4.238, +2250	4.238, +2250
4.238, −2250	4.238, −2250
5.615, +2250	5.615, +2250
5.725, +2250	5.725, +2250
5.725, −2250	5.725, −2250
5.743, −2250	5.743, −2250

I.2 DATA BINNING

The goal of our experiment is to determine asymmetries as a function of two kinematic variables: the squared four-momentum transfer Q^2 and the invariant mass W. Once we have extracted physics quantities as function of these two variables, we can express them as a function of any other pair of kinematic variables as well. Another common pair is (Q^2,x), where x is the Bjorken scaling variable. While converting the (Q^2,W) pair into (Q^2,x), we used kinematic values directly obtained from data, which are averaged over the amount of data observed for that specific kinematic bin. The W bins are 10 MeV wide. Binning in Q^2 is logarithmically calculated by using the formula:

$$\text{Bin Number} = n = \text{int}\left(13\log_{10}\left(\frac{Q^2}{C}10^{27/13}\right)\right), \tag{14}$$

where,

$$C = \frac{(1+10^{-1/13})}{2}\,. \tag{15}$$

From these equations, we can calculate Q^2_{min} and Q^2_{max} for each bin by using the following definitions:

$$Q^2_{min} = C \times 10^{(n-27)/13} \tag{16}$$

$$Q^2_{max} = C \times 10^{(n+1-27)/13} \tag{17}$$

Table 3 show the Q^2 bins of the EG1b data together with the minimum and maximum value for each bin. The table also shows the arithmetic and geometric average of each bin. All kinematical variables of interest (including W and Q^2, but also x, E', ϵ, η and D) were averaged over each bin, using the measured counts as statistical weight. Therefore, the average values of these kinematic variables don't necessarily agree with the values at the bin centers.

TABLE 3: Q^2 bins for EG1b experiment

Bin	Q2min	Q2max	geoAve	ariAve
1	0.009188388	0.010968883	0.0100	0.0101
2	0.010968883	0.013094397	0.0120	0.0120
3	0.013094397	0.015631785	0.0143	0.0144
4	0.015631785	0.018660860	0.0171	0.0171
5	0.01866086	0.022276898	0.0204	0.0205
6	0.022276898	0.026593641	0.0243	0.0244
7	0.026593641	0.031746867	0.0291	0.0292
8	0.031746867	0.037898668	0.0347	0.0348
9	0.037898668	0.045242545	0.0414	0.0416
10	0.045242545	0.054009494	0.0494	0.0496
11	0.054009494	0.064475272	0.0590	0.0592
12	0.064475272	0.076969073	0.0704	0.0707
13	0.076969073	0.091883882	0.0841	0.0844
14	0.091883882	0.109688832	0.100	0.101
15	0.109688832	0.130943966	0.120	0.120
16	0.130943966	0.156317848	0.143	0.144
17	0.156317848	0.186608595	0.171	0.171
18	0.186608595	0.222768982	0.204	0.205
19	0.222768982	0.265936407	0.243	0.244
20	0.265936407	0.317468671	0.291	0.292
21	0.317468671	0.378986684	0.347	0.348
22	0.378986684	0.452425451	0.414	0.416
23	0.452425451	0.540094935	0.494	0.496
24	0.540094935	0.644752718	0.590	0.592
25	0.644752718	0.769690734	0.704	0.707
26	0.769690734	0.918838820	0.841	0.844
27	0.91883882	1.096888321	1.00	1.01
28	1.096888321	1.309439656	1.20	1.20
29	1.309439656	1.563178475	1.43	1.44
30	1.563178475	1.866085950	1.71	1.71
31	1.86608595	2.227689819	2.04	2.05
32	2.227689819	2.659364071	2.43	2.44
33	2.659364071	3.174686710	2.91	2.92
34	3.17468671	3.789866839	3.47	3.48
35	3.789866839	4.524254507	4.14	4.16
36	4.524254507	5.400949352	4.94	4.96
37	5.400949352	6.447527179	5.90	5.92
38	6.447527179	7.696907344	7.04	7.07
39	7.696907344	9.188388200	8.41	8.44
40	9.1883882	10.968883209	10.0	10.1

I.3 DILUTION FACTOR

Since we are interested in scattering events from polarized nucleons, the asymmetries must be corrected for the contributions from unpolarized background. These contributions mainly come from the (nearly - see below) unpolarized ^{15}N nucleus in the target material (ND_3), the liquid helium bath that surrounds it for cooling and the target windows that keep the whole apparatus together. For this purpose, we define a quantity called dilution factor, which is the fraction of events scattered from the polarized deuterons. In order to explain the dilution factor better, we consider the raw asymmetry as described in Eq. 12. In this equation, n^- and n^+ are determined by counting the inclusive scattering events for each helicity and normalizing with the accumulated beam charge. During the counting procedure, we have no way to know if the event is coming from the polarized target or from the unpolarized background. However, since the unpolarized contribution is the same for both helicities, it cancels out in the numerator. The denominator, on the other hand, is heavily diluted by the background contribution. Therefore, we need to correct the denominator such that:

$$A_{undil} = \frac{n^- - n^+}{n^- + n^+ - n_B} \tag{18}$$

where n_B stands for the count of the background events. Based on this approach, we can define a dilution factor (F_D) to correct the asymmetry for the background contribution:

$$F_D = \frac{n^- + n^+ - n_B}{n^- + n^+} = \frac{n_A - n_B}{n_A} = 1 - \frac{n_B}{n_A}, \tag{19}$$

where n_A represents the total count of events from all sources in the beam path. Then we can write the undiluted asymmetry in terms of the diluted asymmetry and the dilution factor defined in Eq. (19) as:

$$A_{undil} = \frac{A_{raw}}{F_D}. \tag{20}$$

In a naive approach, when we consider the $^{15}ND_3$ target, we see that there are 3 polarized deuterons (6 polarized nucleons) for every 21 nucleons. Therefore, the dilution factor, which was defined as the fraction of events scattered from polarized target nucleons, would be 6/21. For a more precise approach, this number would be slightly modified by the difference in cross section for scattering off proton versus scattering off neutron, and nuclear effects. However, the additional material in the beam path, mainly the target windows and the liquid helium bath, makes the determination of the dilution factor more complicated.

TABLE 4: Target parameter definitions. The subscript $\mathcal{X}$ represents different target types used during the experiment. The following acronyms are used for different target types throughout this section: N for nitrogen; A for ammonia; T (or D) for deuteron; C for carbon and He for liquid helium. In addition, Al is aluminum, K is kapton and F represents all kapton and aluminum foils. All counts (represented by $n_{\mathcal{X}}$) are normalized to the corresponding total integrated beam charge for each target. The quantity f is introduced for convenience. It assumes $\sigma_F \approx \sigma_C$ so that the foil mass thickness can be expressed as a fraction of carbon mass thickness. This quantity is used in later sections while calculating the target lengths.

Parameter	Definition
L	Total length of the target cell
$l_{\mathcal{X}}$	Length of target $\mathcal{X}$
$\rho_{\mathcal{X}}$	Density of target $\mathcal{X}$
$\sigma_{\mathcal{X}}$	Cross section of target $\mathcal{X}$
$n_{\mathcal{X}}$	Measured counts from target $\mathcal{X}$
$n'_C = \rho_C l_C \sigma_C$	Expected counts scattered only from ^{12}C
$n'_{He} = \rho_{He} \sigma_{He}$	Expected counts per 1 cm length of liquid ^{4}He
$n'_N = \rho_N l_N \sigma_N$	Expected counts scattered only from ^{15}N
$n'_A = \rho_A l_A \sigma_A$	Expected counts scattered from ammonia
$f = \rho_F l_F / \rho_C l_C$	Contribution to count rate from all Aluminium (Al) and Kapton (K) foils combined, expressed as a fixed fraction of the contribution from ^{12}C

The dilution factor analysis for the proton and the deuteron data were developed together in parallel. As a result, most of the calculations are the same as described in the proton analysis note [1]. Two different calculation methods were utilized, first using the radiated cross-section models and the second using the data parametrization method. Both of these methods are described in detail in the proton analysis note. The general steps in the analysis include combining data from different runs and corrections performed on empty target counts. Afterwards, the calculations of the total target and ammonia target lenghts and calculation of the final dilution factors were performed individually for both methods introduced earlier and compared for systematic error estimates. In the end, the cross section model method was used for all asymmetries in the inelastic region, while it gave a less good description of the quasi-elastic region, where the data-driven method was used. (This in turn is only relevant for the determination of $P_b P_t$ in one case, see next Section).

The only difference in the case of the deuteron dilution factor calculations come from the different number of polarized and unpolarized nucleons in the ND_3 target, which are 6 polarized and 21 unpolarized nucleons instead of 3 and 15 used in the NH_3 case. This modifies the total cross-section of the ammonia target. As a result, the overall dilution factor formula for the ND_3 target is written as:

$$F_D = 1 - \frac{1}{n_A}\left(n_E - l_A n'_{He} + \frac{\rho_A l_A}{\rho_C l_C}\frac{\sigma_N}{\sigma_C} n'_C\right). \tag{21}$$

when we use the data parametrization method and becomes:

$$F_D = \frac{n_T}{n_A} = \frac{\frac{6}{21}\rho_A l_A \sigma_T}{\mathrm{F} + \rho_A l_A(\frac{6}{21}\sigma_T + \frac{15}{21}\sigma_N) + \rho_{He}(L - l_A)\sigma_{He}}. \tag{22}$$

when we use radiated cross-section method. The same change in the ammonia cross-section were also applied while calculating the ammonia target length. Table 5 summarized the densities of various target components for the case of ND_3.

TABLE 5: Densities of the target materials in the EG1b experiment. Values are from Refs. [114] and [115].

Target Material	Density (g/cm^3)	Density (mol/cm^3)
ammonia (NH_3)	0.917	0.0508
ammonia (ND_3)	1.056	0.0502
carbon (^{12}C)	2.17	0.180
nitrogen-15 (^{15}N)	1.1	0.073
liquid helium (He)	0.145	0.0362
kapton (K)	1.42	0.00371
aluminum (Al)	2.69	0.0997

Approximate target lengths from physical measurements are given in Table 6. The value for the window foil material changes after the run 27997 because of the addition of a Kapton (K) piece after this run. The true length of the ammonia target ($^{15}ND_3$), which is represented by l_A, depends on the packing fraction (the percentage of volume occupied by ammonia beads in the total target volume). The liquid Helium exists in all target types since it is used to keep the target at low temperature. Its length depends on how much of the liquid Helium was displaced by the other target material that it is hosting. The length of the Kapton (K) and the Aluminum (Al) targets are known from physical measurements during the experiment. Since the dilution factor

TABLE 6: Lengths of the target materials in the EG1b experiment. Values are from Refs. [114] and [115].

Target Material	Approximate Length (cm)
total (L)	1.9
ammonia (NH_3)	0.6
ammonia (ND_3)	0.6
carbon (^{12}C)	0.23
carbon (^{12}C)	0.22 (for ^{15}N target runs)
nitrogen-15 (^{15}N)	0.5
liquid helium (He)	L minus solid target material
kapton (K)	0.0304(0.0384 after 27997)
kapton (K)	0.0354 (for ^{15}N target runs)
aluminum (Al)	0.0167

is very sensitive to these values, the target lengths for the ammonia targets were studied explicitly to determine the correct F_D. The proton analysis note [1] describes how the target lengths are determined. Table 7 shows the values of some target parameters used for the calculations of the relevant quantities. We reproduce plots of various quantities of interest that enter the dilution factor determination below since they vary slightly from the proton case; however, in all cases the procedure was the same.

TABLE 7: Target parameter values

Quantity	Value	Comment
$\rho_C l_C$	0.498 g/cm^2 = 0.0415 mol/cm^2	mass thickness of carbon
$\rho_C l_C$	0.476 g/cm^2 = 0.0397 mol/cm^2	for ^{15}N target runs
$\rho_K l_K$	0.0432 g/cm^2(0.055 g/cm^2 after 27997)	mass thickness of Kapton
$\rho_K l_K$	0.0503 g/cm^2	for ^{15}N target runs
$\rho_{Al} l_{Al}$	0.0450 g/cm^2	mass thickness of Al
$\rho_F l_F$	0.0882 g/cm^2(0.0996 g/cm^2 after 27997)	mass thickness of Al + K foils
$\rho_F l_F$	0.0952 g/cm^2	for ^{15}N target runs
f	0.177(0.200 after 27997)	$\rho_F l_F / \rho_C l_C$
f	0.235	for ^{15}N target runs

TABLE 8: Calculated total target length L for different data sets in the EG1b experiment are shown for both methods. Method 2 results were used for the final analysis. L_{avg} is used only for $^{12}C/^{15}N$ analysis [113].

Beam Energy (GeV)	Torus Setting	L(cm)-Method 1	L(cm)-Method 2
1.606	+	1.93	1.90
1.606	−	1.82	1.85
1.723	−	1.87	1.87
2.286	+	1.76	1.77
2.561	+	1.93	1.92
2.561	−	1.84	1.86
4.238	+	2.01	2.00
4.238	−	2.04	2.05
5.615	+	1.77	1.78
5.725	−	1.79	1.83
5.743	+	1.93	1.95
5.743	−	1.82	1.87
L_{avg}	$^{12}C/^{15}N$	1.89	1.90

TABLE 9: Values of the effective ammonia target length (l_A), using the two different methods described in the text. The error bars reflect only the error on the statistical fit, not the true uncertainty on the value.

Beam E	Torus	l_A(cm)-Method 1	l_A(cm)-Method 2)
1.606	+	0.6611 ± 0.0005	0.6865 ± 0.0002
1.606	−	0.6394 ± 0.0022	0.6755 ± 0.0005
1.723	−	0.5926 ± 0.0008	0.6262 ± 0.0002
2.561	+	0.5887 ± 0.0009	0.5974 ± 0.0004
2.561	−	0.6179 ± 0.0003	0.6314 ± 0.0002
4.238	+	0.5977 ± 0.0009	0.5978 ± 0.0004
4.238	−	0.6084 ± 0.0003	0.6130 ± 0.0001
5.615	+	0.6045 ± 0.0011	0.6049 ± 0.0005
5.725	+	0.5947 ± 0.0013	0.5897 ± 0.0006
5.725	−	0.5719 ± 0.0005	0.5703 ± 0.0003
5.743	−	0.7226 ± 0.0006	0.7232 ± 0.0003

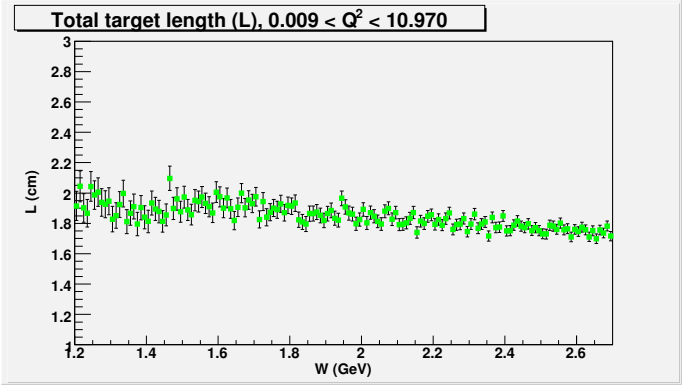

FIG. 1: Total target length, L, calculated using the EG1b data, shown as a function of W averaged over Q^2 bins. A W cut of 1.40 GeV is incorporated for the final value of L to remove the effects of the Δ-resonance. Plot is courtesy of R. Fersch.

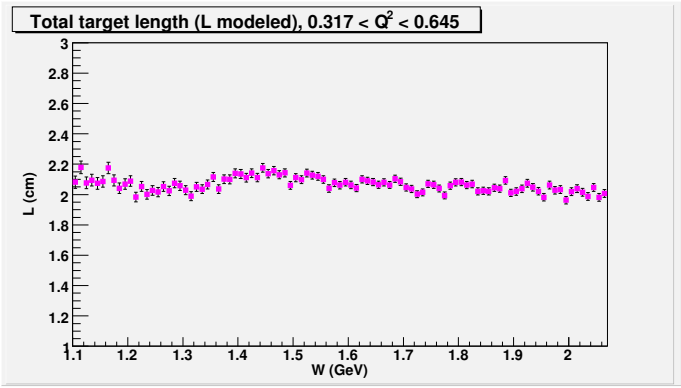

FIG. 2: Total target length, L, calculated using the radiated cross-section models, shown as a function of W, averaged over Q^2 bins ($0.317 < Q^2 < 0.645$) for the 4.2 GeV inbending data set. Plot is courtesy of R. Fersch.

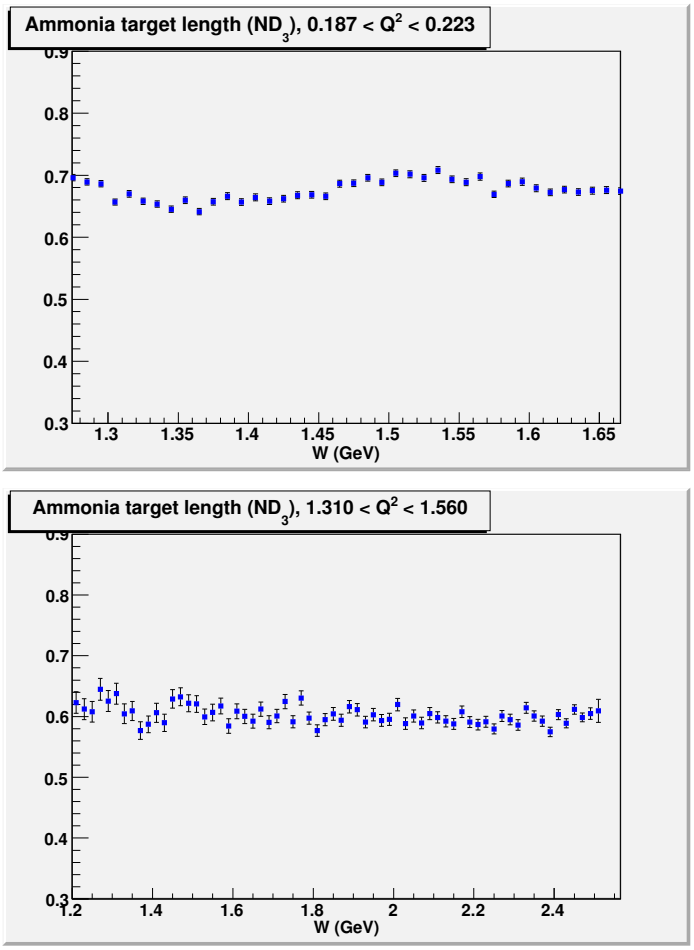

FIG. 3: ND_3 effective target length in cm (calculated from method 1) as a function of W for the 1.6 GeV inbending (top) and 4.2 GeV inbending (bottom) data sets are shown.

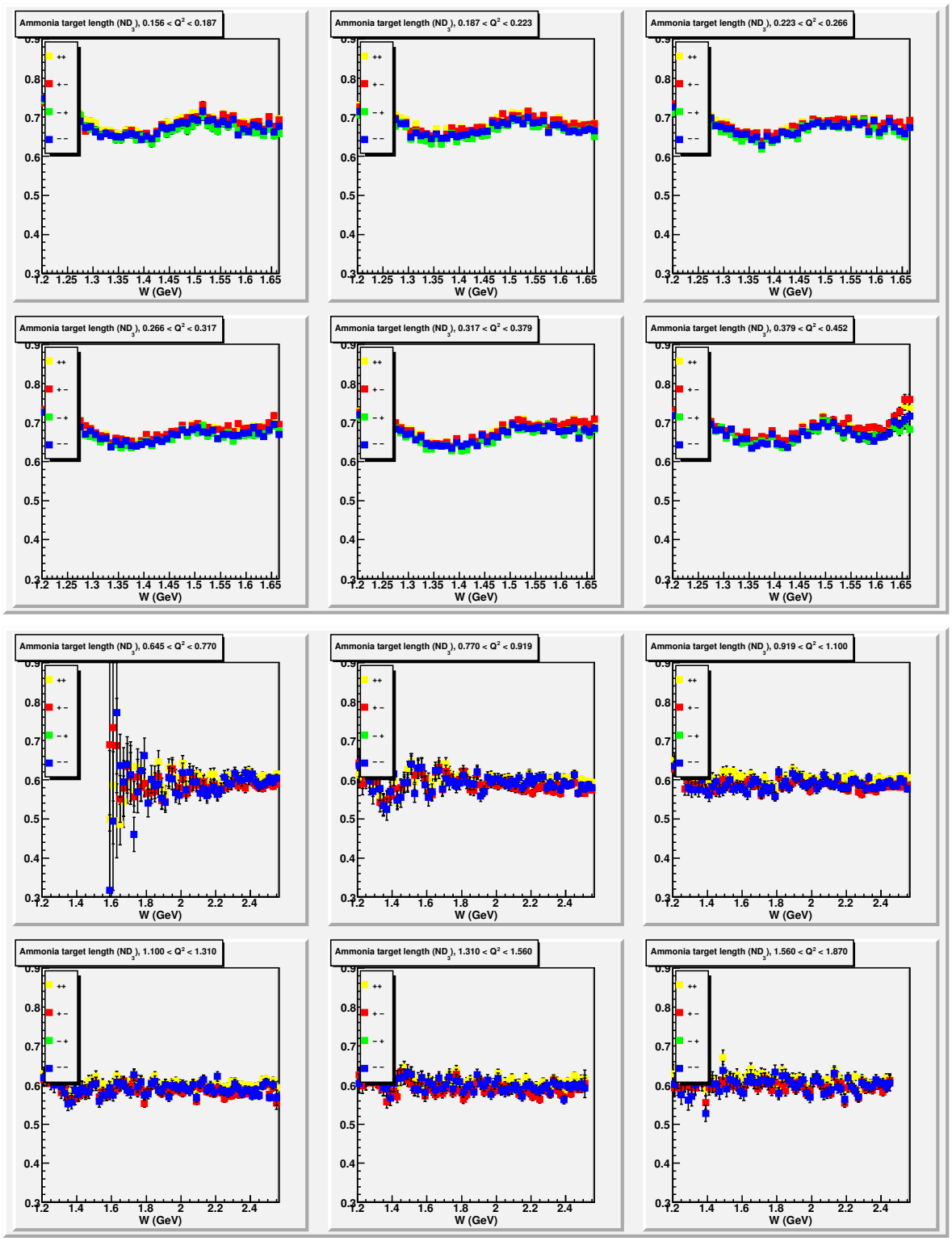

FIG. 4: ND_3 effective target length (in cm) as a function of W for the 1.6 GeV (top) and 4.2 GeV (bottom) inbending data sets. Different colors represent different helicity configurations. The calculations were made by using method 1.

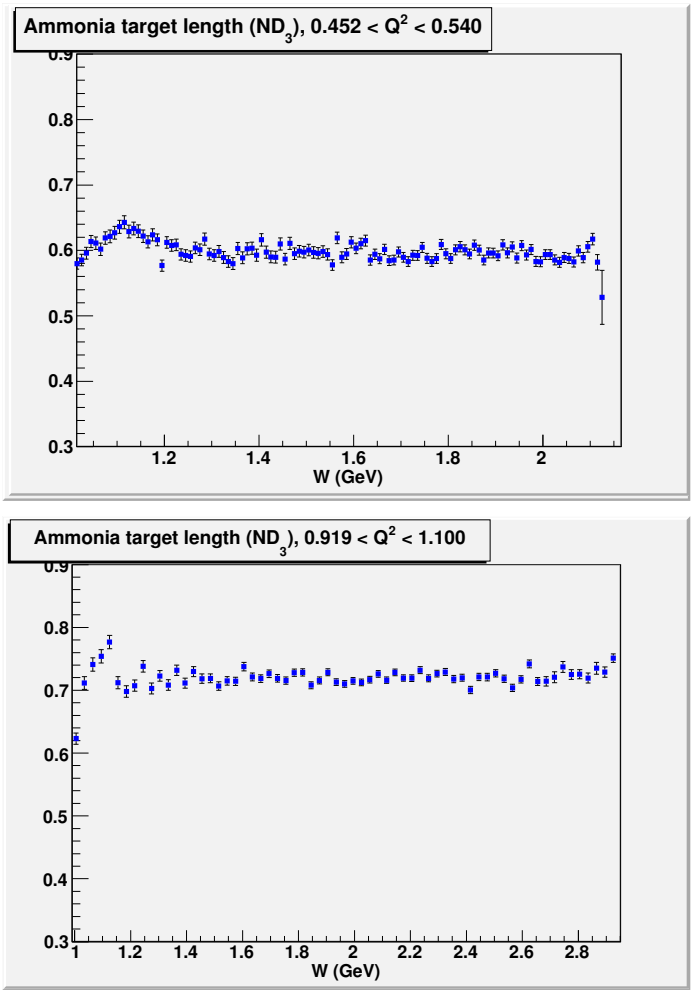

FIG. 5: ND_3 target length shown as a function of W for the 2.5 GeV inbending and the 5.8 GeV outbending data sets. These values are calculated using the radiated cross section model. Plot is courtesy of R. Fersch.

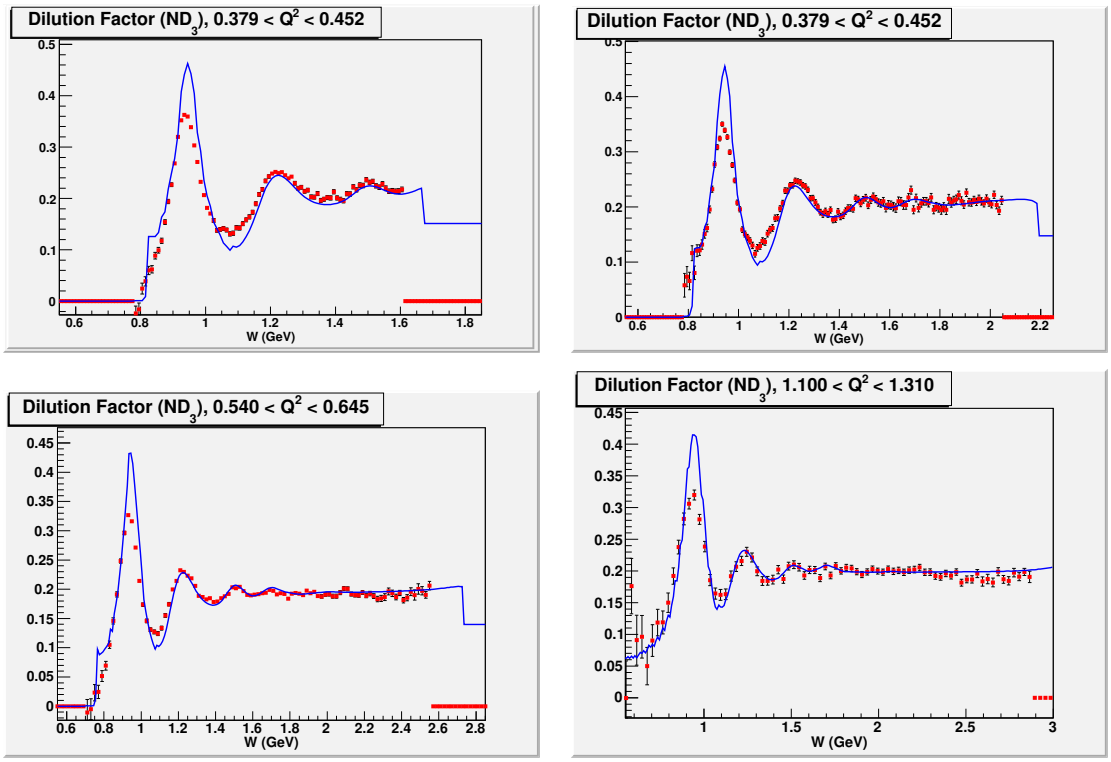

FIG. 6: Dilution factors as a function of W, shown at four different beam energies (1.6+ (top left), 2.5− (top right), 4.2− (bottom left) and 5.7− (bottom right)). The results from method 1 are shown as the red data points while the method 2 results are overlayed as blue lines. In the quasi-elastic region ($W < 1.1$ GeV), the data-driven method 1 was considered more reliable; however, in the end we only used data above $W = 1.1$ GeV where the model-driven method (blue line) is more accurate.

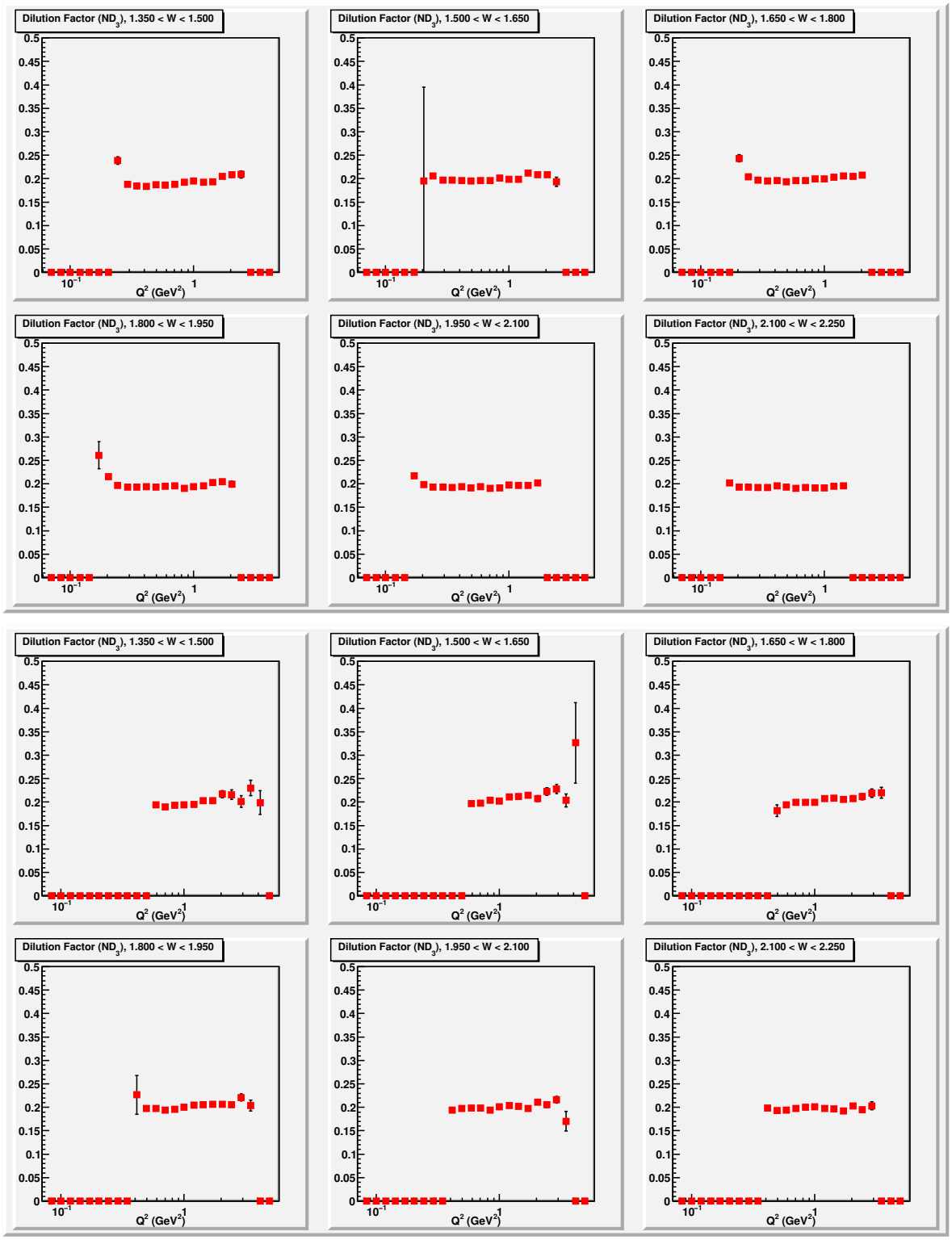

FIG. 7: Dilution factors as a function of Q^2, shown for several W bins, for the 4.2− (top) and 5.7− (bottom) data sets. There is a slight Q^2 dependence of the dilution factor for some W regions.

I.4 BEAM AND TARGET POLARIZATION

In order to determine the double spin asymmetry, the raw asymmetry from the count rates needs to be corrected for the net polarization. Therefore the product of the beam and target polarization is required. During the experiment, the beam polarization was measured by using the Moller Polarimeter and the target polarization was monitored by the Nuclear Magnetic Resonance (NMR) system. In the EG1b experiment, the electron beam polarization was very stable and the measurements from the Moller Polarimeter are dependable. On the other hand, the target polarization was not quite stable. Moreover, the NMR coils are located outside the target, and are therefore more sensitive to the outer layers of the target material. However, the polarization of the target can change within the target volume, especially since the regions of the target exposed to the beam are depolarized more quickly. To prevent quick and local depolarization of the target material, the beam is rastered over the target area in a spiral motion. However, the rastering is not always perfect and especially the outer layer of the target, to which the NMR is most sensitive, is not efficiently rastered. Therefore, it is generally expected that NMR values are superficially higher than the true polarization of the target. Moreover, there are other technical uncertainties on the NMR readings that are not well understood. As a result, we need a reliable method of determining the true beam $\times$ target polarization.

The most reliable method to determine the polarization is to extract the information from the data itself. This extraction is based on the fact that the theoretical asymmetry for elastic and quasi-elastic events is well determined. Once the theoretical asymmetry is known, the beam and target polarization can be determined according to:

$$P_b P_t = \frac{A_{meas}^{quasi-el}}{F_D \; A_{theo}^{quasi-el}} \tag{23}$$

where F_D stands for the dilution factor to remove the effect of scattering from unpolarized nucleons in the target. Therefore, what we need to do is to extract the asymmetry by using quasi-elastic scattering from the deuteron, correct it for the background contributions and then divide it by the theoretical prediction. For the EG1b experiment, this was done separately for each Q^2 bin. Then, the $P_b P_t$ values from all Q^2 bins with reasonable statistical error were averaged to determine the final value, while checking that the "Q^2-dependence" was flat within statistical errors.

I.4.1 Theoretical Asymmetry For Quasi-Elastic Scattering from the Deuteron

The elastic double-spin asymmetry $A_{||}$ for a proton or neutron can be calculated by using the electric and magnetic form factors G_E and G_M of the respective nucleon. The virtual photon asymmetries for elastic scattering are simply [2]:

$$A_1 = 1 \tag{24}$$

and

$$A_2 = \sqrt{R_{(el)}} = \frac{\sqrt{Q^2}}{\nu}\frac{G_E(Q^2)}{G_M(Q^2)}. \tag{25}$$

$R_{(el)}$ represents the structure function R (the ratio of longitudinal to transverse cross section) in the elastic region. Using $Q^2 = 2M\nu$ for elastic events, the double spin asymmetry for elastic scattering can be calculated as:

$$A_{||} = \frac{2\tau G[\frac{M}{E} + G\,(\tau\,\frac{M}{E} + (1+\tau)\tan^2(\theta/2))]}{1 + G^2\,\tau/\epsilon}, \tag{26}$$

where $\tau = Q^2/4M^2$, $G = G_M/G_E$, E is the beam energy, M is the mass of the nucleon and θ is the polar scattering angle of the electron. For the electromagnetic form factors we used the latest parametrization by J. Arrington [117].

For the deuteron, one has to express the asymmetry in the quasi-elastic region ($\nu \approx Q^2/2M_p$) in terms of the contributions from its constituent nucleons. There are in principle two ways to do this: In the first method, quasi-elastic events are selected by detecting only the scattered electrons. This is called the inclusive method. In this case, the weighted contributions from both proton and neutron contribute to the observed quasielastic asymmetry $A_{||}$. Alternatively, one detects the knocked-out proton in coincidence with the scattered electron, using kinematic cuts to ascertain that it carries (nearly) all of the 4-momentum transfer $\nu, \vec{q}$. This is the "exclusive" method. In this case, only the proton inside deuterium contributes (to a very good approximation), and one can use directly the asymmetry Eq. 26 for the proton only, with small corrections for its Fermi motion and D-state contributions to extrapolate to the deuteron polarization. In the next Section, we discuss the event selection for both these methods in detail.

I.4.2 Extraction of Quasi-Elastic Asymmetry from the Data

For both methods discussed above, the first step is to select electrons that fall within the quasi-elastic region. For each detected electron, the final state mass W is reconstructed and a specific cut on W depending on the data configuration (beam energy and torus settings) is applied to select the quasi-elastic events. Table 10 lists the applied cuts for each configuration.

TABLE 10: W limits in GeV for (quasi-)elastic event selection in the inclusive (incl) and exclusive (excl) methods.

E_{beam}	incl W_{min}	incl W_{max}	excl W_{min}	excl W_{max}
1.606	0.90	0.98	0.88	0.98
1.723	0.90	0.98	0.88	0.98
2.286	0.90	0.99	0.87	0.99
2.561	0.90	0.99	0.87	0.99
4.238	0.90	0.99	0.86	1.02
5.615	0.88	1.00	0.84	1.02
5.725	0.88	1.00	0.84	1.02
5.743	0.88	1.00	0.84	1.02

Inclusive Method

The double spin asymmetries of the proton and the neutron were calculated according to Eq. (26) using the parameterization given by Arrington. After that, the deuteron quasi-elastic asymmetry was determined from that of the proton and the neutron as the weighted average:

$$A_{||}^{D} = \frac{\sigma_p^{el} A_p^{el} + \sigma_n^{el} A_n^{el}}{\sigma_p^{el} + \sigma_n^{el}} \left(1 - \frac{3}{2} w_D\right) \tag{27}$$

where w_D is the probability of finding deuteron in D-state. We also used a more detailed calculation incorporating the deuteron wave function, including the momentum-dependent nucleon polarization in deuterium. The two methods yielded very similar results.

The first step in applying this method to the data is to identify the electrons. The set of cuts we used for this purpose is shown in Table 11. The advantage of the inclusive method is its statistical power. The amount of the quasi-elastic events

determined from inclusive scattering is very high compared to the exclusive method. However, the higher statistics comes with a price: more background contribution. The main challenge of this method is to isolate the quasi-elastic peak and to correctly remove the background. We used the data-driven method to calculate the dilution factor to remove the background from inclusive quasi-elastic events.

TABLE 11: Electron cuts for $P_b P_t$ calculation with the inclusive method.

particle charge = -1
good helicity selection
one electron per event
$p \geq 0.01 E_B$
$p \leq E_B$
$0 \leq flag \leq 5$ or $10 \leq flag \leq 15$
triggerbit cut
$CC_{nphe} > 2.0$ if $p \leq 3.0$ GeV or $CC_{nphe} > 0.5$ if $p > 3.0$ GeV
$EC_{tot}/p > 0.20$ if $p \leq 3.0$ GeV or $EC_{tot}/p > 0.24$ if $p > 3.0$ GeV
$EC_{in} > 0.06$
-58.0 $\leq z_{vertex} \leq$ -52.0
$7.5^\circ < \theta < 49^\circ$
$\nu > 0$ GeV
sector 5 cut
loose fiducial cuts
geometric-timing cuts on the CC
W cut (see Table 10)

Another crucial point was to define the quasi-elastic region. We varied the W cuts and monitored the resulting $P_b P_t$ values and their statistical errors. We began with a tight cut, which results in a large statistical error and then we loosened the cut step by step until the $P_b P_t$ value stabilized. Then we also moved the cut region by an offset and monitored the $P_b P_t$ values in order to choose the region where the values are most stable. We performed this procedure for each data configuration. Table 10 lists the final W cuts for different beam energies.

Exclusive Method

In the exclusive method, we selected quasi-elastic $ed \rightarrow epn$ events by identifying the electron and recoil proton in coincidence. The electron cuts applied for this case are slightly different than the previous case. In particular, the cuts on the EC and

CC can be loosened because the requirement for a proton within collinearity and missing energy cuts restricts our particle selection. The final electron cuts are listed in Table 12. For the proton, we used a timing cut of -0.8 ns $< \Delta t <$ 0.8 ns to gain more events. In addition, the cuts applied for the selection of quasi-elastic events are listed in Table 13.

The advantage of the exclusive method is that the background contribution is small since we apply strict kinematic constraints on the data. However, because the proton is not always detected, this approach generally reduces the statistics, which results in a higher statistical error on the extracted $P_b P_t$ value in comparison to the inclusive method. In order to remove the background contribution from the ND_3 data, we used subtract an appropriately scaled spectrum from carbon runs. Fig. 8 shows the distributions of the azimuthal angle differences between the protons and the electrons ($\Delta\phi = \phi_p - \phi_e$) in quasi-elastic events for a few data sets with the ND_3 target. Also, Fig. 9 shows the W distributions for the same events. The scaling factor for the carbon data was determined by using the ϕ distribution of the quasi-elastic events. The ϕ ranges used for this purpose were $160^\circ \leq \Delta\phi \leq 170^\circ$ and $190^\circ \leq \Delta\phi \leq 200^\circ$.

TABLE 12: Electron cuts for $P_b P_t$ calculation with the exclusive method.

particle charge = -1
good helicity selection
one electron per event
$p \leq E_B$
$0 \leq flag \leq 5$ or $10 \leq flag \leq 15$
triggerbit cut
$CC_{nphe} > 1.0$
$EC_{tot}/p > 0.15$ if $p \leq 3.0$ GeV or $EC_{tot}/p > 0.20$ if $p > 3.0$ GeV
-58.0 $\leq z_{vertex} \leq$ -52.0
$8.5^\circ < \theta < 49^\circ$
sector 5 cut
$\nu > 0$ GeV

I.4.3 Final $P_b P_t$ Values

For each target and beam polarization in the EG1b experiment, the $P_b P_t$ values from inclusive and exclusive methods were determined as described above for each

TABLE 13: Cuts for the selection of quasi-elastic events for P_bP_t calculation. An electron and a proton were required with at most one neutral particle in the event in order not to loose events with accidental signals in any of the detectors (by a cosmic ray or a stray photon).

good helicity selection
particles in the event = 2 (or 3 with one neutral particle)
electron found in the event
proton found in the event
$\lvert E_{[miss]}\rvert \leq 0.08$ GeV
$\lvert\theta_p - \theta_Q\rvert < 2^\circ$
$\theta_Q < 49^\circ$
-3° < $\lvert\phi_p - \phi_e\rvert$ - 180° < 3°
W cut (see Table 10)

Q^2 bin. Some sample plots can be seen in Figs. 10-14. In the end, the P_bP_t values are averaged over Q^2 bins as:

$$P_bP_t = \sum_{Q^2} \frac{P_bP_t(Q^2)}{\sigma^2_{P_bP_t}(Q^2)} / \sum_{Q^2} \frac{1}{\sigma^2_{P_bP_t}(Q^2)} \tag{28}$$

$$\sigma_{P_bP_t} = 1/\sum_{Q^2} \frac{1}{\sigma^2_{P_bP_t}(Q^2)} \tag{29}$$

leaving out the Q^2 bins with high statistical errors (the ones with statistical error larger than 0.5). The Q^2 bin ranges for different data configurations can be seen in Table 14. The final values are listed in Table 15 for different data sets and target polarizations. Then the values were compared from four different independent studies of P_bP_t [118]. The values agree well within statistical fluctuations. After careful considerations, it was agreed that the exclusive method in general gave more reliable results. Therefore, for the final analysis, exclusive values were used except for the 1.6 and 1.7 GeV outbending data sets, for which we used the inclusive P_bP_t values because the exclusive values had large statistical errors. The error on the inclusive method is rather small because of the statistical power of the method. Therefore, we did not use the statistical error for those data but instead assigned a 10% error on the value, which is a reasonable estimate made by comparing the independent studies on P_bP_t.

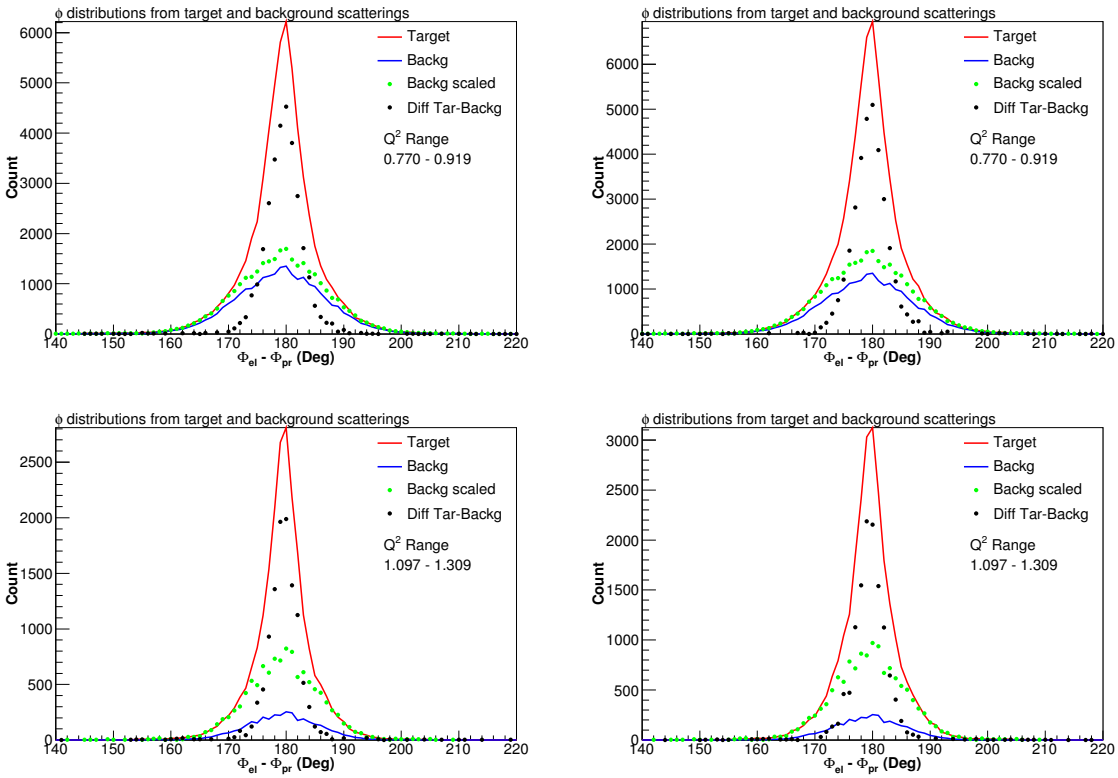

FIG. 8: Distribution of azimuthal angle difference between the electron and the proton ($\Delta\phi = \phi_p - \phi_e$) in exclusive quasi-elastic events for different data sets with the ND_3 target. The top row is from the 1.6 GeV positive (left) and negative (right) target polarizations. The bottom row is the same for the 2.5 GeV data set. The red solid line (*Target*) is the raw inclusive data from the ND_3 target. The blue solid line (*Backg*) represents the ^{12}C data, which is scaled to the ND_3 data (green dots) and subtracted from it. The final quasi-elastic distribution is shown with black dots (*Diff*). The range -3° < $|\phi_p - \phi_e|$ - 180° < 3° was selected for the calculation of $P_b P_t$.

I.4.4 $P_b P_t$ for Weighting Data from Different Helicity Configurations

We have various data sets with different beam energies, torus currents and target polarizations. In order to combine the asymmetries from these data sets, we would like to give them different weights according to their overall statistical precision. In particular, while combining the data sets with opposite target polarizations, we know that the two sets can have a rather significant difference in the magnitude of their target polarizations. An optimal strategy requires us to include this information in our statistical weighting. However, our method of determining the product of beam and target polarization $P_b P_t$ (using elastic or quasi-elastic scattering) will not yield

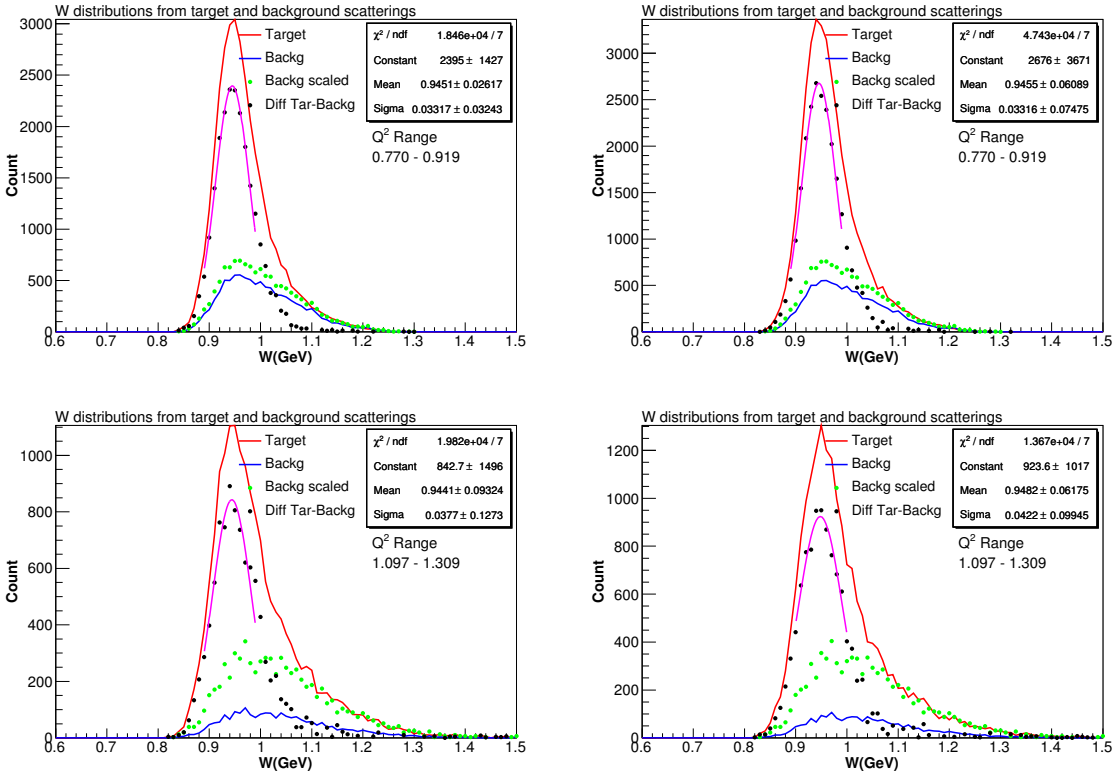

FIG. 9: W distributions for exclusive ep quasi-elastic events for different data sets, showing the background removal for the ND_3 target. The top row is from the 1.6 GeV positive (left) and negative (right) target polarizations. The W cut applied on this data set to calculate $P_b P_t$ was $0.88 \leq W \leq 0.98$. The bottom row is the same for the 2.5 GeV data. The W cut was $0.87 \leq W \leq 0.99$. The explanations for the curves and data points are provided in the caption of Fig. 8.

TABLE 14: Q^2 limits in GeV for the $P_b P_t$ average.

E_{beam}	Torus	incl Q^2_{min}	incl Q^2_{max}	excl Q^2_{min}	excl Q^2_{max}
1.606	+	0.20	1.00	0.71	1.00
1.606	−	0.24	0.71	0.71	0.84
1.723	−	0.17	0.84	0.71	1.00
2.561	+	0.29	2.00	1.00	2.00
2.561	−	0.29	1.86	1.00	1.70
4.238	+	0.59	3.50	1.40	2.90
4.238	−	0.59	3.50	1.40	3.50
5.615	+	1.20	5.90	1.70	6.00
5.725	+	0.84	5.90	1.70	5.90
5.725	−	0.84	5.90	1.70	5.90
5.743	−	0.84	5.90	1.70	5.90

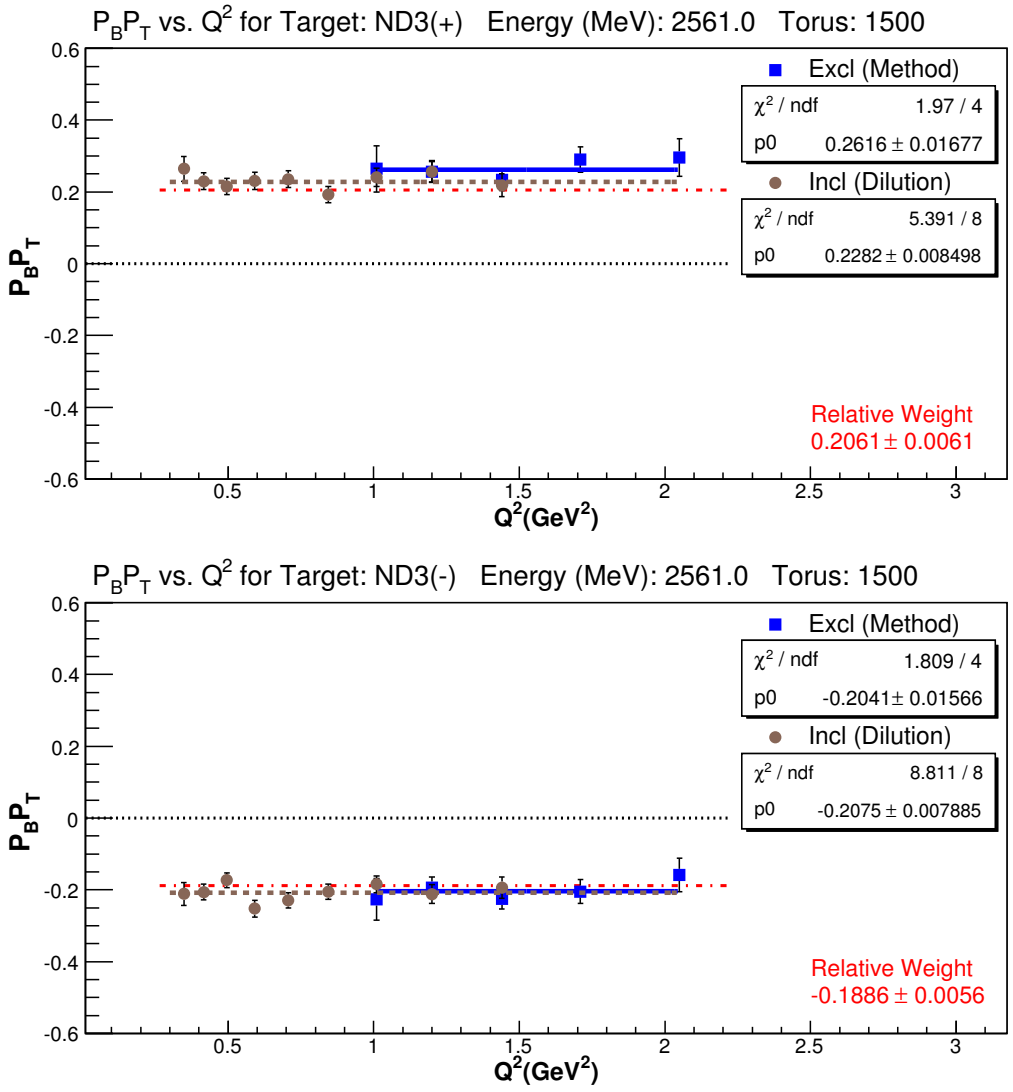

FIG. 10: P_bP_t values for the 2.5 GeV inbending data sets for ND_3 target. The plot shows the resulting P_bP_t values for the Q^2 bins with available data. The results from the exclusive (blue square) and the inclusive (brown circle) methods are shown. The corresponding linear fits to the data are also shown as lines: the solid blue line is for the exclusive and the dashed brown line is for the inclusive methods. The results of the linear fits are shown. Note that these results from the linear fits are not the actual P_bP_t values but they are practically the same up to 3rd significant figure. In addition, the relative weighting factor described in section I.4.4 is also written on each plot.

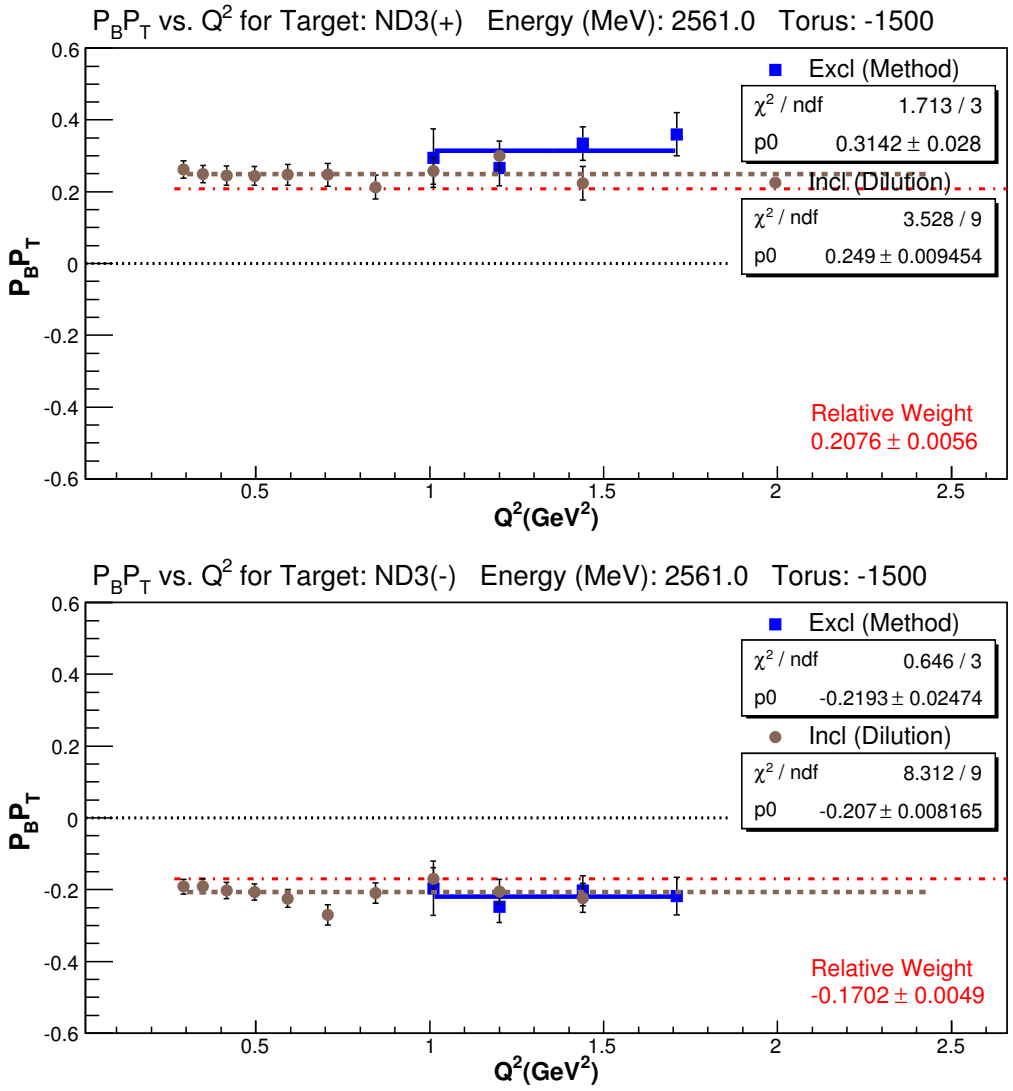

FIG. 11: $P_b P_t$ values for different data sets for ND_3 target.

sufficient statistical accuracy over a single "group" to make this feasible. Therefore, we need a more precise method at least to estimate the *relative* magnitude of $P_b P_t$ for a given data set.

Our approach is to extract an estimate of $P_b P_t$ using our model of the existing spin structure function data together with the already determined asymmetries for each bin for a given group. This does not have to be too precise (and of course may be off by an overall scale factor, since we don't know whether our existing model has the correct overall scale). However, it is sufficient to give us a *relative* magnitude of

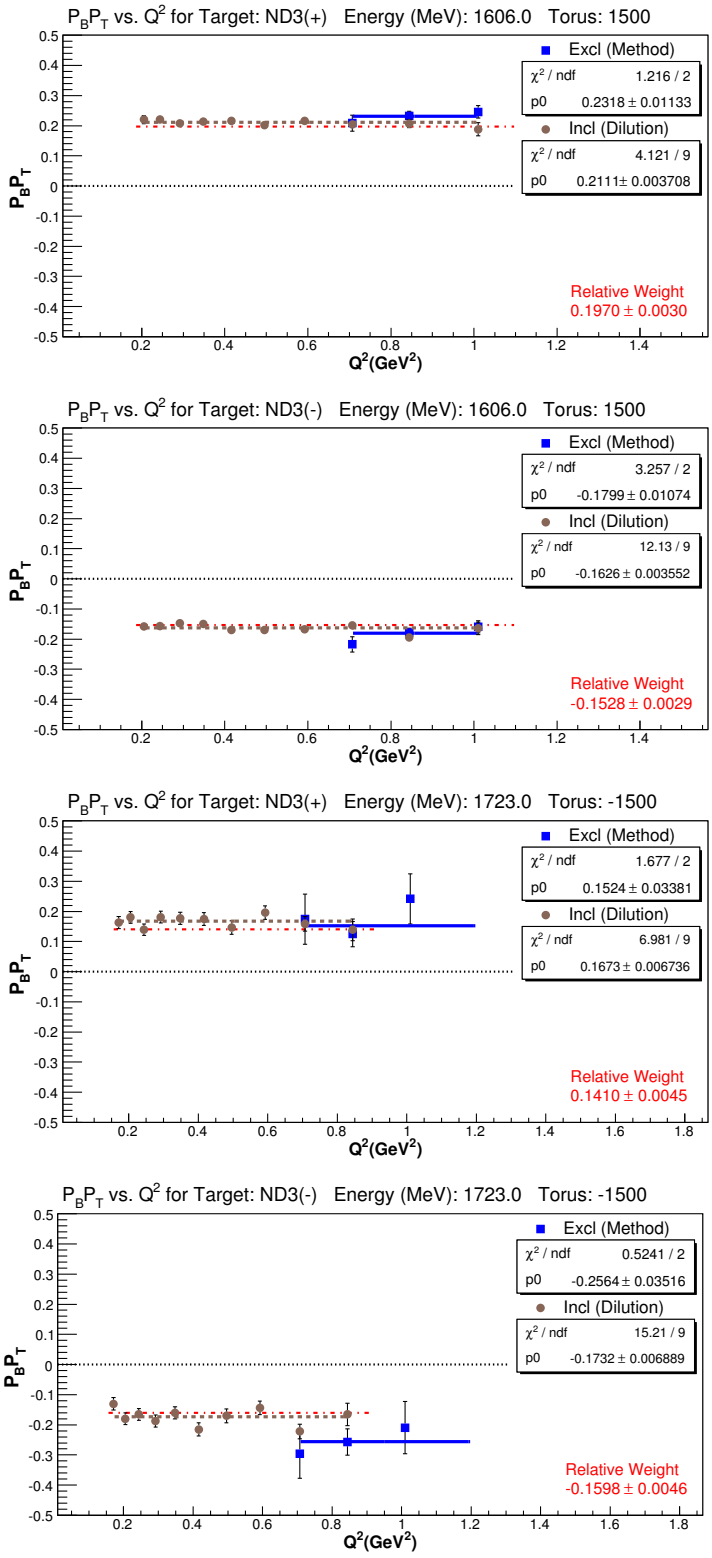

FIG. 12: P_bP_t values for different data sets for ND_3 target.

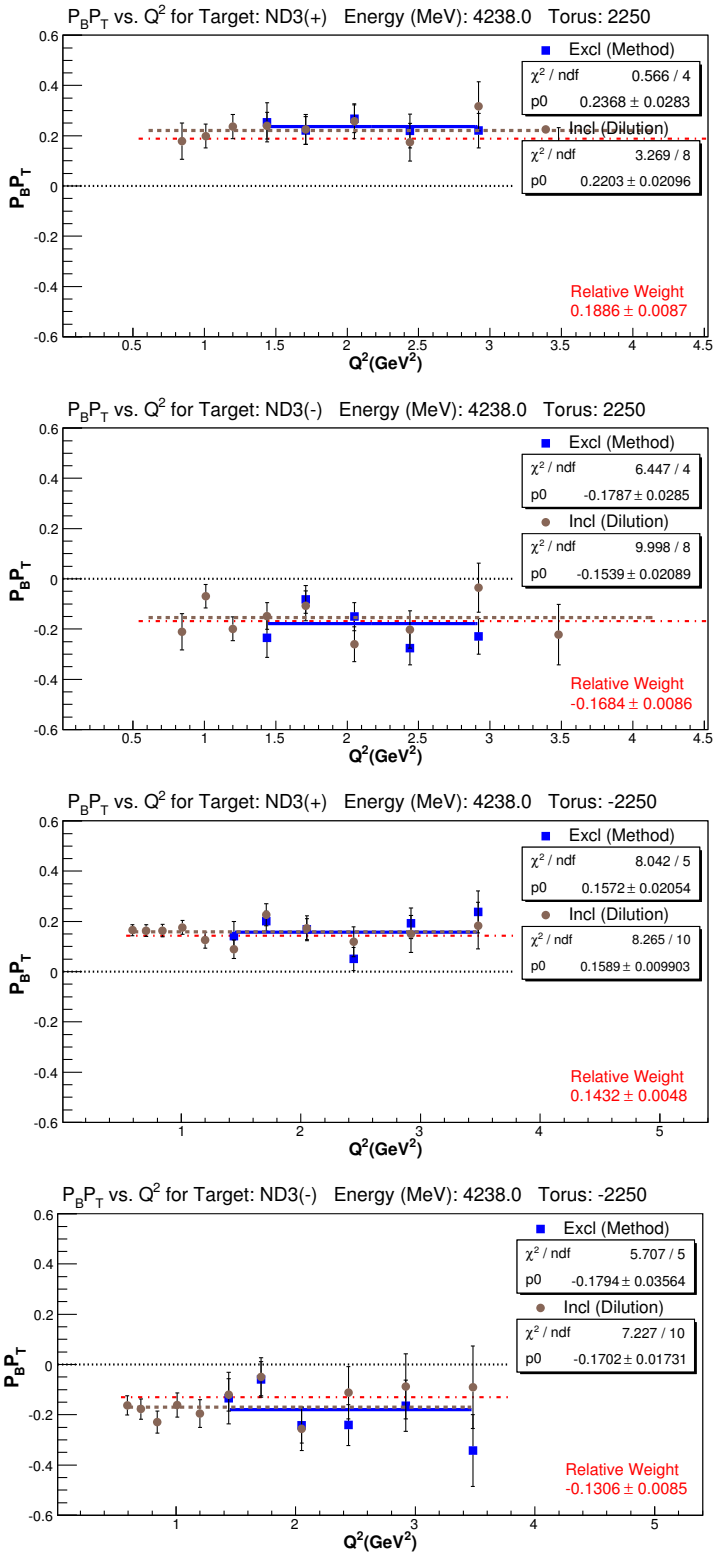

FIG. 13: P_bP_t values for different data sets for ND_3 target.

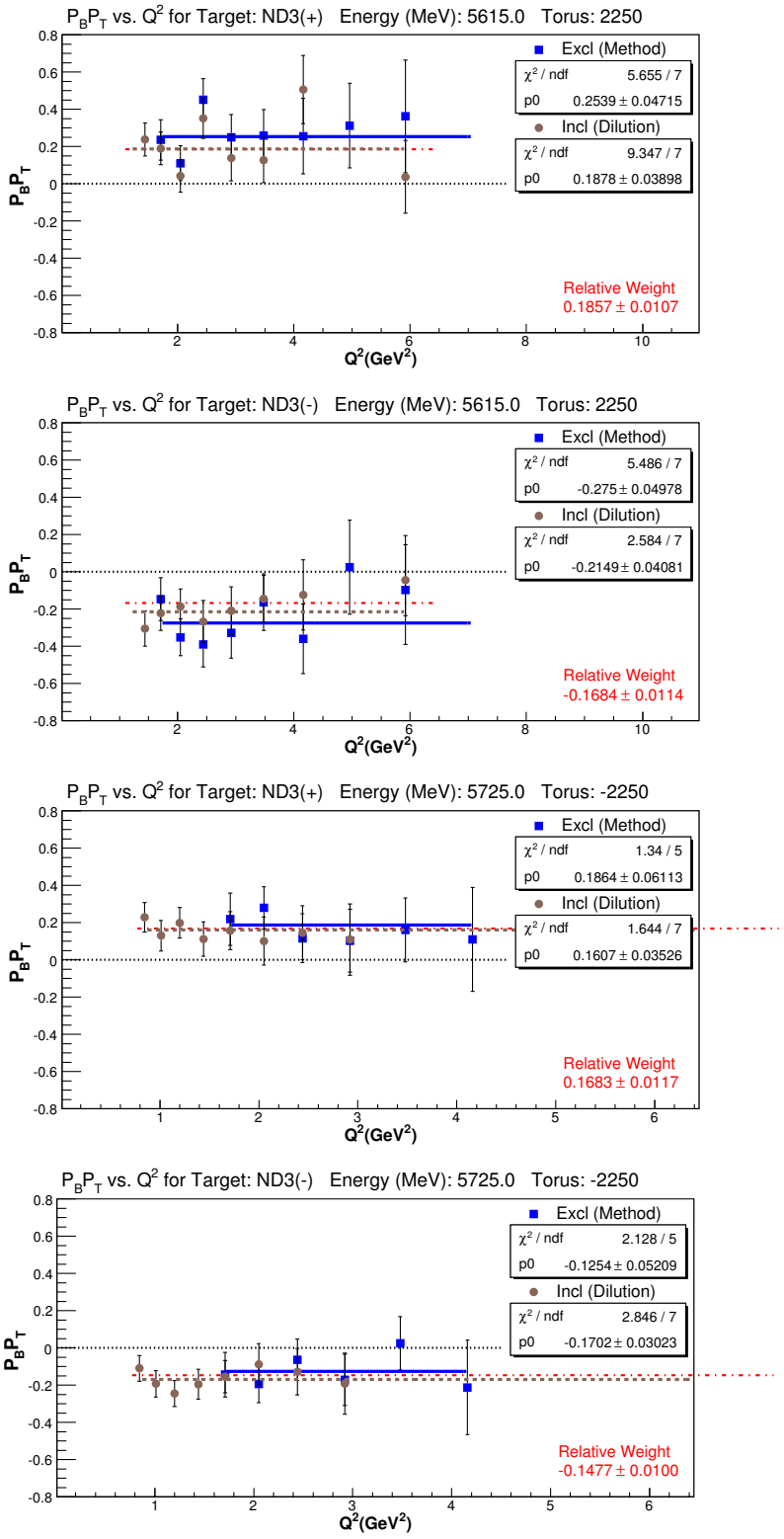

FIG. 14: $P_b P_t$ values for different data sets for ND_3 target.

TABLE 15: P_bP_t values from different methods for all data sets with ND_3 target. E_B is the beam energy, I_T refers to torus polarity (inbending or outbending) and T.Pol is the target polarization sign. The results from the exclusive (*excl*) and the inclusive (*incl*) are listed together with the corresponding errors. The values given in the *rela* column are only used as statistical weighting factors for each set as described in section I.4.4. For the 1.6 and 1.7 GeV outbending data, the inclusive method results were used with 10% error assigned. For the other data sets, the exclusive method results were used for the final analysis.

E_B I_T	T.Pol	excl	excl Err	incl	incl Err	rela	rela Err
1606 i	+	0.23644	0.01326	0.21481	0.00425	0.20581	0.00324
1606 i	−	-0.18544	0.01227	-0.16114	0.00398	-0.15800	0.00310
1606 o	+	0.16199	0.04238	0.17735	0.00863	0.17037	0.00531
1723 o	+	0.16196	0.03588	0.16866	0.00696	0.14782	0.00459
1723 o	−	-0.26576	0.03709	-0.17450	0.00712	-0.16429	0.00470
2561 i	+	0.26900	0.01799	0.22716	0.00914	0.19565	0.00566
2561 i	−	-0.21256	0.01679	-0.20686	0.00849	-0.17591	0.00526
2561 o	+	0.30754	0.02815	0.25168	0.00960	0.22654	0.00566
2561 o	−	-0.21734	0.02532	-0.20961	0.00848	-0.18773	0.00501
4238 i	+	0.24728	0.02994	0.22229	0.02139	0.18059	0.00807
4238 i	−	-0.18915	0.03048	-0.15489	0.02131	-0.15860	0.00806
4238 o	+	0.15641	0.02065	0.16111	0.00989	0.15101	0.00462
4238 o	−	-0.18185	0.03634	-0.17183	0.01771	-0.13286	0.00831
5615 i	+	0.25651	0.04793	0.18969	0.03941	0.17430	0.01002
5615 i	−	-0.28254	0.05152	-0.21685	0.04129	-0.15815	0.01061
5725 i	+	0.21415	0.04658	0.14212	0.04508	0.13318	0.00910
5725 i	−	-0.16873	0.06170	-0.09980	0.06277	-0.15301	0.01269
5725 o	+	0.18149	0.05974	0.15434	0.03507	0.16153	0.01068
5725 o	−	-0.12594	0.05242	-0.15947	0.03008	-0.14486	0.00915
5743 o	+	0.18579	0.04022	0.15101	0.02616	0.12969	0.00742
5743 o	−	-0.20827	0.06619	-0.10362	0.03928	-0.09480	0.01113

P_bP_t, that we will call P_{rel}.

This requires to use the "models" to determine a "predicted" $A_{||}$ for each bin where the group under investigation has data. Above $W = 1.08$ GeV this was done with a simple code that uses the A_1, A_2 and R from "models" and combines them into $A_{||}^{model} = D(A_1+\eta A_2)$, using the correct beam energy and electron scattering angle for each bin to calculate the required kinematic quantities like ϵ, η and D. For kinematic bins below $W = 1.08$ GeV, we used the (quasi-)elastic inclusive asymmetries instead.

These were calculated according to Eqs. (26) and (27). It should be noted that, bins below $W = 0.9$ GeV are not used in this process since the data in these bins are largely unpolarized and/or have large random errors.

At this point, we can calculate an estimate for P_{rel} for each bin in $W > 0.9$ GeV and Q^2 for a given data set (G) as follows:

$$P_{rel}(W, Q^2) = \frac{A^G_{raw}(W, Q^2)}{F_D A^{model}_{||}}, \tag{30}$$

where A^G_{raw} represents the raw asymmetry of the data set (all runs combined) and F_D is the dilution factor for the bin in question. The error on this quantity, for just one kinematic bin, is

$$\sigma_{P_{rel}} = \frac{\sigma_{A^G_{raw}}}{F_D A^{model}_{||}}. \tag{31}$$

We can then combine the information from *all* [Q^2,W] bins with $W > 0.90$ GeV by the usual statistically weighted mean:

$$P^G_{rel} = \frac{\sum\limits_{bins} P_{rel}/\sigma^2_{P_{rel}}}{\sum\limits_{bins} 1/\sigma^2_{P_{rel}}}, \tag{32}$$

with statistical error

$$\sigma^2_{P^G_{rel}} = \frac{1}{\sum\limits_{bins} 1/\sigma^2_{P_{rel}}}. \tag{33}$$

From Eqs. (30) and (31), we can deduce that

$$\frac{P_{rel}}{\sigma^2_{P_{rel}}} = F_D A^{model}_{||} \frac{A^G_{raw}}{\sigma^2_{A^G_{raw}}}, \tag{34}$$

so, the last equation can also be written as

$$P^G_{rel} = \frac{\sum\limits_{bins} F_D A^{model}_{||} A^G_{raw}/\sigma^2_{A^G_{raw}}}{\sum\limits_{bins} (F_D)^2 (A^{model}_{||})^2/\sigma^2_{A^G_{raw}}}, \tag{35}$$

which avoids any need to divide by (potentially) small (zero) numbers.

While combining the two different data sets with opposite target polarizations, we multiply the total count for each set with the square of its relative $P_b P_t$, given by P^G_{rel}, to determine its weight. Then this weight is divided by the sum from both

data sets to determine the scaling factor associated with each set. Then, this scaling factor is used whenever we need to sum quantities from the two data sets. The raw asymmetries and the true $P_b P_t$ values are summed in this way while combining the data sets with opposite target polarizations. More detailed explanations on the data combining procedure is given in section I.8.

TABLE 16: $P_b P_t$ values for the ND_3 target averaged over opposite target polarizations, from three different methods. E_B is the beam energy, I_T refers to torus polarity (inbending or outbending).

E_B I_T	excl 1	Err	excl 2	Err	incl	Err
1606 i	0.2164	0.0093	0.2246	0.0083	0.1938	0.0030
1606 o	0.1619	0.0423	0.2211	0.0353	0.1773	0.0086
1723 o	0.2180	0.0259	0.2244	0.0197	0.1718	0.0050
2561 i	0.2417	0.0123	0.2426	0.0108	0.2173	0.0062
2561 o	0.2655	0.0191	0.2597	0.0157	0.2321	0.0064
4238 i	0.2219	0.0214	0.1871	0.0182	0.1929	0.0152
4238 o	0.1613	0.0180	0.1591	0.0166	0.1632	0.0086
5615 i	0.2675	0.0352	0.2380	0.0312	0.2012	0.0286
5725 i	0.1957	0.0373	0.1821	0.0306	0.1249	0.0369
5725 o	0.1524	0.0395	0.1803	0.0374	0.1570	0.0229
5743 o	0.1901	0.0349	0.1769	0.0341	0.1419	0.0224

I.5 POLARIZED BACKGROUND CORRECTIONS

The dilution factor corrects for scattering off unpolarized "non-target" nucleons or nuclei in the target material. However, some of these might be polarized and, therefore, affect the observed asymmetry. This section explains the corrections required to account for the effects of the polarized background on the measured asymmetry.

The proton and deuteron targets are embedded in $^{15}NH_3/^{15}ND_3$ molecules. As the targets are polarized by the DNP process, surrounding nucleons from ^{15}N can also become polarized. In addition, there is an approximately 2% contamination of ^{14}N, which is also polarizable. Moreover, a small percentage of isotopically contaminated ammonia molecules such as NH_3 and ND_2H_1 also introduce polarizable single protons. Finally, there is a possibility that the target contains some *un*polarized pure hydrogen atoms, for instance in the form of frozen-in water (H_2O). The presence of contaminating free protons (both polarized and unpolarized) has been studied in

detail in CLAS Note 2012 - 004 [119].

Although the effect of the polarized background on the measured asymmetry is small, it should be corrected for and the correction included in the systematic uncertainty budget. In order to correct for the polarized background, we follow the prescription developed by [120, 70], with some minor changes. The general form of the correction can be written as:

$$A_{\parallel}^{corr} = C_1 \left(A_{\parallel} - C_2 A_p \right), \tag{36}$$

where $A_{\parallel}^{corr}$ is the final, sought-after asymmetry due to only the polarized species of interest. $A_{\parallel}$ represents the measured asymmetry after the dilution factor and the beam $\times$ target polarization corrections have been divided out. (At this point, radiative corrections have not yet been applied to $A_{\parallel}$). The multiplicative factor C_1 corrects for both reductions (due to isotopic impurities) and enhancements of the measured asymmetry (due to additional polarized nucleons of the same species, e.g., quasi-deuterons inside ^{14}N in the case of deuterium targets), proportional to the asymmetry of the intended target . The additive constant $C_2 A_p$ corrects for the asymmetry introduced by free and bound nucleons of a different species (e.g., protons bound in ^{15}N and free protons in an $^{15}ND_3$ target).

Corrections on the deuteron target

For a deuterated ammonia target, the first correction factor in Eq. (36) usually is written as follows:

$$C_1^d = \frac{1}{1 - \eta_p + D_n/(1 - 1.5 w_D)} \approx 1.03 \pm 0.01. \tag{37}$$

The main correction comes from the fraction of events that come from free protons in the target instead of deuterons (due to isotopic impurities and frozen water contamination):

$$\eta_p = \frac{number\ of\ protons}{number\ of\ protons + number\ of\ deuterons} \approx 0.015...0.035 \tag{38}$$

Here, the lower estimate is the standard assumption made for similar targets in past experiments [120] (assuming, e.g., that approximately 4.5% of the ND_3 molecules are actually ND_2H_1) while the maximum value comes from the best estimate in CLAS Note 2012 - 004 [119] based on the actual EG1b data. (The value quoted

in Ref. [119] is 5% contamination; however, the kinematic cuts applied there lead to an enhancement of the proton cross section over the deuteron one by a factor of about 1.4 which has to be removed to get the pure relative number density η_p). It is important to note that this form of Eq. 37 is valid for the case where the dilution factor is calculated based on cross section models and the assumption that the target is pure ND_3. In this case the denominator of the asymmetry, $F_D(n^+ + n^-)$, simply overestimates the counts coming from the sought-after target, deuterium, by a constant factor. On the other hand, if the asymmetry is calculated directly by subtraction of an "empirical background" (i.e., some combination of measured rates from Carbon and empty targets that mimic the non-hydrogen parts of the ammonia target) from the total ammonia counts $n^+ + n^-$, one needs to correct only for the actual number of excess counts from free protons. This means that η_p in Eq. 37 must be multiplied by the ratio $\frac{\sigma_p}{\sigma_d}$ of free proton cross section over total deuteron cross section for the corresponding kinematics, yielding the alternative form of C_1^d:

$$C_1^d = \frac{1 + \eta_p \frac{\sigma_p}{\sigma_d}}{1 + D_n/(1 - 1.5 w_D)}. \tag{39}$$

The term $D_n/(1 - 1.5 w_D)$ in either form of C_1^d corrects for the contribution from "bound deuterons" inside ^{14}N (itself only a small contamination in the ^{15}N used for the EG1 targets). The term w_D corrects for the D-state contribution to the deuteron. The remaining terms are defined as:

$$D_n = \eta_N \frac{P_{^{14}N}}{P_d} \frac{g_{EMC}}{3} \frac{P_{d\,in\,^{14}N}}{P_{^{14}N}} \approx -0.0006... - 0.0010 \tag{40}$$

$$\eta_N = \frac{number\ of\ ^{14}\mathrm{N}}{number\ of\ ^{14}\mathrm{N} + number\ of\ ^{15}\mathrm{N}} \approx 0.02. \tag{41}$$

The factor g_{EMC} is the correction for the EMC effect in nitrogen,

$$g_{EMC}^{^{15}N} \approx g_{EMC}^{^{14}N} \equiv g_{EMC} \approx 1, \tag{42}$$

which is just a crude approximation but its uncertainty is included in the overall uncertainty of D_n. The factor $\frac{P_{^{14}N}}{P_d}$ is estimated via the equal spin temperature hypothesis to be between 0.4 and 0.5 (due to the relative magnitude of the magnetic moments of ^{14}N, $\mu_{^{14}N} = 0.404\mu_N$, and deuterium, $\mu_d = 0.86\mu_N$). However, an experimental study at SLAC (E143 experiment, unpublished) yielded a much lower value of $\frac{P_{^{14}N}}{P_d} \approx 0.33$. Therefore, a conservative assumption is to use a value 0.40 ± 0.08 for this ratio. The effective spin polarization of an isoscalar np pair inside ^{14}N

has been estimated (based on the Clebsch-Gordan coefficients of two independent nucleons in $p_{1/2}$ shells) as $\frac{P_{d\,in\,^{14}N}}{P_{^{14}N}} \approx -1/3$ [120], yielding the upper limit for D_n. Under the naïve assumption that both the magnetic moment and the total angular momentum $J = 1$ of ^{14}N is due (only) to the net orbital angular momentum L and spin S of pn pairs in ^{14}N, this factor is estimated to be $\frac{P_{d\,in\,^{14}N}}{P_{^{14}N}} \approx -0.25$. Combining the uncertainty ranges for both parameters yields the stated limits for D_n. While the individual terms have relatively large uncertainties, for the case of an $^{15}ND_3$ target this correction is tiny in comparison to η_p and can therefore be neglected. It is describe here only for future reference (if $^{14}ND_3$ or $^{14}NH_3$ targets are used).

The second term in the correction accounts both for bound protons in ^{15}N and free polarized protons due to isotopic impurities in the ammonia:

$$C_2^d A_p = \left(\eta_p f_{pol} \frac{P_p}{P_d} \frac{\sigma_p}{\sigma_d} + (1 - \eta_N) \frac{P_{^{15}N}}{P_d} \frac{g_{EMC}}{3} \frac{P_{p\,in\,^{15}N}}{P_{^{15}N}} \frac{\sigma_p^{bound}}{\sigma_d} \right) A_p \tag{43}$$

where A_p is the proton asymmetry, $A_\parallel(Q^2, W)$, with all corrections applied, except for the radiative correction. Here, the proton polarization (relative to that of the deuteron) is

$$P_p = \begin{cases} 0.191 + 0.683 P_d & \text{for} \quad P_d > 0.16 \\ 1.875 P_d & \text{for} \quad P_d \leq 0.16 \end{cases}$$

based on empirical studies [120]; for typical target polarizations $P_d \approx 0.25...0.35$, this yields $P_p/P_d \approx 1.2...1.5$. This correction applies only to free protons bound in ammonia molecules. The study in CLAS Note 2012 - 004 [119] showed that only a fraction f_{pol}, at most 1/2 of the most likely contamination $\eta_p = 0.035$, is polarized according to this equation; therefore, a safe range of values for the first term is $\eta_p f_{pol} \frac{P_p}{P_d} \approx 0.018...0.028$. The factor $\frac{P_{^{15}N}}{P_d}$ is again estimated, via the equal spin temperature hypothesis, to be in the range $-0.4... - 0.5$. However, due to the wave function of ^{15}N, the unpaired proton in this nucleus has a negative polarization compared to the nucleus as a whole, $\frac{P_{p\,in\,^{15}N}}{P_{^{15}N}} \approx -0.2... - 0.33$, where the first number uses again the naive assumption that nucleon spin and angular momentum account for both the magnetic moment $\mu_{^{15}N} = -0.26\mu_N$ and the total angular momentum $J = 1/2$ of ^{15}N, while the upper estimate uses a simple shell-model ansatz (namely, the Clebsch-Gordan coefficients for a $p_{1/2}$ state). Therefore, the second term in this correction is positive and is of order $0.026...0.055 \frac{\sigma_p^{bound}}{\sigma_d}$.

Finally, to calculate C_2^d (and, in the second version, C_1^d) one needs the ratios of free, $\frac{\sigma_p}{\sigma_d}$, and bound, $\frac{\sigma_p^{bound}}{\sigma_d}$, proton over deuteron cross sections (note that the deuteron cross section is *not* to be taken "per nucleon" in our convention). These ratios not only depend on kinematics, but also crucially on the reaction under discussion. For inelastic, inclusive scattering (i.e., the main goal of this analysis note), one can assume $\frac{\sigma_p}{\sigma_d} \approx \frac{\sigma_p^{bound}}{\sigma_d} \approx 0.5...0.75$. In this case, combining all factors yields the recommended range for $C_2^d \approx (0.039 \pm 0.012) A_p$.

On the other hand, when extracting $P_b P_t$ from exclusive D$(e, e'p)$n data, these cross section ratios depend strongly on the cuts chosen. In particular, within our exclusive kinematic cuts, $\frac{\sigma_p^{bound}}{\sigma_d} \approx 0.2$ since the bound proton in ^{15}N has a much broader momentum distribution than the one in deuterium, most of which falls outside our cuts. (The value 0.2 quoted comes directly from the ratio of background over signal for this channel within our cuts; for an alternative approach see below). In contrast, the ratio $\frac{\sigma_p}{\sigma_d} > 1$ in this case, since only the protons inside deuterium contribute to σ_d and our cuts are even more efficient for free protons than for those inside deuterium. Using a realistic momentum distribution for p inside d, we assume that this ratio can be as much as 2. Therefore, in this case the recommended range is $C_2^d \approx 0.044...0.073 A_p$. A second change is that for this case, *all* asymmetries in question can be assumed to be proton asymmetries: $A_D = A_p$. This yields a new equation for the relationship Eq. 36:

$$A_\parallel = \left(A_\parallel^{true} + C_2 A_p\right) / C_1 = \frac{1 + C_2}{C_1} A_p \tag{44}$$

This means that one should multiply the measured asymmetry $A_\parallel$ with the factor

$$\frac{C_1}{1 + C_2} \approx \frac{1 + \eta_p \frac{\sigma_p}{\sigma_d}}{1 + \eta_p f_{pol} \frac{P_p}{P_d} \frac{\sigma_p}{\sigma_d} + (1 - \eta_N) \frac{P_{^{15}N}}{P_d} \frac{g_{EMC}}{3} \frac{P_{p\,in\,^{15}N}}{P_{^{15}N}} \frac{\sigma_p^{bound}}{\sigma_d}} \approx 0.98 - 1.03 \tag{45}$$

before using it to extract $P_b P_t$. Here, we ignore the (tiny) contribution from ^{14}N and assume that the background was subtracted using scaled Carbon (and potentially empty) target data, which means C_1^d is taken from Eq. 39.

An alternative approach to estimate the ratio $\frac{\sigma_p^{bound}}{\sigma_d}$ makes use of the fact that about 62% of the total background for the channel D$(e, e'p)$n comes from the seven bound protons in ^{15}N (based on the various amounts of different target materials), so $\sigma_p^{bound} \propto 0.62 n_B / 7$. Correspondingly. $\sigma_d \propto (n^+ + n^- - n_B)/3$ (since there are three

deuterons in ammonia), so that we can write

$$\frac{\sigma_p^{bound}}{\sigma_d} \approx \frac{3}{7}\frac{0.62 n_B}{n^+ + n^- - n_B}. \tag{46}$$

The asymmetry used to extract $P_b P_t$ can therefore be recast as

$$\begin{aligned} A_{qe} &= A_{theor} P_b P_t = \frac{n^+ - n^-}{n^+ + n^- - n_B} \times \\ &\qquad \frac{1 + \eta_p \frac{\sigma_p}{\sigma_d}}{1 + \eta_p f_{pol} \frac{P_p}{P_d}\frac{\sigma_p}{\sigma_d} + (1-\eta_N)\frac{P_{^{15}N}}{P_d}\frac{g_{EMC}}{3}\frac{P_{p\,in\,^{15}N}}{P_{^{15}N}} 0.266 \frac{n_B}{n^+ + n^- - n_B}} \\ &= \frac{n^+ - n^-}{\frac{1+\eta_p f_{pol}(P_p/P_d)(\sigma_p/\sigma_d)}{1+\eta_p(\sigma_p/\sigma_d)}(n^+ + n^- - n_B) + 0.0886 n_B \frac{(1-\eta_N)(P_{^{15}N}/P_d)(P_{p\,in\,^{15}N}/P_{^{15}N})}{1+\eta_p(\sigma_p/\sigma_d)}} \\ &= \frac{n^+ - n^-}{a(n^+ + n^-) - b n_B} \end{aligned} \tag{47}$$

with

$$a = \frac{1 + \eta_p f_{pol}(P_p/P_d)(\sigma_p/\sigma_d)}{1 + \eta_p(\sigma_p/\sigma_d)} \tag{48}$$

and

$$b = \frac{1 + \eta_p f_{pol}(P_p/P_d)(\sigma_p/\sigma_d) - 0.0886(1-\eta_N)(P_{^{15}N}/P_d)(P_{p\,in\,^{15}N}/P_{^{15}N})}{1 + \eta_p(\sigma_p/\sigma_d)} \tag{49}$$

For the extraction of $P_b P_t$ from the exclusive quasi-elastic asymmetry as described in the previous section, we find that $a = 0.99 \pm 0.02$ and $b = 0.98 \pm 0.02$.

The net effect of these corrections, when applied to both the inelastic data and the calculation of $P_b P_t$,is a few percent of the extracted asymmetry. The uncertainties in the values of the correction factors, C_1^d and C_2^d, are considered as part of our systematic error calculations. For the proton asymmetries we used our model which has been fine-tuned to agree with the proton data at a very good level and doesn't introduce any further statistical uncertainty. However, the systematic uncertainty due to this proton model is fully included in our budget. Whenever a systematic variation of the final physics results due to models is studied, we vary the proton model consistently at all points where it entes the calculation - from radiative corrections over the proton contributions to deuteron observables, and also in the correction described in this section. This accounts for all correlations between errors due to these model uncertainties.

I.6 RADIATIVE CORRECTIONS

Our goal is to extract asymmetries for a single photon exchange process, known as Born scattering. However, there are higher order QED processes contributing to the measured asymmetries. These contributions are corrected for by the radiative corrections (see the EG1b proton analysis note for details). The corrections can be separated into two categories: internal and external radiative corrections.

The internal radiative corrections account for higher order QED processes that may occur during the interaction. These include internal Bremsstrahlung, where the incoming or the scattered electron emits a photon; vertex correction, in which a photon exchange occurs between the incoming and the scattered electron; and vacuum polarization of the virtual exchange photon. The corrections for the internal radiative effects have been calculated following Kuchto and Shumeiko [121].

The external radiative corrections (calculated using the prescription by Mo and Tsai [122]) account for the energy loss of the electron while passing through the detector and target material, mainly by the Bremsstrahlung process. As an electron traverses the target it can radiate a real photon, which changes the energy of the scattering process. Corrections for this effect depend crucially on the details of the experimental conditions. Therefore, a slightly different target model than that for the proton, taking all materials and their linear densities into account, was used in calculating these external corrections (see Table 5).

For both internal and external bremsstrahlung, the resulting energy loss may affect the reconstructed kinematics. The effect becomes especially important for the so-called elastic tail because the elastic cross section grows rapidly as the beam energy decreases, which increases the probability for radiation of a high energy photon followed by elastic scattering. This creates a radiative elastic tail in the inelastic region which is most pronounced at high W (low scattered electron energy E'). We applied a cut of $E'/E > 0.2$ to all events to exclude the region with large corrections from this effect.

For the radiative corrections in the EG1b experiment, an iterative, model dependent program called RCSLACPOL was used. For detailed information on the theoretical basis of this software, the reader is referred to [121][122][123]. The radiative corrections to the measured asymmetries for the deuteron are calculated in a completely analog way to those for the proton (see the EG1b proton analysis note). Here we only give a brief summary and highlight any (minor) differences.

The program creates a table of multiplicative and an additive correction term, $1/f_{RC}$ and A_{RC}. These correction terms were generated for each beam energy in our standard (Q^2, W) bins. The correction is applied to the asymmetry $A_{||}$, as the last correction before the calculation of the virtual photon asymmetries,

$$A_{||}^{Born} = \frac{A_{\|}^{corr}}{f_{RC}} + A_{RC}. \tag{50}$$

The additive term, A_{RC}, corrects for the asymmetry of elastic, quasi-elastic (deuterium only) and inelastic radiative tails. The multiplicative term, $1/f_{RC}$, which is always larger than 1, corrects for the "dilution" due to the (unpolarized) radiative elastic and quasielastic (deuterium) tail underneath the inelastic region. Since $0 \leq f_{RC} \leq 1$, we can interpret the measured asymmetry consisting of a fraction f_{RC} of the true asymmetry and a fraction $1 - f_{RC}$ of the contaminating asymmetry. In practice, this multiplicative factor is used to properly propagate the statistical errors from the raw asymmetry to the extracted Born asymmetry.

As in the case of the proton, we generated tables for f_{RC} and A_{RC} for each kinematic bin using our models for polarized and unpolarized structure functions and asymmetries of protons and neutrons in the elastic, quasi-elastic, resonance and DIS region (see next Section). Separate tables for different model input as well as variations of target parameters were generated for systematic studies. Apart from systematic errors due to the target model, all model inputs were varied simultaneously for the radiative corrections and for the other parts of the analysis, to properly account for correlations in the corresponding systematic errors.

I.7 MODEL INPUT

Knowledge of the structure functions F_1 and R as well as the virtual photon asymmetry A_2 is necessary to extract the physics quantities of interest, namely A_1 and g_1, from the EG1b double spin asymmetry data. Moreover, the deep inelastic contributions to the integral over g_1 require knowledge of A_1, A_2 and F_1 beyond the measured kinematics for a full evaluation of the moments. Eqs. (90-95) provide a brief summary of these calculations and the usage of these quantities. Finally, the radiative corrections discussed above require models of all these quantities over the full DIS and resonance region, including the regions unmeasured by the experiment. Therefore, parameterizations based on the existing world data were used for these

models. A package originally developed by the E143 collaboration [46] and maintained by S. Kuhn and N. Guler generates values of all physics quantities of interest based on these world data parameterizations. The results of the present experiment were used, in an iterative approach, to refine these models.

The models are under continuous development as new data become available on the asymmetries and the structure functions. Especially the models on A_1 and A_2 in the resonance region went through an extensive upgrade with the inclusion of many experiments, including EG1b. Studies of the parameterizations of the virtual photon asymmetries in the resonance region are provided in chapter III. The first part of the present section describes the models of the unpolarized structure functions. In the second part, we will give the current status of the virtual photon asymmetries in the DIS region.

I.7.1 Models of the unpolarized structure functions for the deuteron

For the purposes outlined above, we needed models for the unpolarized structure function F_1 and the ratio $R = \sigma_L/\sigma_T$ of longitudinal to transverse virtual photon absorption cross-sections, for protons, neutrons and for the deuteron. We used the parametrizations developed by P. Bosted and E. Christy for the proton [125] and the neutron [124] for F_1 and R in the inelastic region. Bosted and Christy [124] also use the nucleon structure functions and form factors to model the deuteron inelastic and quasi-elastic response. They kinematically smear the elastic and inelastic response of the nucleons (to simulate the effect of Fermi motion) using a table of the Paris wave function. An additional correction accounts for extra strength observed in the "dip region" between the quasi-elastic peak and the Delta resonance in deuterium beyond the quasi-free approximation (most likely due to meson exchange currents). (The deuteron elastic response, needed for its radiative tail, was modeled using the known deuteron form factors).

In the DIS region,we used the most recent parametrization of world data by the HERMES collaboration [126]. Together with a fit of R (R1998 [127]), one can extract F_1. In all cases, the assumption $R_p \approx R_n \approx R_d$ was made.

As a reference, plots for R and F_1 models of the deuteron are shown for various Q^2 bins in Fig. 15.

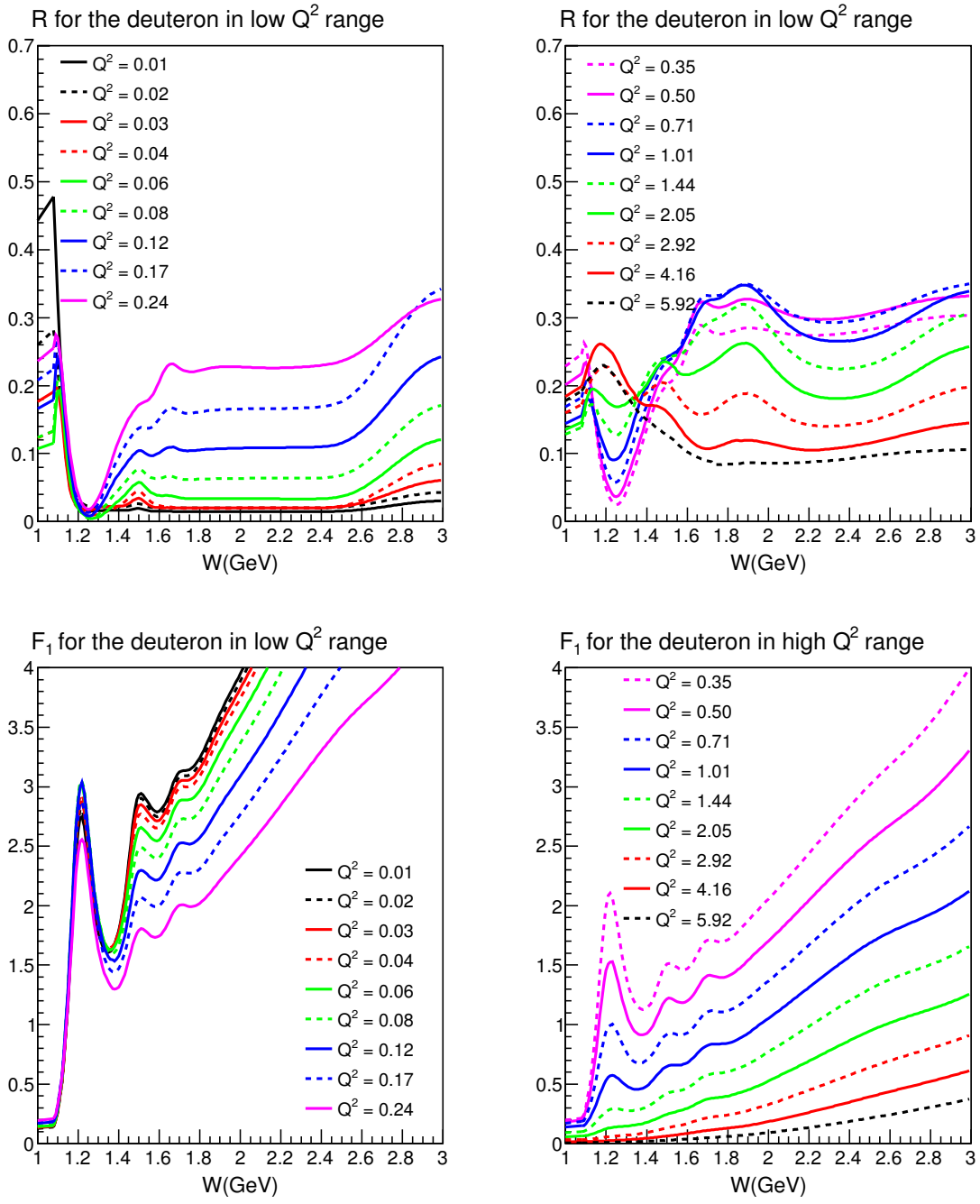

FIG. 15: The models for R (top) and F_1 (bottom) for the deuteron are shown for various Q^2 bins.

I.7.2 Models of A_1 and A_2 in the DIS region

The proton and neutron models for A_1 in the DIS region were produced by parameterizing the world data. The A_1^p parametrization included data from EMC [7], SMC [45], E143 [46], E155 [48], HERMES [49], EG1a [69] and EG1b [18]. The A_1^n parametrization included data from measurements on ^{3}He targets (E142 [44], E154 [47], HERMES [49] and Hall-A [71]) as well as ND_3 targets (E143 [46], E155 [48], HERMES [49], SMC [45], COMPASS [50], EG1a [68] and EG1b [51]). We also used real photon data from ELSA [128][129] and MAMI [130] for both parameterizations to constrain the fit as $Q^2 \to 0$. The data on A_1^n were used as presented by the experiments with the ^{3}He target. In order to extract neutron data from ND_3 measurements, we used the simplified assumption:

$$A_1^d = (1 - 1.5w_D)\left[\frac{F_1^p A_1^p + F_1^n A_1^n}{F_1^p + F_1^n}\right] \tag{51}$$

and solved the equation for A_1^n using models for A_1^p and the unpolarized structure functions $F_1^{p,n}$. In the end, the A_1^p fit utilized the following parametrization:

$$A_1^p = \xi^{P_1 + P_2 \tan^{-1}(P_3^2 Q^2)}[1 + (P_4 + P_5 \tan^{-1}(P_6^2 Q^2)) \sin(\pi \xi^{P_7})], \tag{52}$$

while the parametrization for A_1^n was

$$A_1^n = \xi^{P_1}[(P_2 + P_3 \tan^{-1}(P_4^2 Q^2)) \sin(\pi \xi^{P_5}) - \cos(\pi \xi^{P_6})], \tag{53}$$

where P_i represents parameter i. We also allowed the overall scale of each experiment to vary within the stated systematic error by employing additional parameters for each experiment. The kinematic variable ξ in the parameterizations was defined by

$$\xi = \frac{Q^2 + (M + M_\pi)^2 - M^2}{M(\nu + \sqrt{\nu^2 + Q^2})}, \tag{54}$$

where M is the nucleon mass and M_π is the mass of the $\pi^0 = 0.135$ GeV/c^2. The error on the fit was calculated by using the error matrix E_k^j determined by the minimization routine such that $\delta A_1 = \partial_j E_k^j \partial^k$, where $\partial_i = \partial A_1 / \partial P_i$ is the derivative of A_1 with respect to parameter P_i, and summation is implied over repeating indexes. Fig. 16 shows some results for both A_1^p and A_1^n fits. Afterwards, the deuteron model was obtained by using Eq. (51), with the corresponding error calculated by

$$\delta A_1^d = \frac{1 - 1.5w_D}{F_1^p + F_1^n}[(F_1^p)^2 (\delta A_1^p)^2 + (F_1^n)^2 (\delta A_1^n)^2]^{1/2}. \tag{55}$$

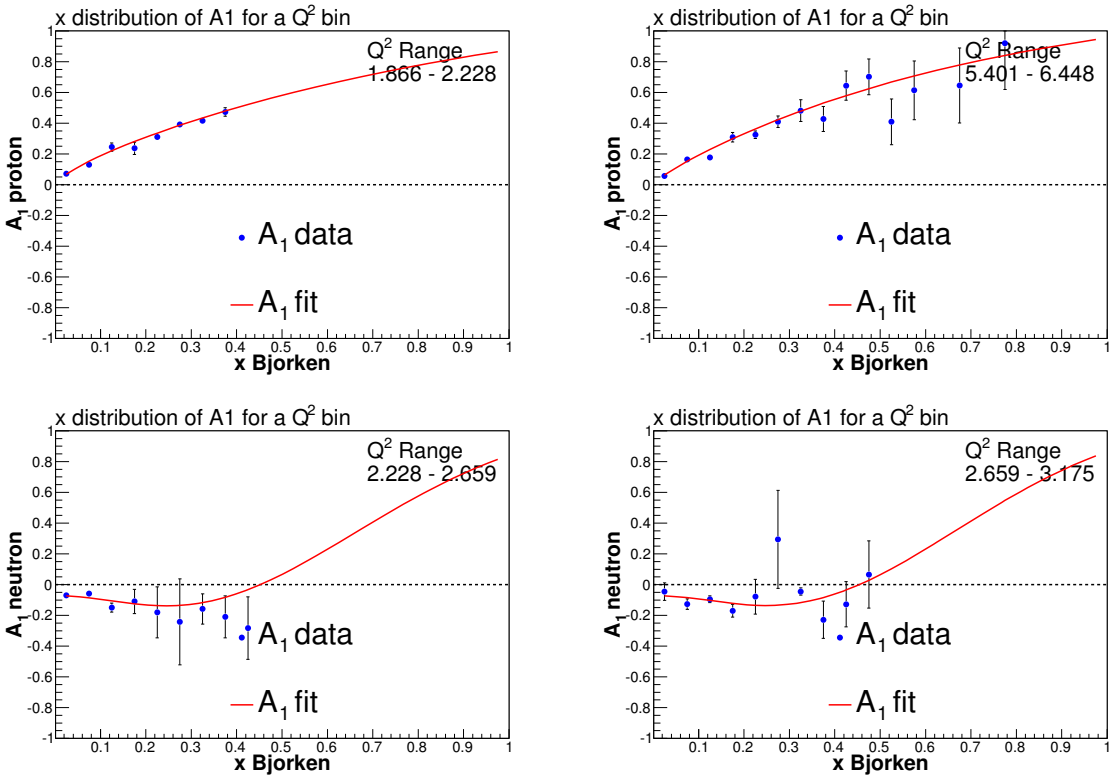

FIG. 16: The A_1 fits in the DIS region for the proton (top) and neutron (bottom).

A_2 in the DIS region was calculated by using the the *Wandzura-Wilczek* [8] relation for g_2^{WW}, which yields

$$A_2 = \gamma \frac{g_T^{WW}}{F_1} \tag{56}$$

where F_1 comes from our model and g_T^{WW} was calculated by solving

$$g_T^{WW} = \int_x^1 \frac{g_1}{y} dy \tag{57}$$

iteratively in terms of our A_1 and F_1 models, without considering the higher twist contributions. The higher twist contributions were taken into account for the systematic error on the model by including twist-3 calculations. After the calculations of both A_2^p and A_2^n, the asymmetry A_2^d for the deuteron was determined as a weighted sum of the two by using F_1 as a weight factor (similar to Eq. (51)).

In order to ensure a smooth transition between the resonance and the DIS regions, the parameterizations for A_1 and A_2 in the DIS region were constrained to "behave regularly" when extrapolated into the resonance region. In particular, we used the

constraint $A_1 = 1$ for $W = 1.07$, the inelastic threshold. (This is expected in all realistic QCD models for $x \to 1$, as well as from arguments based on parton-hadron duality). The asymmetries in the resonance region were then modeled as a combination of this DIS extrapolation, resonant terms (from MAID) and earlier models and fit to the data. Details are described in chapter III since the process uses our own EG1b data in an iterative fashion.

I.8 COMBINING DATA FROM DIFFERENT CONFIGURATIONS

As in the proton analysis, we want to combine data taken with different beam, target and detector configurations within the same kinematic (Q^2, W) bin to extract results with the smallest errors possible. Different runs can differ in the following parameters:

1. Beam energy
2. Torus polarity
3. Target material and polarization (including direction of polarization, along (+) or opposite (−) to the beam direction)
4. $\lambda/2$-plate status (in = 1 or out = 0)

The procedure used follows closely that for the proton. Below we give a short summary as reference for the reader.

I.8.1 Combining runs

Events from all runs belonging to the same beam energy, torus current (including sign) and target polarization (including sign) were added together to calculate the first set of raw asymmetries, $A_{raw}(W, Q^2)$, for each kinematic bin. This includes summing over runs with opposite status of the "half-wavelength" ($\lambda/2$) plate. Such a set of runs is called a *group, "G"*. The advantage of summing over a relatively large set of runs is that the asymmetries for each bin will be distributed more like a Gaussian around the "true" values, with errors that are not excessively large in general. This makes combining such asymmetries more straightforward and less error-prone. Events from matching helicity pairs are summed in two counters, N_0 and N_1, which are the total inclusive counts for the two relative spin orientations (including the effect of the $\lambda/2$ plate):

1. $N0$ is incremented if beam and target spin are antiparallel

2. $N1$ is incremented if they are parallel.

Similarly, for each run the counters FC_0 and FC_1 are increased according to the lifetime gated Faraday Cup scaler sums for the two relative orientations, again taking the status of the $\lambda/2$ plate into account. After summing over all runs within a group, the asymmetry in a given bin is then calculated as:

$$A^G_{raw}(W,Q^2) = \frac{N_0 - (FC_0/FC_1)N_1}{N_0 + (FC_0/FC_1)N_1}. \tag{58}$$

The error on the asymmetry is, to a very good approximation, given by

$$\sigma_{A^G_{raw}}(W,Q^2) = \sqrt{\frac{1}{N_0+N_1}}. \tag{59}$$

At the same time, for future reference, we also need to determine the averaged values of several kinematic variables for each of the bins. Those variables are Q^2, ν and

$$W = (M^2 + 2M\nu - Q^2)^{1/2} \tag{60}$$

$$E' = E - (W^2 - M^2 + Q^2)/2M \tag{61}$$

$$x = Q^2/2M\nu \tag{62}$$

$$\gamma = \sqrt{Q^2}/\nu \tag{63}$$

$$\theta = \tan^{-1}\left(\sqrt{p_x^2 + p_y^2}/p_z\right) \tag{64}$$

$$\epsilon = \frac{2EE' - Q^2/2}{E^2 + E'^2 + Q^2/2} \tag{65}$$

$$\eta = \frac{\epsilon\sqrt{Q^2}/E}{1 - \epsilon E'/E}. \tag{66}$$

The averages of these kinematic variables for a given bin in Q^2 and W are calculated by simply calculating the quantity in question for each event in the bin, summing over all events within a group, and then dividing by the number of events in the bin for the group.

TABLE 17: t-Test results for combining sets with opposite target polarizations.

Target	E_{beam}(GeV)(Torus)	t_{ave}	$\sigma_{t_{ave}}$	χ^2	N_{bin}
ND_3	1606i	-0.0166	0.0243	1.002	1685
ND_3	1723o	0.0142	0.0213	1.022	2199
ND_3	2561i	0.0101	0.0211	1.018	2242
ND_3	2561o	-0.0046	0.0184	0.986	2955
ND_3	4238i	0.0031	0.0189	0.994	2791
ND_3	4238o	0.0223	0.0158	1.000	3976
ND_3	5615i	0.0128	0.0183	1.002	2986
ND_3	5725i	-0.0018	0.0185	1.030	2925
ND_3	5725o	0.0117	0.0157	0.996	4033
ND_3	5743o	0.0283	0.0158	1.004	3993

I.8.2 t-Test

Before combining two different groups with opposite target polarizations, we first want to ascertain whether their individual results are statistically compatible with each other. This allows us to discover previously unknown problems with particular groups (e.g., vastly different dilution factors), as well as showing us at what level *single spin* asymmetries might be present. We use a t-test for this purpose. For each kinematic bin, we define

$$t(W,Q^2) = \frac{A^{G1}_{raw}/P^{G1}_{rel} - A^{G2}_{raw}/P^{G2}_{rel}}{\sqrt{\sigma^2_{A^{G1}_{raw}}/(P^{G1}_{rel})^2 + \sigma^2_{A^{G2}_{raw}}/(P^{G2}_{rel})^2}}. \tag{67}$$

with the relative polarization P^G_{rel} as defined in section I.4.4. If the fluctuations between group 1 and group 2 are purely statistical, we expect that the distribution of t for the different bins is Gaussian with a mean of zero and a standard deviation (which is similar to χ^2) of 1. The mean t should be zero within the error on the mean, which is simply $1/\sqrt{N_{bins}}$. Large deviations from these expectations suggest that additional scrutiny of the two groups in question is warranted. Fig. 17 shows sample plots from the t-tests for 2.5 and 5.7 GeV data sets and Table 17 lists all obtained t values. As can be seen, the systematic difference between any two data sets with opposite polarization is at most 3% of the point-to-point statistical error, and within two standard deviations (or less) of the expected value of zero. The values for χ^2 are also all reasonable.

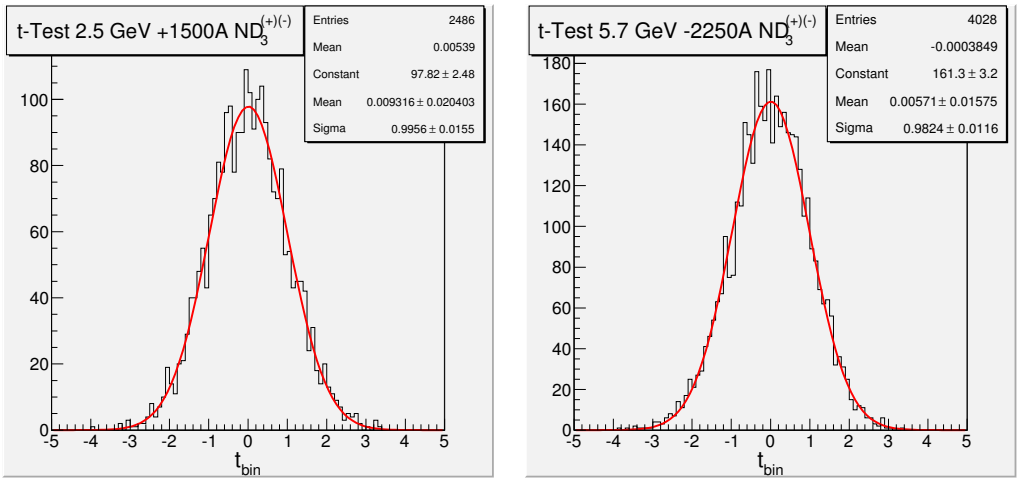

FIG. 17: Plots showing the distribution of $t(W, Q^2)$, in Eq. (67), for the t-Test between data sets with opposite target polarizations.

I.8.3 Combining opposite target polarizations

We combine the two groups with opposite target polarizations bin by bin, weighting each asymmetry with its statistical weight, $(P^G_{rel})^2/\sigma^2_{A^G_{raw}}$. The statistical error of the resulting combined asymmetry is

$$\sigma_{A^C_{raw}} = \sqrt{\frac{(P^{G1}_{rel})^2 + (P^{G2}_{rel})^2}{(P^{G1}_{rel})^2/\sigma^2_{A^{G1}_{raw}} + (P^{G2}_{rel})^2/\sigma^2_{A^G_{raw}}}}. \tag{68}$$

The average kinematic variables introduced earlier were also combined for each bin with the same statistical weights. The result for the 2 groups with opposite target polarizations combined is referred to as a "set" in the following. The only difference between the sets is their beam energy and torus currents.

Before continuing any further in combining runs, at this stage we converted the raw asymmetries by dividing out $P_b P_t$ and F_D for each set. In addition, the corrections for pion and pair-symmetric contaminations as well as the polarized background and the radiative corrections were all applied at this stage. Finally, the resulting values for $A^{Born}_{||}(W, Q^2)$ were converted to values for $A_1 + \eta A_2(W, Q^2)$ by dividing with the averaged D results (obtained from models) for each bin. All of these manipulations in principle depend on the beam energy and in case of contaminations, also on the torus polarity. The values for $A_1 + \eta A_2$, for each bin, as well as the averaged kinematic variables and the count rates are propagated into the next step.

I.8.4 Combining data with slightly different beam energies

At this stage we have 11 data sets. These sets are given in Table 2. Among these, there are sets with slightly different beam energies but the same torus current. These sets are:

- 1.606 GeV, −1500A ; 1.723 GeV, −1500A
- 5.615 GeV, +2250A ; 5.725 GeV, +2250A
- 5.725 GeV, −2250A ; 5.743 GeV, −2250A

The values for $A_1 + \eta A_2 \equiv A_{12}$ are combined for these sets by taking their error weighted average for each kinematic bin,

$$A_{12}^{mean}(W,Q^2) = \frac{A_{12}^{S1}/\sigma^2_{A_{12}^{S1}} + A_{12}^{S2}/\sigma^2_{A_{12}^{S2}}}{1/\sigma^2_{A_{12}^{S1}} + 1/\sigma^2_{A_{12}^{S2}}}, \tag{69}$$

$$\sigma_{A_{12}^{mean}}(W,Q^2) = \left(\frac{1}{1/\sigma^2_{A_{12}^{S1}} + 1/\sigma^2_{A_{12}^{S2}}}\right)^{1/2}. \tag{70}$$

The kinematic factor η does depend on the beam energy, however, it is relatively small for our kinematic region and varies only slightly for closely neighboring beam energies, which makes the combination of $A_1+\eta A_2$ for slightly different beam energies possible. Moreover, we applied a t-test in order to make sure that these data sets are compatible with each other for combining. The form of the t-test for this case is

$$t_{(W,Q^2)} = \frac{A_{12}^{S1} - A_{12}^{S2}}{\sqrt{\sigma^2_{A_{12}^{S1}} + \sigma^2_{A_{12}^{S2}}}} \tag{71}$$

for each of the overlapping kinematic bins. The average t-score,

$$t_{ave} = \frac{\sum\limits_{W,Q^2} t_{(W,Q^2)}}{N} \qquad \sigma_{t_{ave}} = \sqrt{\frac{1}{N}} \tag{72}$$

and the χ^2 values

$$\chi^2 \approx \sigma_t^2 = \left[\frac{\sum\limits_{W,Q^2} t^2_{(W,Q^2)}}{N}\right]^{1/2} \tag{73}$$

are monitored for each combination. Table 18 provides the overall result of this test.

TABLE 18: t-Test results for combining data with slightly different beam energies.

Target	E_{beam}(GeV)	t_{ave}	$\sigma_{t_{ave}}$	χ^2	N_{bin}
ND_3	1.606 - 1.723	0.0055	0.0231	0.99	1882
ND_3	5.615 - 5.725	-0.0289	0.0201	1.01	2465
ND_3	5.725 - 5.743	0.0917	0.0169	0.99	3497

As one can see, there is only one case where the t-value is unexpectedly large (nearly 10% or about 5 sigma), for the pair 5.725 GeV - 5.743 GeV. It should be noted that these two energy settings correspond to 1-month long run periods each, with potentially significant changes in running conditions. In any case, the systematic difference expressed by t should be compared to the known magnitude of the systematic error on these data sets as fraction of the statistical error, see Table 44 in Appendix C.2. This table shows that the systematic error due to the polarization product $P_b P_t$ alone (which is different for the two run periods) is about 20% of the statistical error in each W bin over most of Q^2. If the actual difference due to $P_b P_t$ between the two run sets is just 1/2 of this estimated systematic error, it would result in the value of t_{ave} observed in Table 18.

We also propagated the kinematic variables and the count rates to the next step. The kinematic variables are averaged between the two data sets by using the total counts for each set as a weighting factor, e.g.,

$$\langle Q^2 \rangle = \frac{Q^2_{S1} N_{S1} + Q^2_{S2} N_{S2}}{N_{S1} + N_{S2}}. \tag{74}$$

I.8.5 Combining data sets with opposite torus polarities

Opposite torus polarities for the same beam energy do not have any effect on the values of $A_1 + \eta A_2$. Therefore they can safely be combined in a straightforward way, taking error weighted averages. Therefore, we followed exactly the same prescription outlined in the previous section, using Eqs. (69) and (70). Again, we performed a t-test for each pair of data sets combined. Table 19 provides the results. The obtained t values are again in the few-% range and mostly within 2 sigma of the expected 0. They are also completely compatible with possible systematic differences between the data sets with opposite torus polarity, within the systematic errors.

At this point, before combining data sets with different beam energies, we need

TABLE 19: t-Test results for combining sets of opposite torus polarity.

Target	E_{beam}(GeV)(Torus)	t_{ave}	$\sigma_{t_{ave}}$	χ^2	N_{bin}
ND_3	1.6(+) - 1.6(−)	-0.0561	0.0283	0.99	1252
ND_3	2.5(+) - 2.5(−)	-0.0272	0.0252	0.98	1572
ND_3	4.2(+) - 4.2(−)	-0.0443	0.0219	1.01	2082
ND_3	5.7(+) - 5.7(−)	-0.0439	0.0197	1.00	2589

to extract A_1 and g_1 by using models for A_2 and F_1,

$$A_1(W,Q^2) = [A_1 + \eta A_2](W,Q^2) - \langle\eta\rangle A_2^{model}(W,Q^2) \tag{75}$$

$$g_1(W,Q^2) = \frac{F_1^{model}(W,Q^2)}{1+\langle Q^2\rangle/\langle\nu\rangle^2}\left[A_1(W,Q^2) + \frac{\sqrt{\langle Q^2\rangle}}{\langle\nu\rangle}A_2^{model}(W,Q^2)\right]. \tag{76}$$

These values, again, together with the kinematic variables, averaged according to Eq. (74), and the count rates for each bin are propagated to the next level of analysis.

I.8.6 Combining data sets with different beam energies

At this point we have 4 independent data sets, which we can label E^1, E^2, E^4 and E^5, corresponding to 1.x, 2.x, 4.x and 5.x GeV data sets. In each set, we have A_1, g_1, kinematic variables and the count rates for each bin. The A_1 and the g_1 values from different sets can be combined by taking their error weighted averages. The kinematic variables are, again, combined by weighting them with corresponding count rates in each bin. In this way, the data sets were combined, two at a time: first combining E^1 and E^2, then combining $E^{(1:2)}$ with E^4 and finally combining $E^{(1:2:4)}$ with E^5. We performed a t-test between each individual data set, as well as between the combined and the individual data sets. The results are given in Table 20. Similar comments apply as before - no t values exceed 6.2% which is smaller than the known systematic errors (as fraction of the statistical ones) of all data sets involved.

As a result, all data are combined into a single set, consisting of A_1 and g_1 values, as well as the properly averaged kinematic variables and the count rates, for W and Q^2 bins. In the next section, we will *s*ummarize the corrections applied on the asymmetries and describe how we propagated the statistical errors after each correction. Then we will outline the systematic errors and the final results for these quantities. All quantities of interest are presented in chapter II.

TABLE 20: t-Test results for combining data sets for g_1 with different beam energies.

Target	Beam Sets	t_{ave}	$\sigma_{t_{ave}}$	χ^2	N_{bin}
ND_3	E^1-E^2	0.0623	0.0265	0.98	1421
ND_3	E^2-E^4	-0.0487	0.0274	1.03	1330
ND_3	E^4-E^5	0.0565	0.0217	0.99	2118
ND_3	E^2-E^5	0.0482	0.0373	1.00	719
ND_3	E^1-E^4	-0.0271	0.0389	1.02	658
ND_3	$E^{(1:2)}$-E^4	-0.0358	0.0274	1.02	1330
ND_3	$E^{(1:2:4)}$-E^5	0.0527	0.0217	0.97	2118

I.8.7 Combining W bins for plotting

Our final results are created as a function of Q^2 and W. Section I.2 explains the kinematic values of our standard Q^2 and W bins. On the other hand, while demonstrating the results for various quantities, it is generally better to combine a few W bins and plot the average result in a larger kinematic range for better visibility. Therefore, we combined data in standard W bins within a $\Delta W = 40$ MeV range and plot the average results. For this purpose, the data from standard W bins were combined by taking their error weighted average:

$$\bar{x} = \frac{\sum_i x_i/\sigma_i^2}{\sum_i 1/\sigma_i^2} \tag{77}$$

$$\sigma_{\bar{x}}^2 = \frac{1}{\sum_i 1/\sigma_i^2} \tag{78}$$

where summation is performed within $\Delta W = 40$ MeV range. It should be pointed out that this kind of combination was only made for the data and its statistical error. We utilized a different method for the systematic errors, which will be explained in section I.10.

I.9 PHYSICS QUANTITIES AND PROPAGATION OF THE STATISTICAL ERRORS

The raw asymmetry is calculated from the count rates:

$$A_{raw}(Q^2, W) = \frac{N^+ - R_{FC}N^-}{N^+ + R_{FC}N^-} \tag{79}$$

where N^+ and N^- are total inclusive counts, for each bin, corresponding to the positive and negative helicity configurations, respectively. The quantity R_{FC} is the normalization factor,

$$R_{FC} = \frac{FC^+}{FC^-} \tag{80}$$

which is the ratio of accumulated Faraday cup charges for these helicity configurations. The statistical error on the raw asymmetry is given by

$$\Delta A_{raw} = \frac{2R_{FC}N^+N^-}{N^+ + R_{FC}N^-}\sqrt{\frac{1}{N^+} + \frac{1}{N^-}} \tag{81}$$

Later, pion and pair symmetric contaminations are determined. Since the pion contamination is small, it is only treated as a systematic error in the final results. The pair symmetric correction is applied to the raw asymmetry,

$$A_{corr} = A_{raw}C_{back} = A_{raw}\,\frac{1 - RA^{pos}/A_{raw}}{1-R} = \frac{A_{raw} - RA^{pos}}{1-R} \tag{82}$$

where R is the e^+/e^- ratio and A^{pos} is the positron raw asymmetry. The error on this quantity propagates as

$$\Delta A_{corr} = \sqrt{\frac{(\Delta A_{raw})^2 + R^2(\Delta A^{pos})^2}{(1-R)^2}} \tag{83}$$

The next step in the analysis is to determine the dilution factor, F_D, and the beam $\times$ target polarization, P_bP_t. The asymmetry corrected for these effects is

$$A_\parallel^{raw} = \frac{A_{corr}}{F_D P_b P_t}. \tag{84}$$

Although extraction of these quantities have their own statistical and systematic uncertainties, they are treated as part of our systematic error calculations. Thus, their uncertainties do not enter into the statistical error of the final results. The error on the $A_\parallel^{raw}$ is written as

$$\Delta A_\parallel^{raw} = \frac{\Delta A_{corr}}{F_D P_b P_t}. \tag{85}$$

Then we apply the polarized background corrections,

$$A_\parallel^{corr} = C_1\left(A_\parallel^{raw} - C_2A_p\right) \tag{86}$$

(see Section I.5). The uncertainty on C_2A_p is treated as a systematic error, and therefore

$$\Delta A_\parallel^{corr} = C_1\Delta A_\parallel^{raw} \tag{87}$$

with the factors C_1 and C_2 described in section I.5. Finally, radiative corrections are applied in the following form,

$$A_{\parallel}^{Born} = \frac{A_{\parallel}^{corr}}{f_{RC}} + A_{RC}, \tag{88}$$

and the statistical error becomes:

$$\Delta A_{\parallel}^{Born} = \frac{\Delta A_{\parallel}^{corr}}{f_{RC}}. \tag{89}$$

After all corrections described in the preceding sections, the final form of the corrected asymmetry, $A_{\parallel} \equiv A_{\parallel}^{Born}$, can be written as:

$$A_{\parallel} = \frac{C_1}{f_{RC}} \left(\frac{A_{raw}}{F_D P_b P_t} C_{back} - C_2 \right) + A_{RC}. \tag{90}$$

In the next stage, we can calculate the virtual photon asymmetry A_1:

$$A_1 = \frac{A_{\parallel}}{D} - \eta A_2, \tag{91}$$

where D is the depolarization factor described earlier. The statistical error on the virtual photon asymmetry is calculated as:

$$\Delta A_1 = \frac{\Delta A_{\parallel}}{D}. \tag{92}$$

The spin structure function g_1 is given by

$$g_1 = \frac{F_1}{1+\gamma^2} \left[\frac{A_{\parallel}}{D} + (\gamma - \eta) A_2 \right]. \tag{93}$$

The statistical error associated with the g_1 is

$$\Delta g_1 = \frac{F_1}{1+\gamma^2} \left[\frac{\Delta A_{\parallel}}{D} \right]. \tag{94}$$

Finally, we can calculate the moments of the spin structure function. The n^{th} moment is written as,

$$\Gamma_1^n(Q^2) = \int_0^1 g_1(x, Q^2) x^{n-1} dx. \tag{95}$$

The integral can be divided into small Δx ranges and expressed as a summation

$$\Gamma_1^n(Q^2) = \sum_{i=0}^{N} \int_{x_i}^{x_{i+1}} g_1(x, Q^2) x^{n-1} dx. \tag{96}$$

Then the individual bin integrals can be evaluated by parts

$$\int_{x_i}^{x_{i+1}} g_1(x,Q^2)x^{n-1}dx = g_1(x,Q^2)\left[\frac{x_{i+1}^n - x_i^n}{n}\right] - \frac{x^n}{n}\, d(g_1(x,Q^2)). \tag{97}$$

Since our bin sizes are small and we have a single g_1 value per bin, hence g_1 is constant within the infinitesimal range of the integration, $d(g_1(x,Q^2)) = 0$. Therefore, the second term in the right hand side vanishes, leaving us with

$$\Gamma_1^n(Q^2) = \sum_{i=0}^{N} \frac{x_{i+1}^n - x_i^n}{n} g_1(x,Q^2). \tag{98}$$

The small bin sizes we have validates this as a good approximation to a continuous integration. However, our data is in (W,Q^2) bins, so we need to determine the corresponding x for each bin. We used experimentally determined kinematic averages for x_{av} in each (W,Q^2) bin and calculated the n^{th} moment of g_1 as:

$$\Gamma_1^n(Q^2) = \sum_{W} \frac{x_{high}^n - x_{low}^n}{n} g_1(W,Q^2), \tag{99}$$

with

$$x_{high} = (x_{av[W]} + x_{av[W-1]})/2 \tag{100}$$

$$x_{low} = (x_{av[W]} + x_{av[W+1]})/2 \tag{101}$$

for a constant Q^2. The statistical error on this quantity is given by

$$\Delta\Gamma_1^n(Q^2) = \left(\sum_{W}\left[\frac{x_{high}^n - x_{low}^n}{n}\right]^2 \times [\Delta g_1(W,Q^2)]^2\right)^{1/2}. \tag{102}$$

where $\Delta g_1(W,Q^2)$ is the statistical error on $g_1(W,Q^2)$.

The final results on all of these quantities are presented in chapter II. In the following sections, we will describe how we handled systematic errors.

I.10 SYSTEMATIC ERROR CALCULATIONS

All applied corrections to the asymmetries and the structure functions as well as the model inputs required to calculate the final results are summarized in Eqs. (90-94). However, each of the correction factors as well as the model inputs for the A_2, F_1 and D [1] have their uncertainties.

[1]The depolarization factor D internally depends on the structure function R.

We chose to estimate the effect of these uncertainties on a given measured quantity by evaluating that quantity with the standard value of all corrections and model input and then repeat the evaluation with a model input or a parameter varied within uncertainties. The difference between these two results can be considered as the systematic error, due to that specific factor, on the quantity of interest. Therefore, the first step in the systematic error calculation is to determine the range of uncertainty for each factor that enters into the calculations. The analysis is first performed by using the standard values, which we can call standard measurement. Then it is repeated again by changing only one of the factors by the amount of its uncertainty while keeping all other quantities at their standard values. Consequently, the full analysis is repeated for each uncertain factor and several different systematic variations are obtained for each measured quantity. For example, if $A_1^{(s)}(W, Q^2)$ is the standard value for a given (W, Q^2) bin and $A_1^{(i)}(W, Q^2)$ is the value obtained by changing a factor i by its uncertainty, the systematic error on $A_1(W, Q^2)$ due to the uncertainty of i is calculated by

$$\delta A_1^{(i)}(W, Q^2) = |A_1^{(s)}(W, Q^2) - A_1^{(i)}(W, Q^2)| \tag{103}$$

The total systematic error $\delta A_1^{(tot)}(W, Q^2)$, is then calculated by adding all the systematic uncertainties in quadrature:

$$\delta A_1^{(tot)}(W, Q^2) = \left(\sum_i [\delta A_1^{(i)}(W, Q^2)]^2 \right)^{1/2} \tag{104}$$

The main factors that enter into the systematic error calculations are:

1. Pion and pair symmetric background
2. Dilution factor
3. Beam $\times$ target polarization
4. Polarized background
5. Radiative correction
6. Errors on model asymmetries and structure functions

However, it should be noted that, for each item on this list, there may be several sub-parameters varied during the analysis. Overall there are 27 parameters as listed

in Table 21. In order to make this procedure quick and automatic, an error index array was used in the analysis program. Each subprocess in the program looks for the status of the index in the array corresponding to its specific correction and decides whether the correction should be applied at the standard value or the boundary value of the parameter. Each index in the array is turned on or off, "on" meaning the systematic change should be applied to that parameter. Then, the whole analysis code is put into a loop over all values of the index array. For each repetition, one element of the index array is turned on to create the systematic results of the analysis. Table 21 lists the elements of the error index array and describes the corresponding variations. In addition, Appendix section C.2 provides detailed tables of systematic errors for individual Q^2 bins as a percentage of the statistical errors. This quantity is calculated as the quadratic mean of the ratio of the systematic error to the statistical error,

$$\sigma_{sys}^{percent}(Q^2) = \sqrt{\frac{1}{N}\sum_{W}\frac{\sigma_{sys}^2(Q^2,W)}{\sigma_{stat}^2(Q^2,W)}} \times 100 \tag{105}$$

where N is the number of W bins entering into the summation. Tables 41-44 summarize the systematic errors on $A_1 + \eta A_2$ for each data set with different beam energy settings and provides the individual contributions from different sources. Also, Table 45 gives the total systematic errors on A_1, together with the different sources, and Table 46 provides the systematic errors evaluated in different W regions.

The following sections describe the different systematic variations in more detail. Before continuing to the individual systematic error definitions, it should also be noted that the systematic errors were evaluated independently for standard W bins of 10 MeV and the combined W bins of 40 MeV. While the data and the statistical errors from standard bins were combined within $W = 40$ MeV range as explained in section I.8.7, the systematic errors cannot be combined in that fashion. Therefore, the full analysis was performed for the combined bins the same way it was done for the standard bin size by running over all systematic variations and adding the systematic differences in quadrature for the combined data. Similarly, for any other quantity of interest we calculated from the data, we used the same approach: going through the full chain of analysis for this quantity, for each variation of a parameter, and again adding the variations of the final result in quadrature. This applies to quantities like g_{1d} as well as moments thereof, and also to the extracted values for g_{1n}.

TABLE 21: Systematic error index and corresponding variations to each index element.

Error Index	Variation
0	Standard analysis
1	Pion background correction
2	Pair symmetric correction varied
3	Dilution factor varied
4	Radiative corrections varied
5 - 16	$P_b P_t$ varied for each beam energy
17 - 22	Model inputs
23 - 25	Place holder for further model inputs
26 - 28	Polarized background corrections

I.10.1 Pion and pair-symmetric backgrounds

Most of the pion background was removed by precise identification of electrons including the geometrry and timing cuts ("Osipenko cuts", see [1]) on the CC. Studies on the remaining pion background revealed a very small amount of pion contamination in the electron sample. Since it is very small, the total amount of this contamination was treated as a systematic error. The effect of the remaining pion contamination on the raw asymmetry can be quantified as

$$A_{corr} = \frac{A_{raw} - R_\pi A^\pi}{1 - R_\pi} \tag{106}$$

where $R_\pi = \pi^-/e^-$ ratio and $A^\pi \approx 0$ is the pion asymmetry. The difference between the corrected value and the uncorrected value was used to estimate the systematic error due to the remaining pion contamination. (This is equivalent to assuming an uncertainty of $\delta A^\pi = \pm A^e$).

In order to determine the systematic uncertainty in the pair-symmetric contamination, the average contamination over all θ and momentum bins, weighted by the errors on the fit parameters, were compared for opposing torus polarities for the same beam energy. Half of that difference was added to the e^+/e^- ratio and the asymmetry was corrected by using the new value. In case there were not data for both torus polarities for a particular beam energy, such as the 1.7 and 5.6 GeV data sets, the comparison was made with the closest beam energy. The total systematic error due to the pion and pair symmetric backgrounds is less than 1% of the asymmetry.

I.10.2 Dilution factor

The dilution factor analysis was performed by R. Fersch, who precisely determined the overall systematic uncertainty on this quantity. The main source of error in determining the dilution factor was the target model parameters, namely, the uncertainties in the physical measurements of the various materials in the target: the lengths and the densities of the carbon, Kapton and aluminum as well as the frozen ammonia target. In order to estimate the systematic error on the dilution factors, these parameters were changed by a reasonable amount [1].

The dilution factor was obtained by two independent methods, first one relying on data and the second one relying on a model, as described in section I.3. This model used a world data parametrization of unpolarized cross sections. Eventually, the results obtained by using the model were used for the final analysis. However, the systematic errors from the model were not determined. Therefore, in addition to the systematic uncertainties on the target parameters, model uncertainties should also be considered in the systematic error calculation. This was done by comparing the dilution factors obtained from the two different methods. However, the results from the first method had bin to bin statistical fluctuations, so a direct comparison would result in an error dominated by these statistical fluctuations, which are not characteristic for systematic error. Also, that approach would not be possible for some kinematic regions, where we had poor data but the model dependent dilution factors were determined by extrapolation. Therefore, a fit to the dilution factors obtained from the data was generated and a comparison between this fit and the model-based dilution factors were used as part of the systematic error on this quantity. For more detailed information, please refer to [1].

I.10.3 Beam and target polarizations

As described in section I.4, the product of beam and target polarization was extracted using data. The main source of error on this quantity is of a statistical nature. The full error also contains a systematic uncertainty coming from the factors a and b described in Section I.5. Both factors are varied (by 0.02) within their uncertainties and the polarization product is reevaluated. The resulting variations for either factor are added in quadrature to the statistical error (which dominates).

The error on $P_b P_t$ was not propagated as a statistical error. Instead ,it was added

to the value of the polarization used for the standard analysis, for one data set at a time, keeping others unchanged. The full analysis was repeated 12 times, each corresponding to a change in the polarization of one data set. Then the differences between the standard analysis and the systematic analysis were added in quadrature to determine the total systematic error due to the uncertainties in the $P_b P_t$ extraction. The $P_b P_t$ extraction was done by using the exclusive method for all data sets except the 1.6 and 1.7 GeV ND_3 sets with negative torus polarity. For these specific data sets, the inclusive method of extraction was used with a 10% error on the value, which is twice and three times larger than the statistical error obtained from the inclusive method, respectively. For the inclusive method, dilution factors were used but because of the overestimated statistical errors on these data sets, the correlation in the systematic errors between the dilution factor and $P_b P_t$ can be safely neglected.

I.10.4 Polarized background

The correction factors C_1 and C_2, described in section I.5, have uncertainties that are not well defined. For the standard correction, the values $C_1 = 1.03$ and $C_2 = 0.039 A_p$ were used, where A_p is the proton asymmetry. The systematic error was determined using three variations:

1. $C_1 = 1.02$ was used
2. $C_2 = 0.027$ was used
3. the model for A_p was varied by its uncertainty. This happens "automatically" when the models are varied (see below) - such variations are *simultaneously* applied to all places where a given model enters.

As a result to the first 2 variations, this correction yields an average systematic error of about 2% to 6% of the statistical error on $A_1 + \eta A_2$.

I.10.5 Radiative corrections

Radiative corrections have uncertainties stemming from the target model used (for external radiation) and from the models for structure functions used to calculate radiative tails. The former uncertainty was evaluated by varying our target model within reasonable parameters, while the latter was again "automatically" taken care of by the variation of models described below. In particular, radiative correction

tables were calculated for each variation of the models, and the corresponding tables were applied whenever the models were varied. This follows exactly the procedure for the proton analysis and is described in more detail in Ref. [1].

I.10.6 Systematic errors due to models

The models used for F_2, R (and thus F_1), as well as A_1 and A_2 in the DIS region, are described in Section I.7. In all cases except for $A_2(DIS)$, the models were based on multi-parameter fits with systematic uncertainties quantified by the parameter uncertainties or by direct comparison with data. For all systematic effects due to these model uncertainties, we varied each of the models for F_2, R and $A_1(DIS)$ by these fit uncertainties in turn. For $A_2(DIS)$, we used an alternative model with a twist-3 part, g_T^{HT} added to the standard Wandzura-Wilczek form. Finally, for the models of A_1 and A_2 for both the proton and the neutron in the resonance region (see Section III), we used alternative versions derived from earlier fits of a more limited data set.

In all cases, any change in one model was propagated to all steps in the analysis where this particular model is used to properly evaluate the systematic correlations of such changes.

CHAPTER II

PHYSICS RESULTS

The results from the analysis are presented in this section by showing comprehensive plots of the physics quantities extracted. The main goal of the analysis is to measure the double spin asymmetry $A_{\parallel}$ with all corrections given in Eq. (90) and extract $A_1 + \eta A_2$, A_1, g_1 and Γ_1 for the deuteron. It should be noted that the quantities in the following figures are averaged over the final state invariant mass W in 40 MeV bins. The systematic errors for the averaged results were obtained with the usual procedure by independently running the whole analysis on each quantity for each systematic uncertainty.

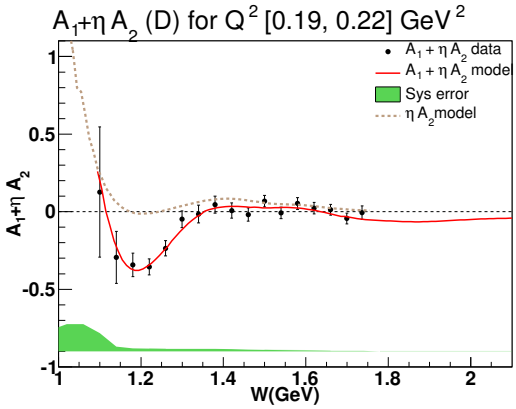

(a) 1.6 GeV

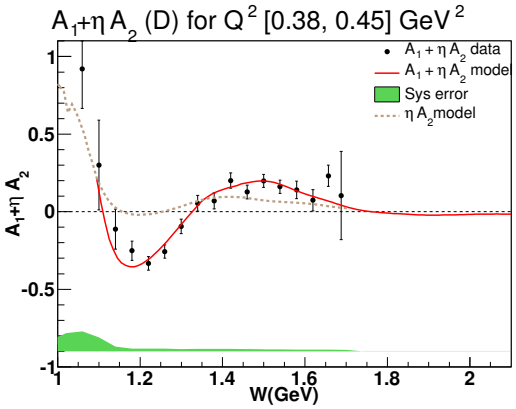

(b) 1.6 GeV

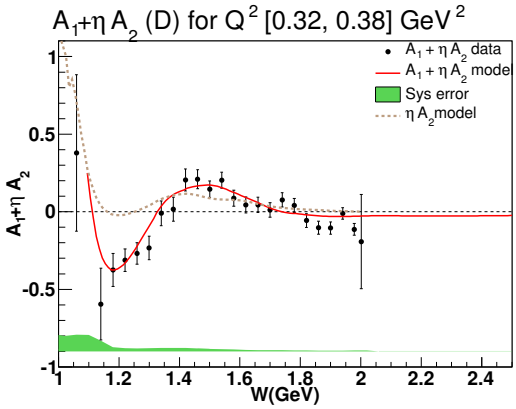

(c) 2.5 GeV

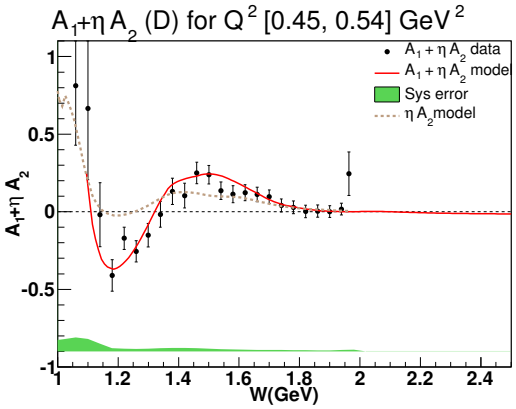

(d) 2.5 GeV

FIG. 18: $A_1 + \eta A_2$ versus final invariant mass W for 1.6 and 2.5 GeV beam energy settings. The Q^2 bin is given at the top of each plot. The red-solid and brown-dotted curves are $A_1 + \eta A_2$ and ηA_2 parameterizations, respectively. The green shade represents the total systematic error on $A_1 + \eta A_2$.

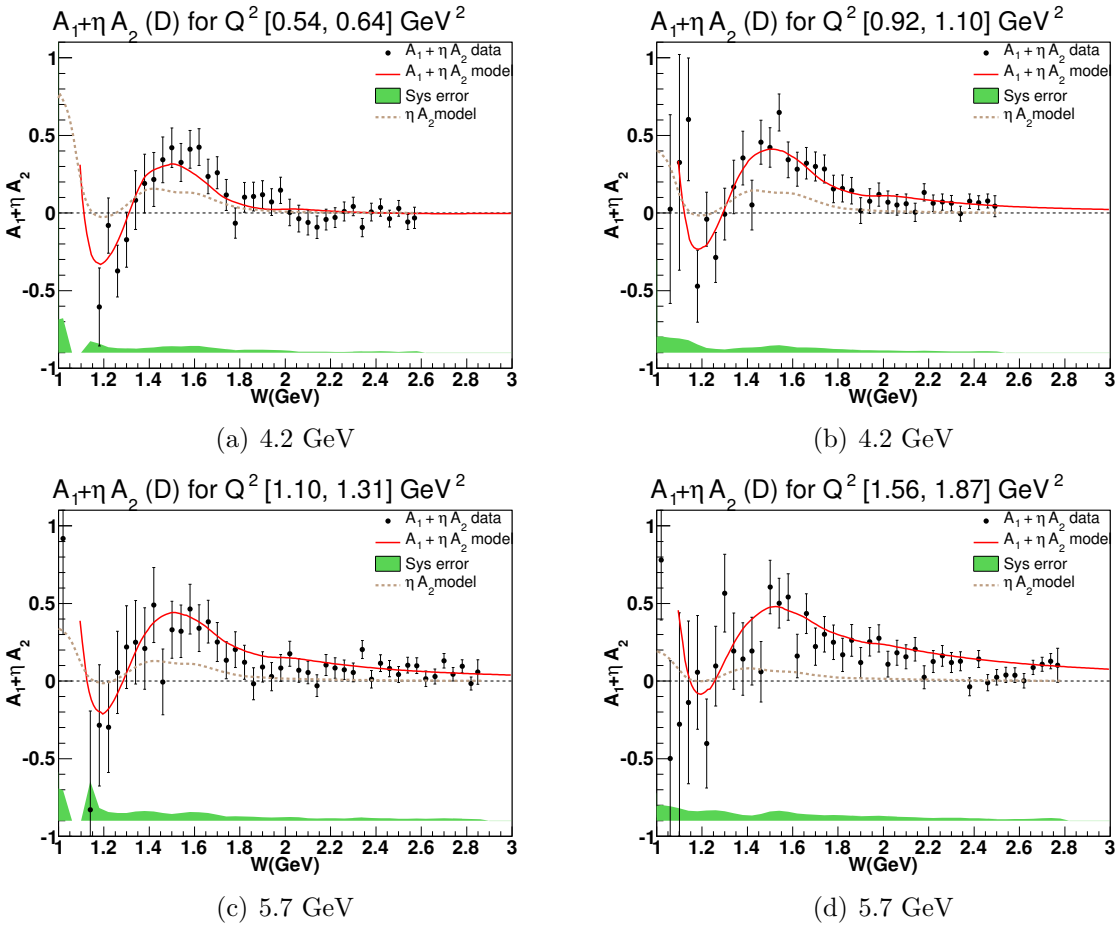

(a) 4.2 GeV (b) 4.2 GeV

(c) 5.7 GeV (d) 5.7 GeV

FIG. 19: $A_1 + \eta A_2$ versus final invariant mass W for 4.2 and 5.7 GeV beam energy settings. The Q^2 bin is given at the top of each plot. The red-solid and brown-dotted curves are $A_1 + \eta A_2$ and ηA_2 parameterizations, respectively. The green shade represents the total systematic error on $A_1 + \eta A_2$.

Figures 18 and 19 show the results for $A_1 + \eta A_2$ for selected Q^2 bins for various beam energy settings. Fig. 20 explicitly provides the systematic errors on this quantity from different contributing elements. Once $A_1 + \eta A_2$ is calculated, we can extract the virtual photon asymmetry A_1, by using model inputs for A_2. Fig. 21 shows this quantity together with different sources of systematic errors. In addition, Figs. 22 and 23 show the final A_1 versus final state invariant W mass for all Q^2 bins in our kinematic coverage. At low Q^2, the effect of the $\Delta P_{33}(1232)$ resonance is clearly visible which proves that the $A_{3/2}$ transition is dominant in this region as expected, causing the asymmetry to be negative. As we go to higher values of W, the transition $A_{1/2}$ becomes dominant leading to resonances such as $D_{13}(1520)$ and $S_{11}(1535)$.

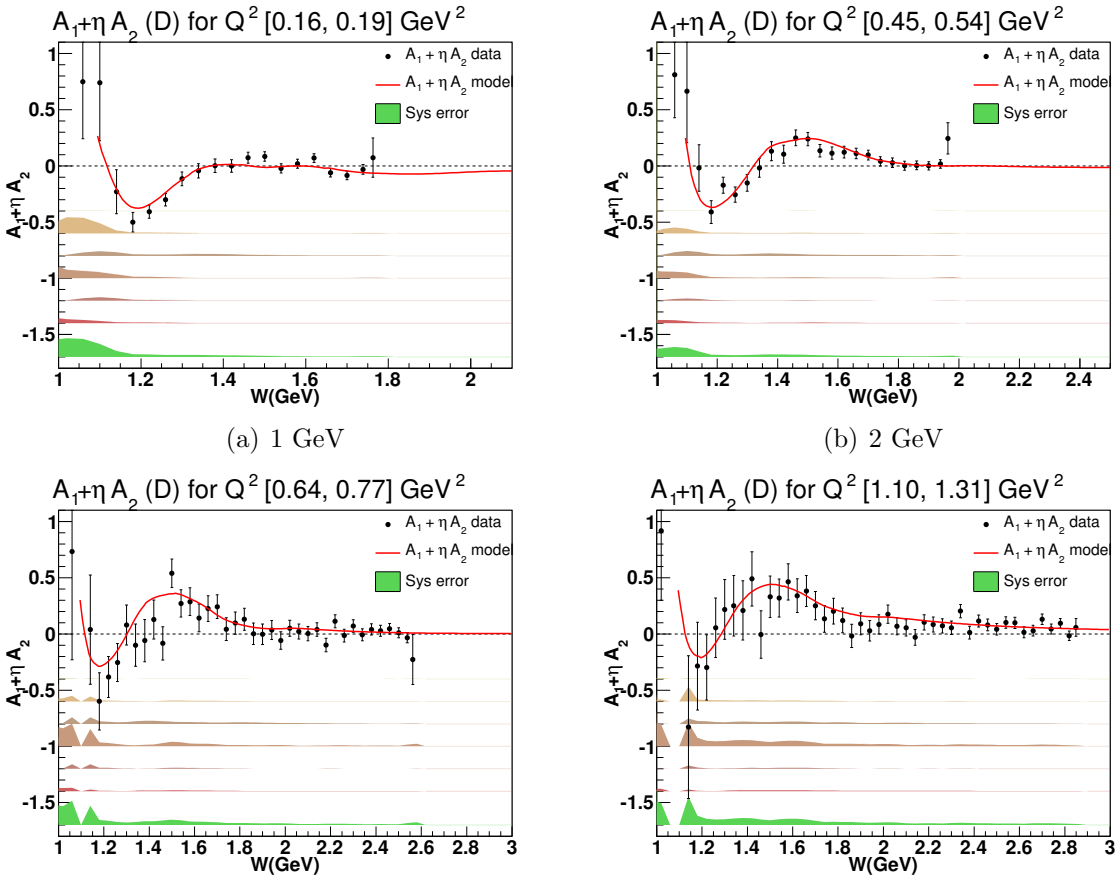

(a) 1 GeV (b) 2 GeV

(c) 4 GeV (d) 5 GeV

FIG. 20: $A_1 + \eta A_2$ versus W together with different sources of systematic error. The shade at the bottom (green) is the total systematic error. The other systematic errors are offset to the following vertical scales, from top to bottom: pion and pair symmetric contamination (-0.4); dilution factor (-0.6); radiative correction (-0.8); $P_b P_t$ (-1.0); models (-1.2); polarized background (-1.4). At this point, the biggest source of our systematic error comes from the $P_b P_t$ extraction.

By using Eq. (93) and taking F_1 and A_2 from models, the spin structure function g_1^d is evaluated for each bin. Figs. 24 and 25 show its behavior with respect to W. In addition, g_1^d versus Bjorken x for each Q^2 bin are also presented in Figs. 26 and 27. The red curve on each plot comes from the our "Models". g_1 is deeply affected by the resonance structure, again the $\Delta(1232)$ being the most prominent one, making g_1 negative in this region. When we go to higher Q^2, the effect of the resonances diminishes and g_1 approaches zero toward the quasi-elastic region.

The moments of the structure functions are calculated by integrating the structure

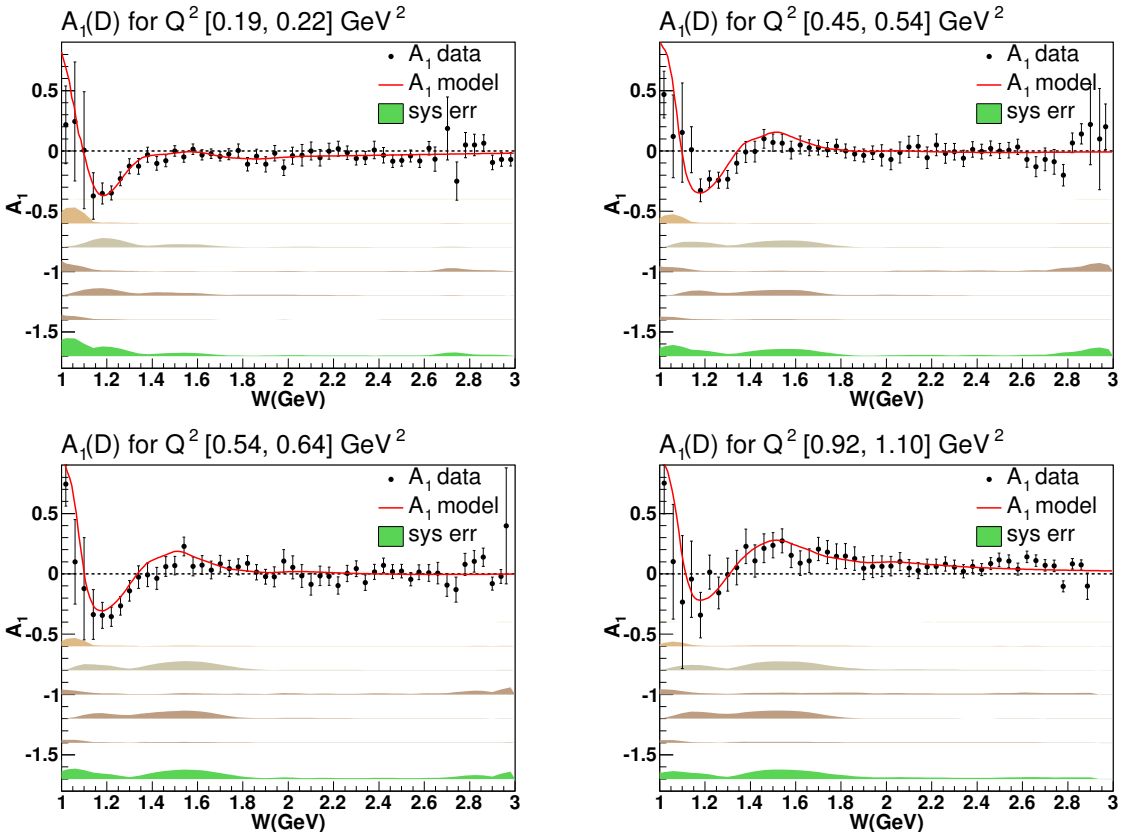

FIG. 21: Virtual photon asymmetry A_1 versus W for a few Q^2 bins are shown together with systematic errors. The shade at the bottom is the total systematic error. The other systematic errors are offset to the following vertical scales, from top to bottom: pion and pair symmetric contamination (-0.4); dilution factor (-0.6); radiative correction (-0.8); $P_b P_t$ (-1.0); models (-1.2); polarized background (-1.4). Uncertainity from the A_2 models is a major conributer to the overall systematic error for A_1. This systematic error can be reduced once we have measurements on A_2.

functions over the full kinematic region from $x = 0.001$ up to the quasi elastic threshold x at $W = 1.08$ GeV. By using the relation,

$$W = \sqrt{M^2 + Q^2/x - Q^2} \tag{107}$$

the maximum W values for the kinematic point $x = 0.001$ were determined for each Q^2 bin from $Q^2 = 0.01$ to 10 GeV^2.

Experimental limitations prevent us from exploring the region where $x \to 0$ since it would require a very high beam energy. At the limit $x = 0.001$, the invariant mass reaches up to 100 GeV. Moreover, the extrapolation of the integral is not well known below $x = 0.001$. Therefore, this kinematic region was excluded from the integration.

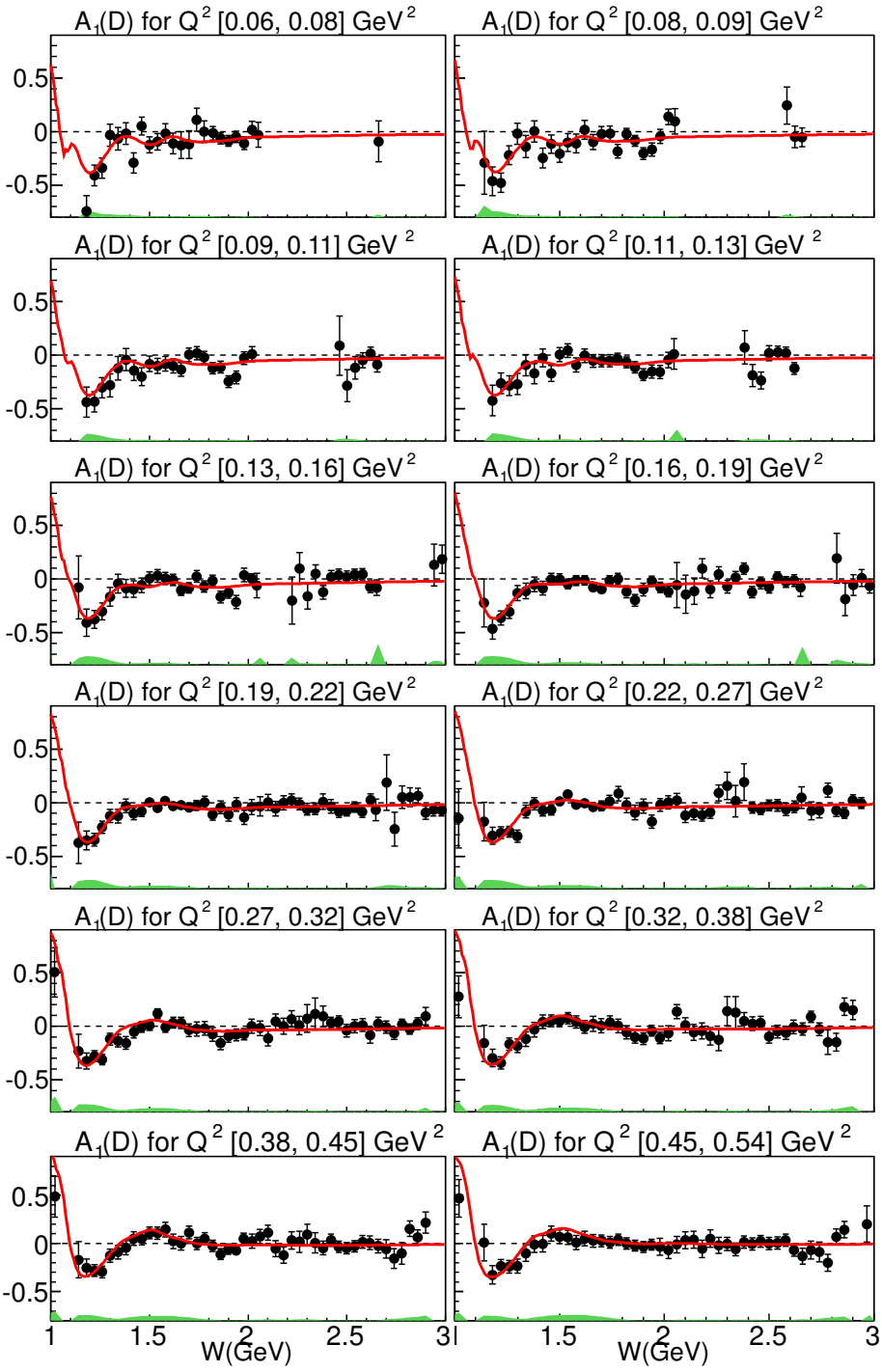

FIG. 22: A_1 for the deuteron versus the final state invariant mass W for various Q^2 bins. Systematic errors are shown as shaded area at the bottom of each plot. Our parametrized model is also shown as a red line on each plot. Only the data points with $\sigma_{stat} < 0.3$ and $\sigma_{sys} < 0.2$ are plotted.

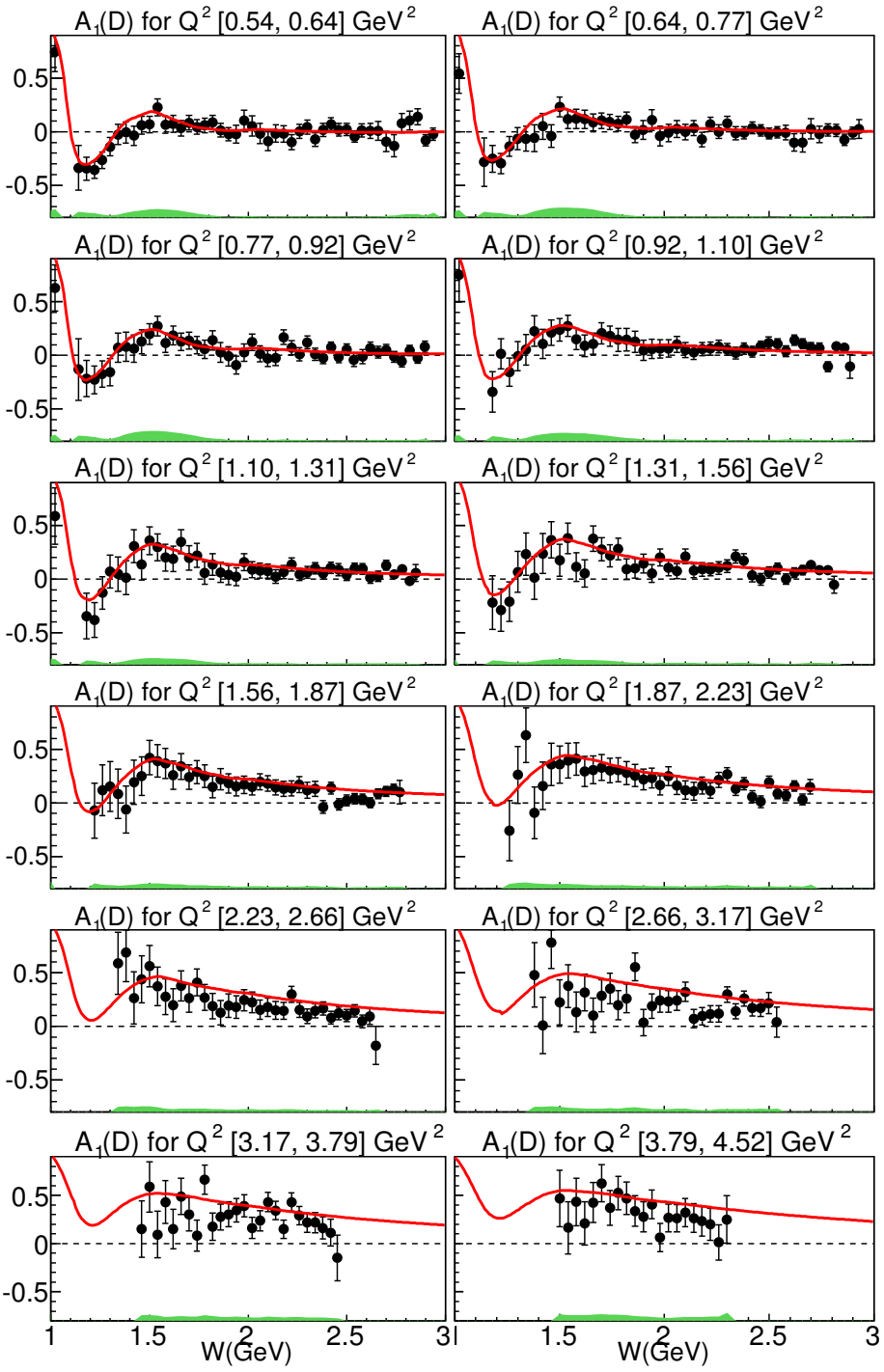

FIG. 23: Continuation of Fig. 22 for remaining Q^2 bins.

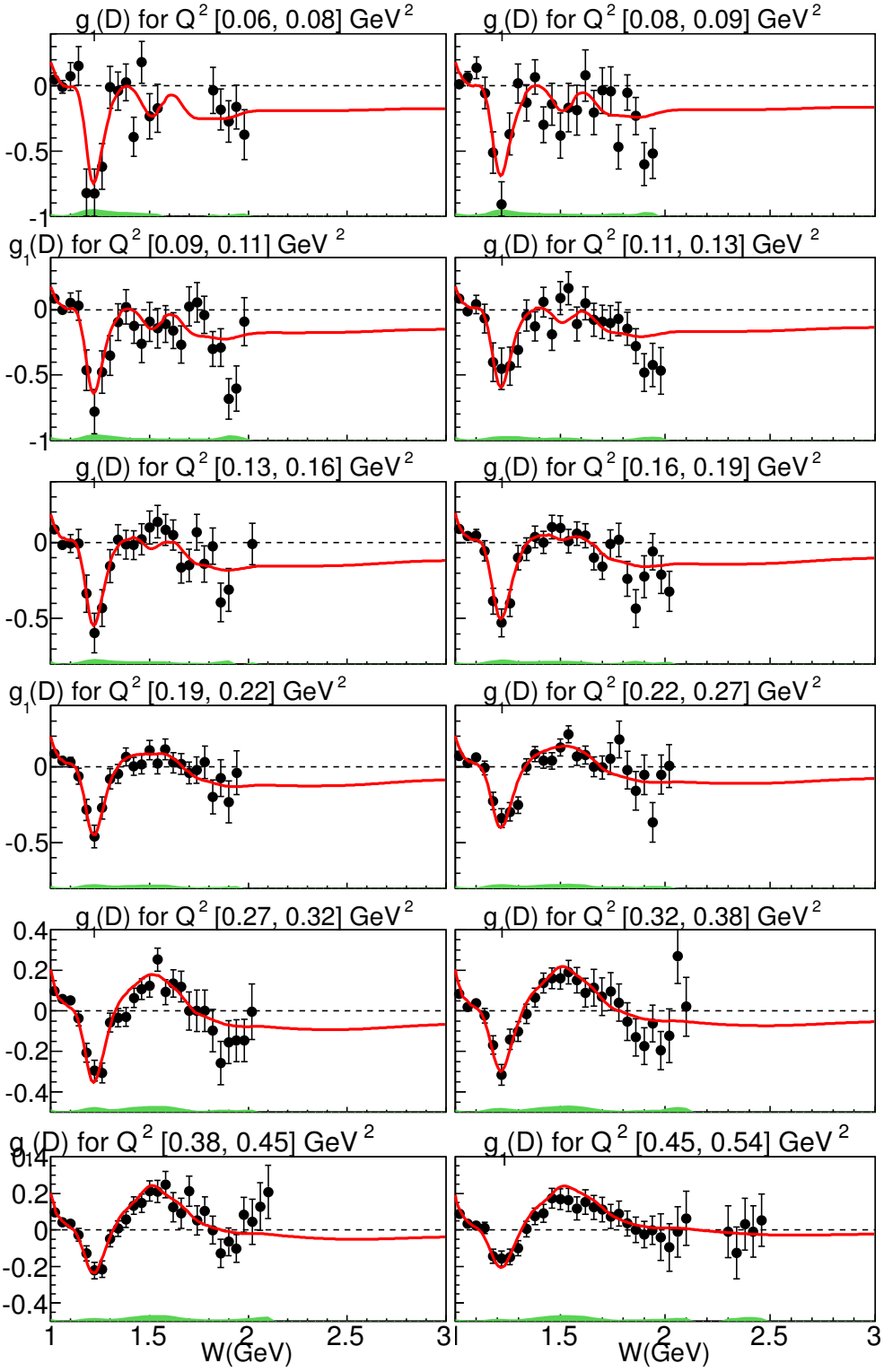

FIG. 24: g_1 for the deuteron with respect to the final state invariant mass W for many Q^2 bins. The shaded area at the bottom of each plot represents the systematic errors. Model for g_1 is shown as a red line on each plot. Only data points with $\sigma_{stat} < 0.2$ are plotted.

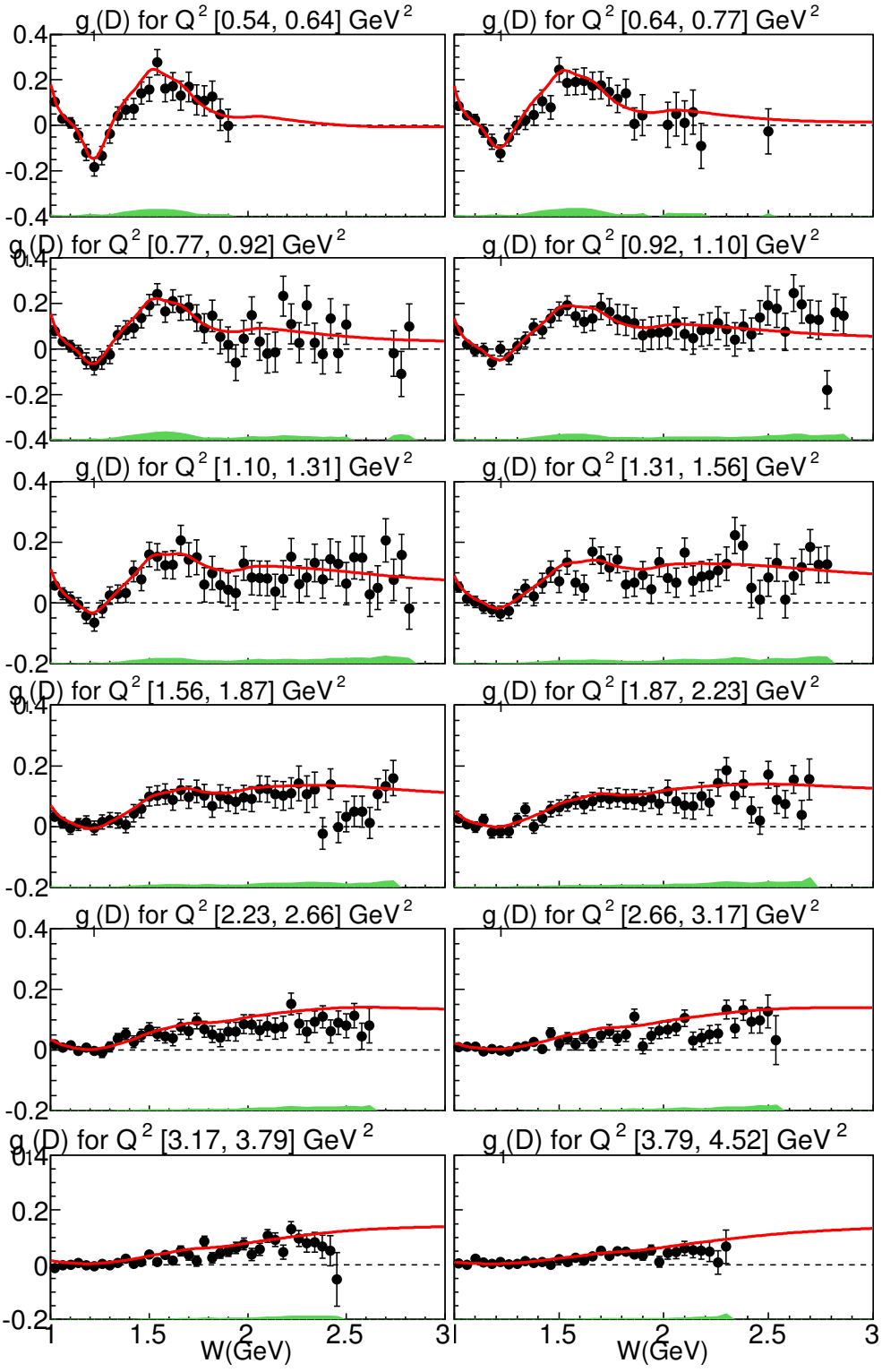

FIG. 25: Continuation of Fig. 24 for remaining Q^2 bins.

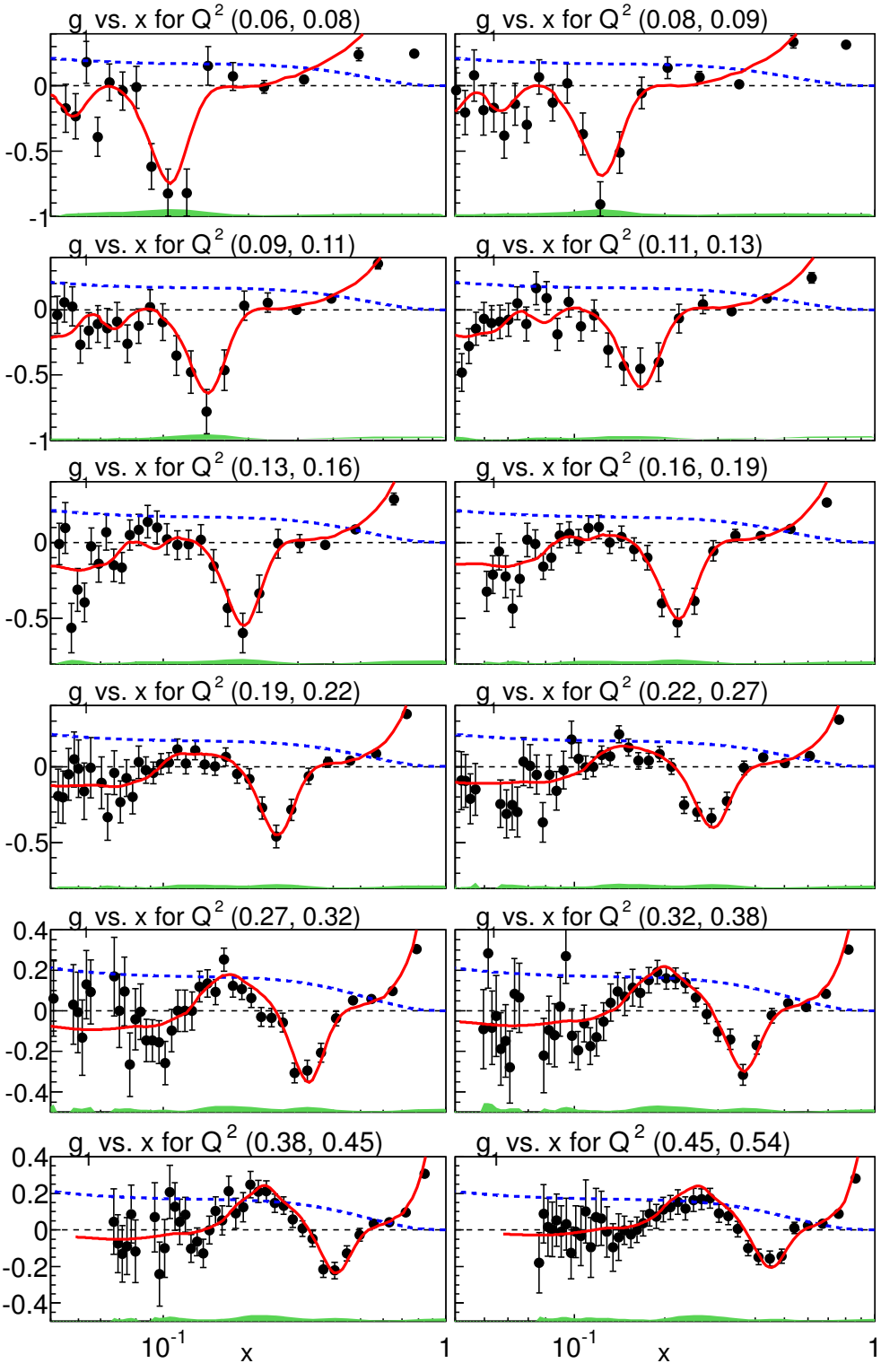

FIG. 26: g_1 with respect to the Bjorken variable x for many Q^2 bins together with model shown as red lines on each plot. The shaded area at the bottom of each plot represents the systematic error. DIS curve for $Q^2 = 10$ GeV is also shown as blue dashed line.

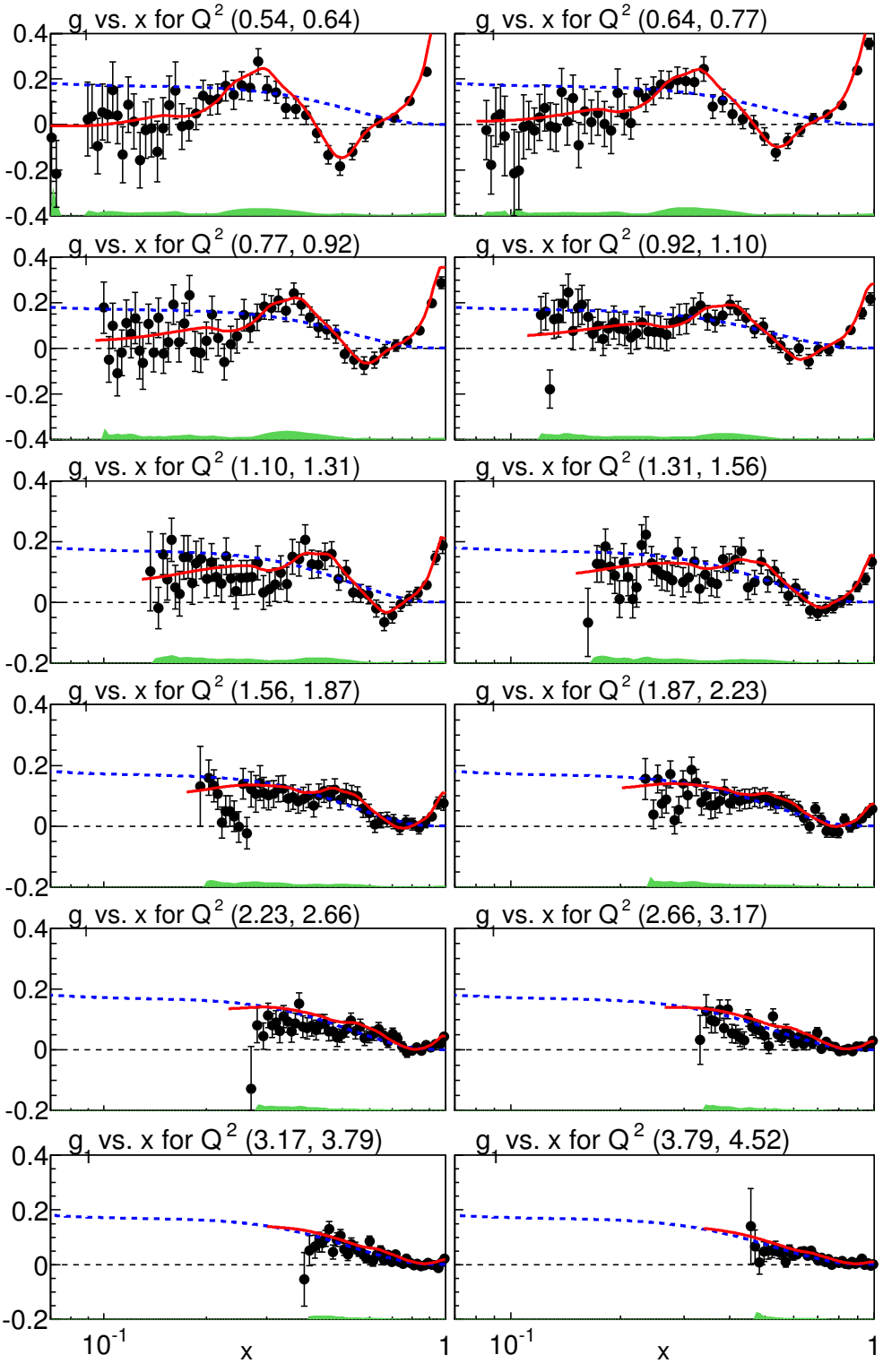

FIG. 27: Continuation of Fig. 26 for remaining Q^2 bins.

The minimum W value was always kept at 1.08 GeV, which is the quasi-elastic threshold. Convention for the evaluation of the moments generally excludes the quasi-elastic region. The low Q^2 behavior of Γ_1 is more interesting without the elastic contribution since the effect of the Δ resonance becomes more obvious.

The described limits of the integration require model input since the EG1b results do not cover the full kinematic region. Therefore, the model values for g_1 were used where data are not available. The regions for which we use either the data or the model were determined by scanning through the quality of the data for different W regions in each Q^2 bin. Data with large statistical errors were excluded from the integration. The EG1b data for the structure function g_1 starts at $W = 1.15$ GeV, since below that region the radiative effects overwhelm the real data. However, we have a reliable model that can be used for the integration. Above this value, we have data up to $W = 3$ GeV depending on the Q^2 bin. Figs. 26 - 27 show the behavior of g_1 data for all Q^2 bins used in the integration. Also, there are some gaps in our data that correspond to uncovered regions because of discrete beam energies. These gaps appear only for a few Q^2 bins and model values were used for the integration in those regions. Table 47 in Appendix C.3 summarizes the W regions in which the values from the model or the data were used for the integration. An additional constraint can also be put on the data by considering the average kinematic points we have extracted from the data and propagated up to this point. These kinematic variables include ϵ, η and γ for each bin, so that one can calculate a cut parameter y such that,

$$y = \frac{\nu}{E_{beam}} = \frac{\eta(1-\epsilon)}{\epsilon(\gamma-\eta)}. \tag{108}$$

Then, a requirement $y < 0.80$ can be used to select the regions for which data can be used for the integration. If data with large statistical errors are used in the integration, these statistical errors will clearly be visible in the relevant Q^2 values of the moments.

With above considerations, the integral can be divided into measured and unmeasured regions such that,

$$\begin{aligned}\Gamma_1(Q^2) = &\int_{x=0.001}^{x(W_{data})} g_1(x,Q^2) \quad \text{model} \\ &+ \int_{x(W_{data})}^{x(W=1.15)} g_1(x,Q^2) \quad \text{data (or model for gaps)} \\ &+ \int_{x(W_{1.15})}^{x(W=1.08)} g_1(x,Q^2) \quad \text{model}\end{aligned} \tag{109}$$

and each integration is performed according to Eqs. (99) and (102). For comparison purposes, the plots of Γ_1 will usually show the results of the integration using only the data and using the data and model together. Of course the result obtained by only using the data will deviate from the true value since the integral is not complete. However, there are Q^2 regions where the overall model contribution to the integral is very small and the data alone gives a good approximation to the full integral. In those kinematic points, the results obtained from the data alone and from the data + model together come very close to each other. Figs. 28 - 30 show the Q^2 evolution of the first moment as measured by the EG1b experiment and also the current status of the world data on this quantity. The higher moments Γ_1^3 and Γ_1^5 are also calculated in the same way by using Eq. (99) with appropriate powers $n = 3, 5$. Fig. 31 shows the results for the third moment Γ_1^3 and the fifth moment Γ_1^5 of g_1 as extracted from the EG1b data.

Fig. 32 shows the forward spin polarizability γ_0 for the deuteron. Values calculated are multiplied by 15.134 for unit conversion to [10^{-4} fm^4]. The figure also shows the integral part of γ_0 without the kinematic factor $16M^2\alpha/Q^6$. Additional information on γ_0 is provided in the proton analysis note.

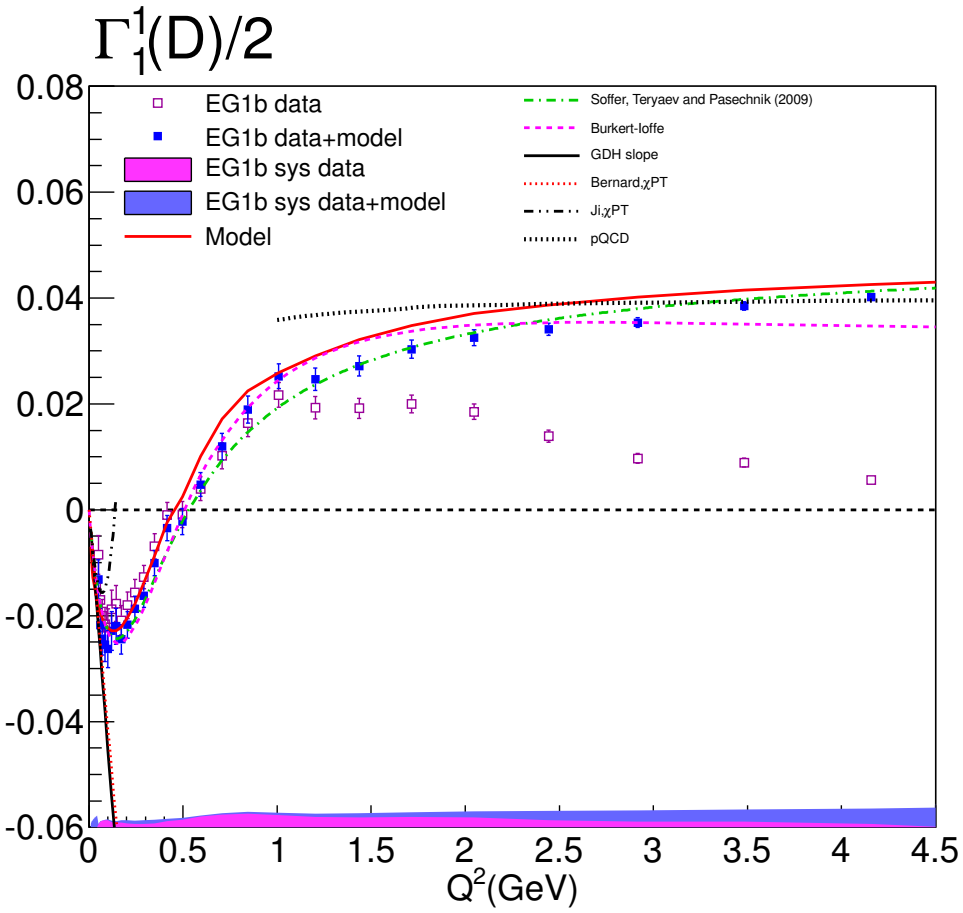

FIG. 28: Γ_1^1 for the deuteron versus Q^2 from data only (hollow-magenta squares) and data+model (full-blue squares), including the extrapolation to the unmeasured kinematics. The red curve is evaluated by only using the model. Also shown are phenomenological calculations from Soffer-Teryaev and Burkert-Ioffe, together with the χPT results from Ji [60] (black dotted dashed line) and Bernard [61] (red dotted line). The GDH slope (black solid line) and pQCD prediction (black dotted line) are also shown on the plots . The systematic errors are shown for only data (magenta shade) and data+model (blue shade) at the bottom of the plot.

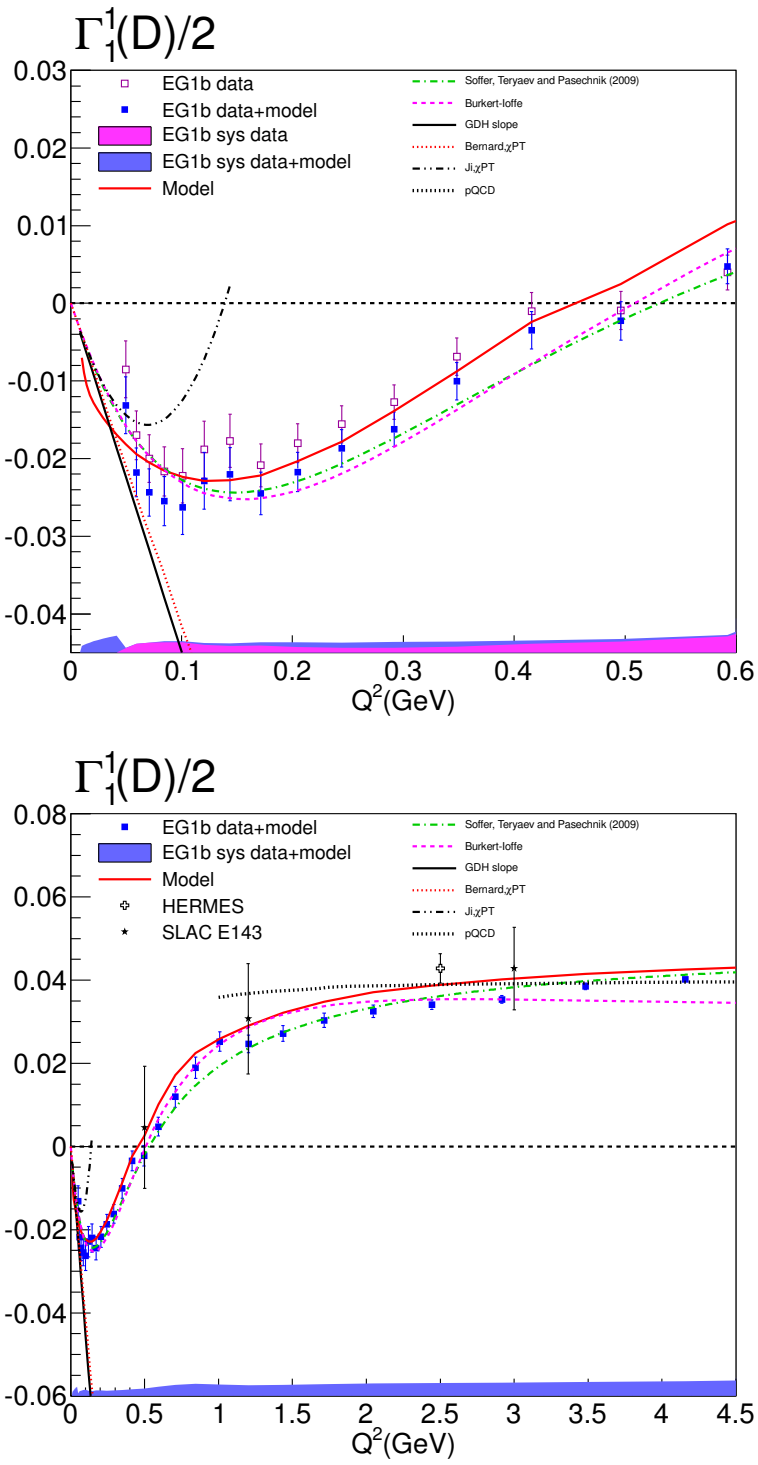

FIG. 29: The top plot is the same as Fig. 28 only zoomed into the low Q^2 region. Results from other experiments are also shown in the bottom plot, including E143 [46], HERMES [49].

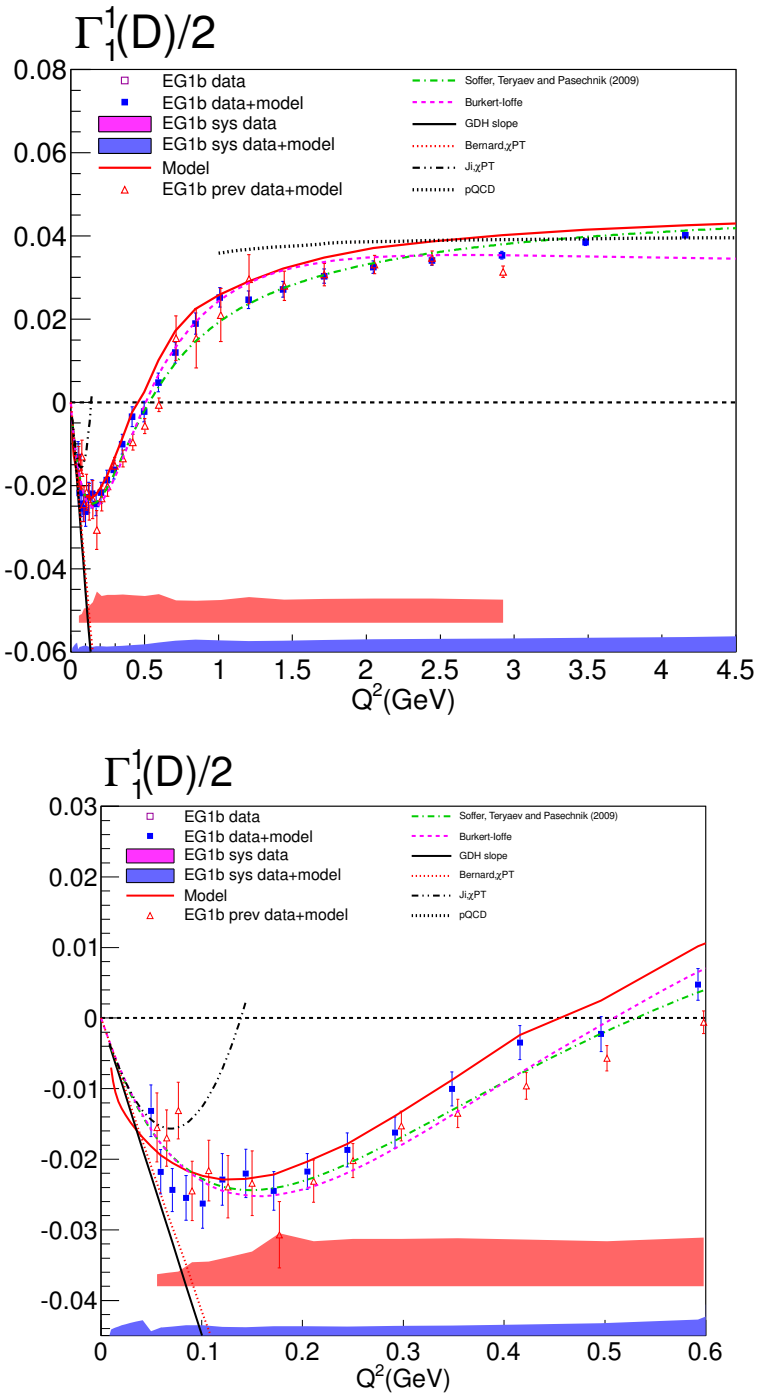

FIG. 30: Comparison of this analysis and the previous one on the Γ_1^1 extraction from EG1b. The red triangles represent the previous analysis, which was done by only using the 1.6 and 5.7 GeV data. For clear visibility, those points are shifted to a slightly higher Q^2 by adding an offset factor. The two independent analysis results complement each other well within statistical errors. Addition of the 2.5 and 4.2 GeV data clearly improves the medium Q^2 region and the overall statistics.

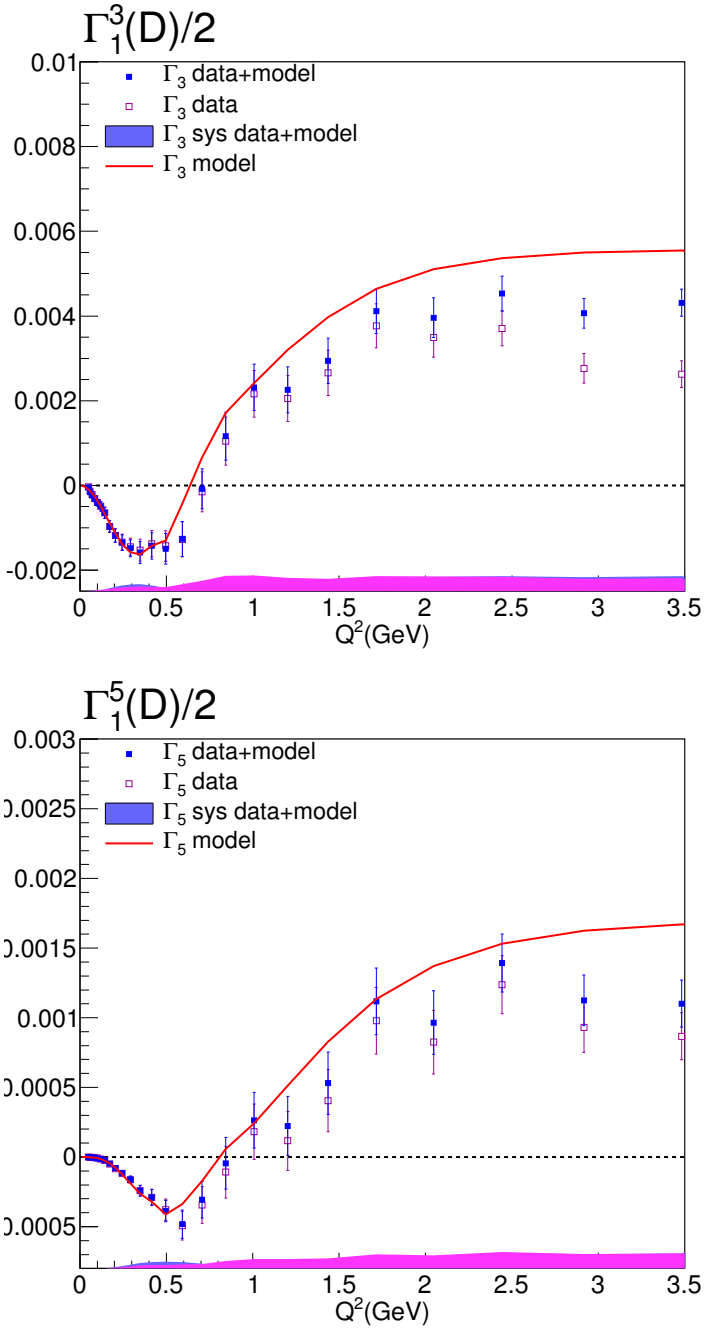

FIG. 31: Higher moments of g_1 extracted from the EG1b data are shown with respect to Q^2, the third moment Γ_1^3 (top), and the fifth moment Γ_1^5 (bottom). The hollow squares were calculated with no model contribution while the filled squares have model input for the kinematic regions with no available data.

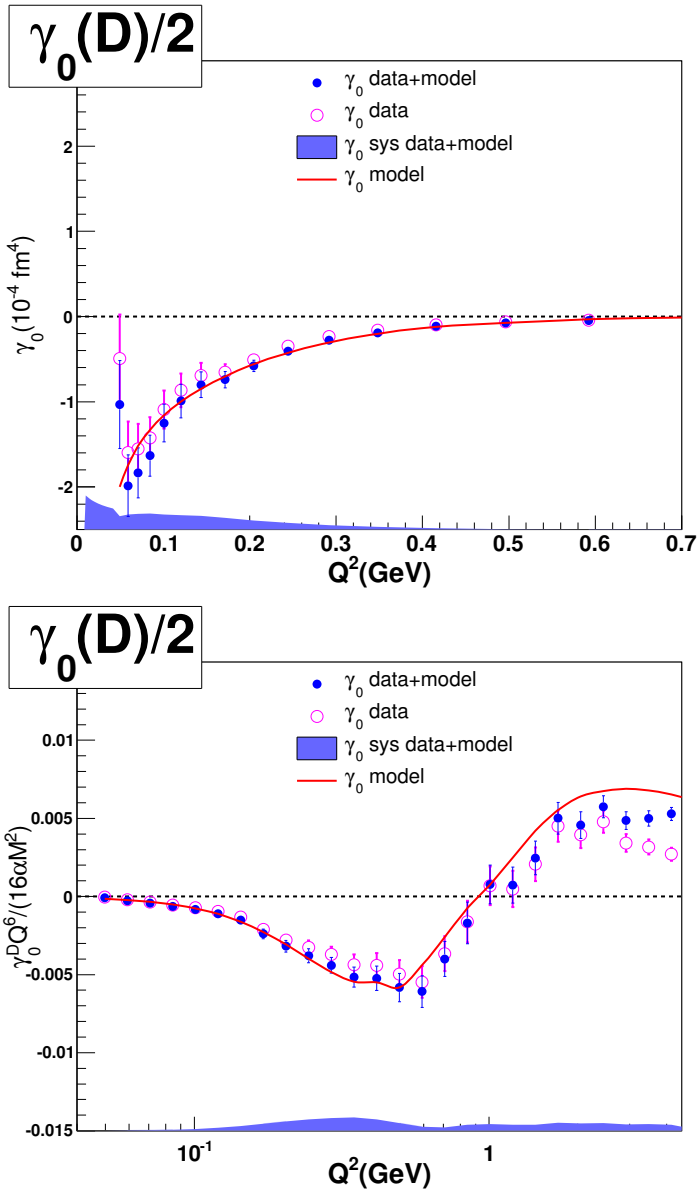

FIG. 32: Forward spin polarizability (γ_0) for the deuteron is shown versus Q^2. The hollow circles represent the calculation by using only data and the full circles are data + model results. The green shaded area is the total systematic error. The systematic error that comes from g_2, by taking $g_2 = 0$, is shown with the gray shade overlapped on the total systematic error. The model curve is also shown as a line through data points. The top plot shows values also multiplied by 15.134 for unit conversion to [10^{-4} fm^4]. The bottom plot is just the integral part, without the kinematic factor taken into account.

CHAPTER III

MODELING THE WORLD DATA

As new data are generated on the structure functions, our knowledge in different kinematic regions improves, which enables us to upgrade the models on interesting physics quantities such as A_1 and A_2 for the proton, the neutron and the deuteron. This chapter presents the latest efforts for fitting the world data to produce reliable models, specifically for A_1 and A_2 for the proton and neutron. Moreover, since data are rare on the neutron target, existing deuteron and proton data, especially with the help of the EG1b results, provide us a platform to extract information on the neutron spin structure functions.

The behavior of the spin structure functions and the asymmetries in the resonance region is especially interesting because we don't have a rigorous theory to describe this region. Therefore, parametrization of the existing data in the resonance region remains the only reliable option. These parameterizations are needed to extract other physics quantities, study radiative effects and even learn about the effects of nuclear medium on the structure of the nucleon.

The general procedure for the fits includes collection of the world data on the specific quantities and utilization of a least-square fitting routine to determine the optimal parameters that describe the data best by minimizing the χ^2 of the fit, which is defined by

$$\chi^2(Q^2, W) = \sum_n \frac{(A^{data}(Q^2, W) - A^{fit}(Q^2, W))^2}{(\sigma_{A^{data}}(Q^2, W))^2} \tag{110}$$

where the sum is taken over all data points. $A^{data}(Q^2, W)$ is the value of the data for the specific quantity, A_1 or A_2, and $A^{fit}(Q^2, W)$ is the output of the fit function at the kinematic point of the data. The $\sigma_{A^{data}}(Q^2, W)$ is generally taken as the statistical error of the data point, but for some experiments, statistical and systematic errors were added in quadrature.

Minimization of χ^2 was performed by using the MINUIT package from CERN [112], which provides various different minimization routines. The most widely used is MIGRAD, which is regarded as "the most efficient and complete single method, recommended for general functions" [112]. We tried MIGRAD as well as MINOS, to evaluate parameter errors. Also, the MINIMIZE scheme uses MIGRAD unless it

gets into trouble, in which case it switches to SIMPLEX, which is another multi-dimensional minimization routine, and then calls MIGRAD again. In the end, we decided to use the MINIMIZE routine. However, we did not observe, in any of the fits we used, a failure with MIGRAD and a switch to SIMPLEX.

Various parameterizations were tried and compared to each other. The final functional forms are given in the following sections. The parametrized functions, in general, also utilize other existing models such as MAID 2007 [131] as well as an older parameterization of the same kind performed on the more limited data set of the time. MAID is a unitary isobar model for pion photo- and electroproduction on the nucleon. It describes the world data on the $\gamma^* N \to \Delta$ transition and threshold π^0 production. These existing models provided us a method to extrapolate the fit successfully into the kinematic regions with no available data, which is the case specifically with A_2^p and A_2^n parameterizations..

In the following sections, information is given on the specific parameterizations of the existing world data on the virtual photon asymmetries A_1 and A_2 in the resonance region for the proton and the neutron. We should point out that all data shown in this chapter were averaged over $\Delta W = 40$ MeV for plotting purposes by taking their error weighted averages. However, fitting was performed on the individual data points at their true kinematic values. Once the models for the spin structure functions of the proton and the neutron were created, the deuteron models in the resonance region were obtained by smearing the nucleon structure functions and adding them. For this purpose, the smearing procedure developed in Ref. [74] was used.

III.1 PARAMETRIZATION OF A_1^p

The EG1b experiment measured A_1^p in the resonance region with an unprecedented precision. Therefore, the largest amount of data for this fit comes from the EG1b experiment, in the kinematic region 0.05 GeV^2 $< Q^2 <$ 5.0 GeV^2. The next experiment is from MIT BATES [132] and has precision data in the Δ resonance region for Q^2 = 0.123, 0.175, 0.240 and 0312 GeV^2. Then the RSS experiment [133][134], performed in Hall-C of the Jefferson Lab, provides precision data in the region 1.0 $< Q^2 <$ 1.4 GeV^2 and 1.08 GeV $< W <$ 2.0 GeV. We also used the results from the EG1a experiment [69], which measured A_1^p in the Q^2 region from 0.15 to 1.6 GeV^2.

The fit was performed in two separate steps. The first step employed a 16 parameter fit function. In this function, some of the parameters were used to specifically

treat certain W regions to describe the resonant structure better. Also, the MAID model and an extrapolation of the DIS model into the resonance region were utilized to ensure the resulting parametrization smoothly continues in the high and low W regions. The resulting parameters from this step were fixed and the function was used as a static quantity in the second step fit. The second step employed a 12 parameter fit function. In this step, we also used an older parametrization and made use of its strength in some kinematic regions. This two-step approach created a good method to treat and fine tune certain kinematic regions and describe the resonant structure better. The fit function for the first step can be written as:

$$
\begin{aligned}
E_1 &= P_0 + P_1 \tan^{-1}[\left(Q^2 - P_2^2\right) P_3^2] \\
E_2 &= P_4 + P_5 \tan^{-1}[\left(Q^2 - P_6^2\right) P_7^2] \\
E_3 &= 1 - E_1 - E_2 \\
E_4 &= P_8 + P_9 \tan^{-1}[\left(Q^2 - P_{10}^2\right) P_{11}^2] \\
E_5 &= P_{12} + P_{13} \tan^{-1}[\left(Q^2 - P_{14}^2\right) P_{15}^2] \\
C_1 &= 1 - \sin\left(\frac{\pi}{2}\left[\frac{W - 1.08}{2 - 1.08}\right]\right) \\
C_2 &= C_1^2 \\
C_3 &= \cos\left(\frac{\pi}{2}\left[\frac{W - 1.08}{2 - 1.08}\right]\right) \\
C_4 &= \begin{cases} \left[\sin\left(\pi\left[\frac{W-1.08}{1.9-1.08}\right]\right)\right]^2 & W \geq 1.9 \\ 0 & W < 1.9 \end{cases} \\
C_5 &= \begin{cases} \sin\left(\pi\left[\frac{W-1.08}{1.35-1.08}\right]\right) & W < 1.35 \\ 0 & W \geq 1.35 \end{cases} \\
\mathcal{M} &= E_1 C_1 + E_2 C_2 + E_3 C_3 + E_4 C_4 + E_5 C5 \\
A_1^{C[1]} &= \begin{cases} \mathcal{M} A_1^M + (1 - \mathcal{M}) A_1^{DIS} & W \leq 2 \\ A_1^{DIS} & W > 2 \end{cases}
\end{aligned}
\tag{111}
$$

where P_i represents parameter i, A_1^M is the MAID 2007 model of A_1^p and A_1^{DIS} is the DIS extrapolation. $A_1^{C[1]}$ represents the calculated fit from the first step. The parametrization for $A_1^{C[1]}$ is used in the second step fit function, which is described by

$$
\begin{aligned}
Q_{ph}^2 &= \begin{cases} 0 & Q^2 \leq 0.01 \text{ GeV}^2 \\ \frac{1}{3\pi}\left(\frac{\log\left(Q^2\right)}{\log(10)} + 2\right) & Q^2 > 0.01 \text{ GeV}^2 \\ 1 & Q^2 > 10 \text{ GeV}^2 \end{cases} \\
W_{ph} &= \pi \frac{(W - 1.08)}{(2.04 - 1.08)} \\
D_0 &= P_0 + P_1 \cos\left(Q_{ph}^2\right) + P_2 \cos\left(2Q_{ph}^2\right) \\
D_1 &= P_3 + P_4 \cos\left(Q_{ph}^2\right) + P_5 \cos\left(2Q_{ph}^2\right) \\
D_2 &= P_6 + P_7 \cos\left(Q_{ph}^2\right) + P_8 \cos\left(2Q_{ph}^2\right) \\
D_3 &= P_9 + P_{10} \cos\left(Q_{ph}^2\right) + P_{11} \cos\left(2Q_{ph}^2\right) \\
\mathcal{B} &= \begin{cases} D_0 \sin\left(12W_{ph}\right) + D_1 \sin\left(W_{ph}\right) & \\ \quad + D_2 \sin\left(2W_{ph}\right) + D_3 \sin\left(4W_{ph}\right) & W < 2.04 \text{ GeV} \\ 0 & W \leq 2.04 \text{ GeV} \end{cases} \\
A_1^C &= \left(1 - \mathcal{B}\right) A_1^{C[1]} + \mathcal{B} A_1^{OM}
\end{aligned}
\tag{112}
$$

where A_1^{OM} represents an older parametrization and A_1^C is the updated parametrized model. The total number of parameters for the whole fit is 28. During each fit step, the minimization was performed iteratively, generally two iterations were used, automatically passing the results of the first iteration as the starting parameters of the second one. In the first iteration, an initial step size of 0.00001 was used on all parameters. After the first evaluation of the χ^2, MINUIT decides on the step size values based on the first derivatives. In the second iteration, we let MINUIT continue to decide the step sizes internally. We observed that the final step sizes are generally very close to zero, on the order of 10^{-10}. Also, no restrictions were employed on the parameter limits.

Tables 22 and 23 give the initial and final values of the parameters together with estimated errors and the first derivatives. No user defined derivatives were supplied, in which case, MINUIT uses its own method by evaluating the finite differences over the step size. The small step sizes we observe ensures the reliability of these first derivatives, which in turn yields the reliability of the parameter errors. The resulting first derivatives are generally small or practically zero for some of the parameters. However, the parameter errors were not used to determine the systematic errors

on the actual model. The errors on the model were determined systematically by evaluating the differences between the new fit and various different parameterizations from old fits.

Total number of data points for the A_1^p fit was 4325. For the step 1 fit with 16 parameters, the initial χ^2 value was 22898. After the fit, a χ^2 of 5231.94 was reached. For the second step with 12 parameters, the initial χ^2 was 5331.92 and the final value became 4500.08, which results $\chi^2/n.d.f \approx 1.04$. Figs. 33 and 34 show the resulting fit together with the data and the other models for various Q^2 regions.

TABLE 22: Parameters for the first step A_1^p fit (version number 20S1 [135]). The fit function is given in Eq. (111). The total number of data points used in the fit was 4325. The final $\chi^2/n.d.f \approx 1.209$ was reached at the end of the fit.

ParNo	Initial	Final	Error	First Derivatives
1	0.4	-1.01616e−01	8.42531e−01	2.01952e−03
2	0.1	-2.97618e+00	7.93359e−01	2.89470e−03
3	0.5	-3.23456e−01	2.68590e−02	-7.30760e−03
4	1.0	2.74645e+00	4.96660e−01	-2.24628e−03
5	0.4	1.21003e+00	8.04876e−01	2.13005e−03
6	0.1	3.10913e+00	7.00746e−01	2.83534e−03
7	0.5	4.56491e−05	3.39639e−04	4.65342e−03
8	1.0	2.17872e+00	4.27999e−01	2.32311e−03
9	0.1	5.08220e−01	8.64463e−01	-6.65403e−03
10	0.1	-5.99465e−01	5.56410e−01	1.04521e−02
11	0.5	-1.09332e+01	5.46744e+01	-6.88992e−14
12	1.0	-2.03878e+03	1.44157e+04	-1.98474e−12
13	1.0	3.42967e−01	8.05711e−02	1.32518e−02
14	0.1	4.38685e−01	1.43131e−01	5.90950e−03
15	1.0	1.28403e−07	1.17306e+00	1.07202e−06
16	1.0	1.01192e+00	4.94477e−01	2.97119e−03

III.2 PARAMETRIZATION OF A_2^p

A similar method as described in the previous section was used to fit the A_2^p data. Again, there were no restrictions on the parameter limits and the same initial step sizes with two consecutive iterations were employed for MINUIT.

Data on A_2^p is sparse, which makes the fit difficult. Mainly, the RSS [136], BATES [132] and the latest EG1b [96] results were used for this fit. The EG1b results were obtained by linear regression between $A_1 + \eta A_2$ values and η from varying beam

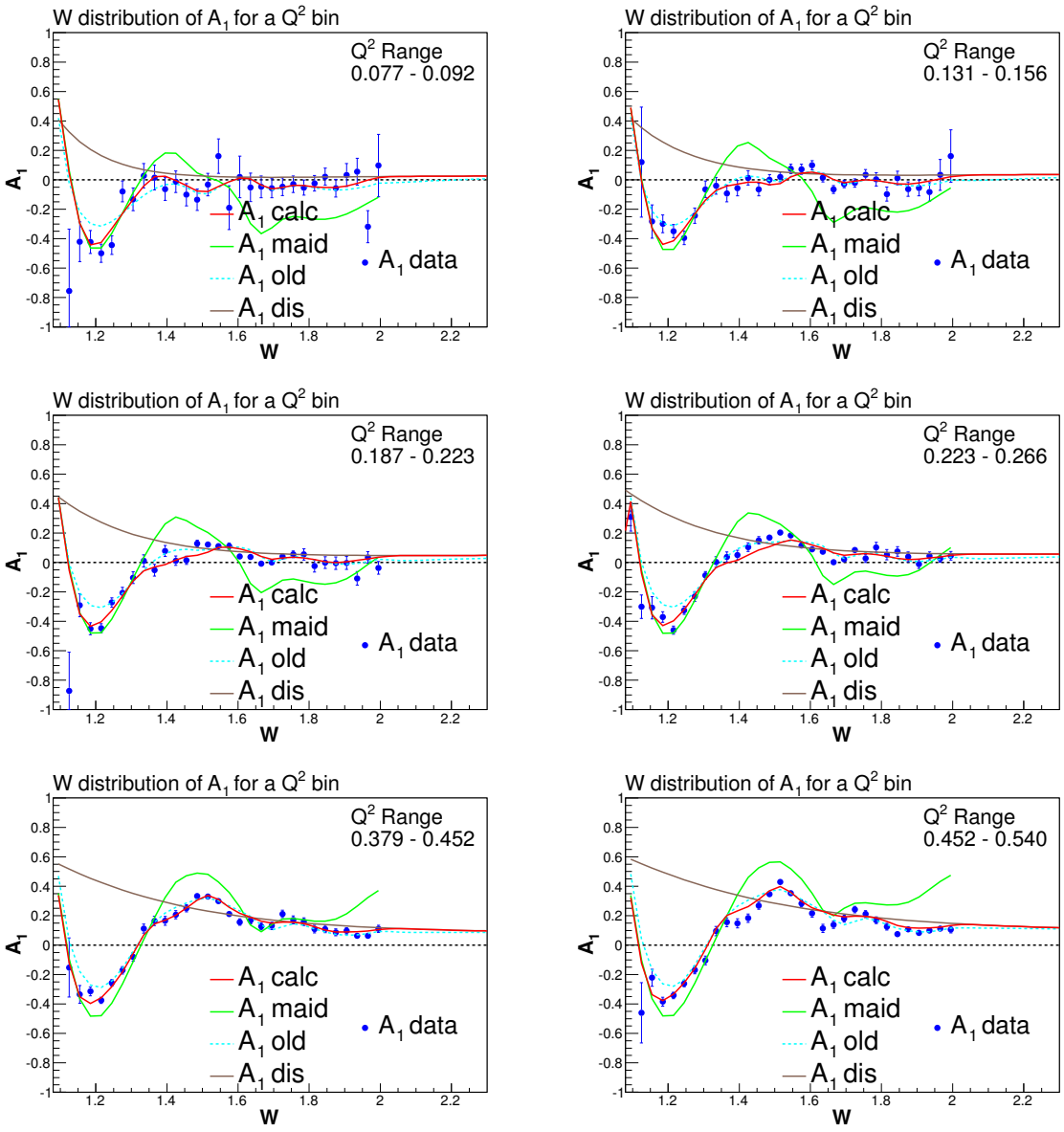

FIG. 33: A_1^p parametrization for various Q^2 bins. The fit is shown with the red curve. Other curves are MAID 2007, old parametrization and the DIS extrapolation into the resonance region. For only plotting purposes, the data from different contributing experiments were combined over $\Delta W = 40$ MeV, by taking their error weighted averages (fitting was performed on the individual data points at their true kinematic values).

TABLE 23: Parameters for the second step A_1^p fit (version number 20S2 [135]). The fit function is given in Eq. (112). The total number of data points used in the fit was 4325. The final $\chi^2/n.d.f \approx 1.0405$ was reached at the end of this fit.

ParNo	Initial	Final	Error	First Derivatives
1	0.0	2.19052e-01	4.25711e-02	-1.92465e-02
2	0.0	1.42339e-01	5.77638e-02	-1.23507e-02
3	0.0	-1.19772e-01	5.96739e-02	-8.45372e-03
4	0.0	4.27655e-01	4.96346e-02	-4.19115e-02
5	0.0	1.79650e-01	3.12603e-02	-2.84653e-01
6	0.0	3.32088e-03	6.51726e-02	6.57517e-02
7	0.0	-7.13901e-02	5.61801e-02	8.36566e-03
8	0.0	-2.57325e-01	6.96612e-02	5.24777e-03
9	0.0	2.53712e-01	7.17325e-02	1.21548e-02
10	0.0	-1.57327e-01	3.74878e-02	-1.06141e-02
11	0.0	1.53637e-01	5.66157e-02	-3.72469e-03
12	0.0	-2.91941e-01	5.66538e-02	-1.40743e-02

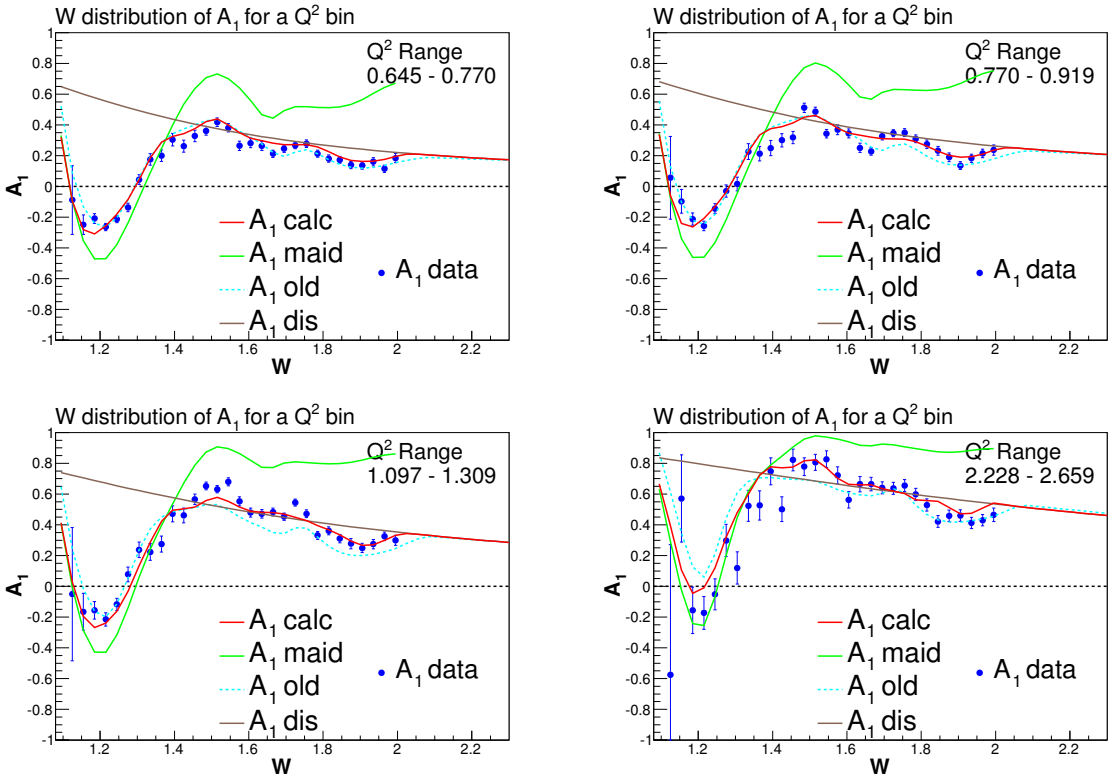

FIG. 34: A_1^p parametrization for various Q^2 bins (continuation of Fig. 33).

energies. After various trials with different fit functions, the following form was employed:

$$
\begin{aligned}
E_3 &= P_0^2\left(\frac{\pi}{2} - \tan^{-1}\left(Q^2P_1^2 + P_2\right)\right)\\
E_2 &= \frac{P_3^2 + \tan^{-1}\left(Q^2P_4^2 + P_5\right)}{\frac{\pi}{2} + P_3^2}\\
E_1 &= 1 - E_2 - E_3\\
E_4 &= \frac{P_6^2}{\left(\log\left(Q^2\right) - P_7\right)^2 + P_8^2 + 0.0001}\\
C_1 &= 1 - \left[\frac{W - 1.08}{2 - 1.08}\right]\\
C_2 &= \left[1 - \sin\left(\frac{\pi}{2}\left[\frac{W - 1.08}{2 - 1.08}\right]\right)\right]^2\\
C_3 &= \cos\left(\frac{\pi}{2}\left[\frac{W - 1.08}{2 - 1.08}\right]\right)\\
C_4 &= \begin{cases} \sin\left(\pi\left[\frac{W-1.3}{1.8-1.3}\right]\right) & 1.3 \le W \le 1.8\\ 0 & \text{otherwise}\end{cases}\\
\mathcal{M} &= E_1C_1 + E_2C_2 + E_3C_3\\
A_2^C &= \begin{cases} \mathcal{M}A_2^M + \left(1 - \mathcal{M}\right)A_2^{DIS} + E_4C_4 & W \le 2\\ A_2^{DIS} & W > 2\end{cases}
\end{aligned}
\tag{113}
$$

Similar to the previous section, P_i represents parameter i and A_2^C represents the calculated fit, while A_2^M is the MAID model and A_2^{DIS} is the DIS extrapolation. The Wandzura-Wilczek relation and the Burkhardt-Cottingham Sum Rule [8] were used to estimate the DIS extrapolation of A_2 into the resonance region and were used as a constraint in the fit. A smooth transition between the resonance region and the DIS region was required. In addition, another constraint, the Soffer limit provided a general estimate and a boundary on the fit results. A penalty was applied to the χ^2 for cases when the calculated fit exceeded the Soffer limit such that:

$$
\chi^2(Q^2, W) = \sum_n \frac{\left(|A^{fit}(Q^2, W)| - A^{soffer}(Q^2, W)\right)^2}{0.005}. \tag{114}
$$

The fit was performed in several iterations. In the first iteration, the values of parameters P_6, P_7 and P_8 were kept constant, and in the second iteration, they were

released. The resulting parameters from these first calculations were used as the starting parameters for the next round and the same fit was repeated twice, again first fixing parameters P_6, P_7, P_8 and releasing them after the first 6 parameters reached their optimal values.

The total number of data points for the A_2^p fit was 344. The final χ^2 of the fit was 418.8, resulting in a $\chi^2/n.d.f \approx 1.21$. Table 24 shows the resulting parameter values and Fig. 35 shows the fit results together with the available data for various Q^2 regions.

TABLE 24: Parameters for the A_2^p fit given in Eq. (113). The final $\chi^2/n.d.f \approx 1.21$ was reached at the end of this fit. The total number of data points used in the fit was 344.

ParNo	Final	Error	First Derivatives
1	5.92348e−01	1.97150e−01	9.30561e−04
2	1.66989e+02	4.89463e−01	-2.21883e−04
3	-2.79601e+04	1.62278e+02	-2.99000e−07
4	-1.80099e+00	4.56000e−01	2.26247e−04
5	3.66274e+00	7.98533e+02	5.63709e−10
6	-7.76211e+04	4.47812e+06	3.92323e−15
7	2.72528e−01	5.91656e−02	1.13762e−02
8	-1.77948e−01	9.76423e−02	4.03108e−03
9	4.72596e−01	1.06130e−01	-2.63065e−03

III.3 PARAMETRIZATION OF A_2^n

It is not possible to make a direct measurement on a polarized neutron target to extract the asymmetries and structure functions of the neutron. The best approximates to a polarized neutron target are polarized ^{3}He and deuterium targets. In both cases, the nuclear effects smear the nucleon structure, making it difficult to isolate the information from a single nucleon. Currently, there are limited data on a transversely polarized deuteron target [133]. However, smearing makes it difficult to extract neutron information for A_2^n from deuteron because proton dominates. In the resonance region, there are also two other experiments that took measurements on a polarized ^{3}He target. The first experiment was E94-107, which took place in Hall-A at Jefferson Lab [137][138]. The experiment measured the spin-dependent cross section for the inclusive scattering of polarized electrons from a polarized ^{3}He

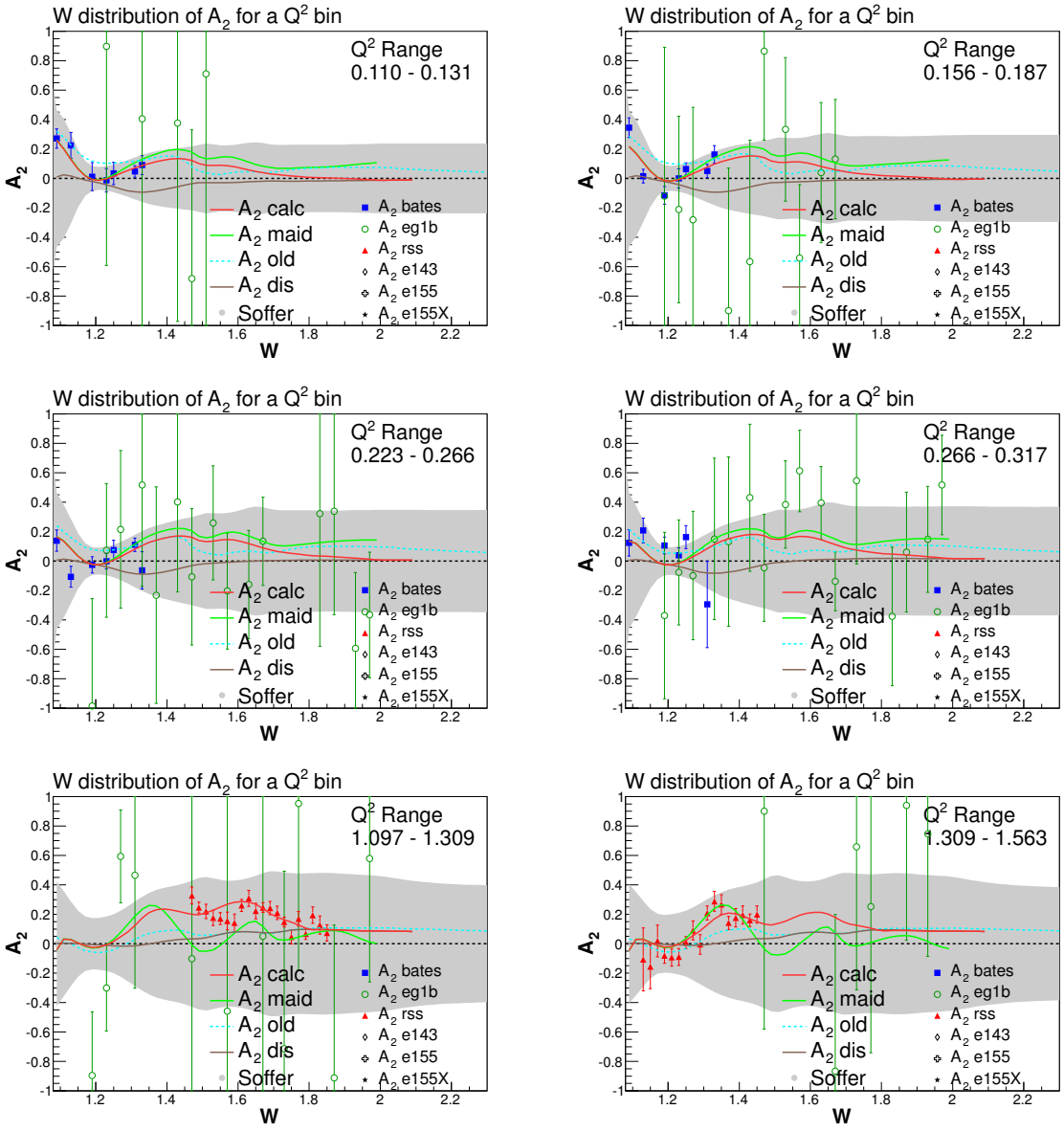

FIG. 35: A_2^p parametrization (red line) for various Q^2 bins, for which there are available data, are shown together with other models described in the text. The shaded area represents the Soffer limit. The RSS (red), BATES (blue) and EG1b (green circle) data are also plotted.

target in the quasi-elastic and resonance regions for $0.1 < Q^2 < 0.9$ GeV^2. By using both the transverse and longitudinally polarized targets, the experiment extracted the spin structure functions g_1 and g_2 for ^{3}He. The second experiment, E01-012, also took place in Hall-A at Jefferson Lab to measure the quark-hadron duality on the neutron by using a polarized ^{3}He target [139][140]. This experiment also extracted the spin structure functions g_1 and g_2 for ^{3}He by measuring the cross section for inclusive electron scattering off longitudinally and transversely polarized targets.

Since we are merely trying to model the general behavior of A_2^n in the resonance region, we decided to use these data on ^{3}He to extract some A_2^n data for our fits. We first applied simple nuclear corrections to get the polarized structure function of the neutron from the ^{3}He data by using our latest model for the proton,

$$g_1^n = \frac{g_1^{\mathrm{He}} + 2.0 \times 0.027 g_1^{p[m]}}{0.87} \tag{115}$$

$$\sigma_{g_1^n} = \frac{\sigma_{g_1^{\mathrm{He}}}}{0.87} \tag{116}$$

$$g_2^n = \frac{g_2^{\mathrm{He}} + 2.0 \times 0.027 g_2^{p[m]}}{0.87} \tag{117}$$

$$\sigma_{g_2^n} = \frac{\sigma_{g_2^{\mathrm{He}}}}{0.87} \tag{118}$$

where the factor 0.87 is for the effective neutron polarization in ^{3}He while 0.027 is that of the proton, with two protons. Then we calculated the corresponding virtual photon asymmetries A_1 and A_2 for the neutron by using these results,

$$A_1 = \frac{g_1 - \gamma^2 g_2}{F_1} \tag{119}$$

$$\sigma_{A_1}^2 = \left(\frac{\sigma_{g_1} - \gamma^2 \sigma_{g_2}}{F_1} \right)^2 \tag{120}$$

$$A_2 = \frac{\gamma}{F_1}(g_1 + g_2) \tag{121}$$

$$\sigma_{A_2}^2 = \left(\frac{\gamma}{F_1}(\sigma_{g_1} + \sigma_{g_2}) \right)^2 \tag{122}$$

where we used the existing models for F_1, which are described in section I.7. Once we have the relevant data, we utilized our fit function given in (113), which was also used to fit the proton data on A_2^p. The total number of data points we had for this case was 161. The initial χ^2 of the fit with the starting parameters was 350.55 while the final χ^2 after the minimization was 190.23, yielding $\chi^2/n.d.f = 1.18$. Table 25 shows the initial and the final parameters of the A_2^n fit. Figs. 36 and 37 show the fit together with the experimental data for various Q^2 values with available data.

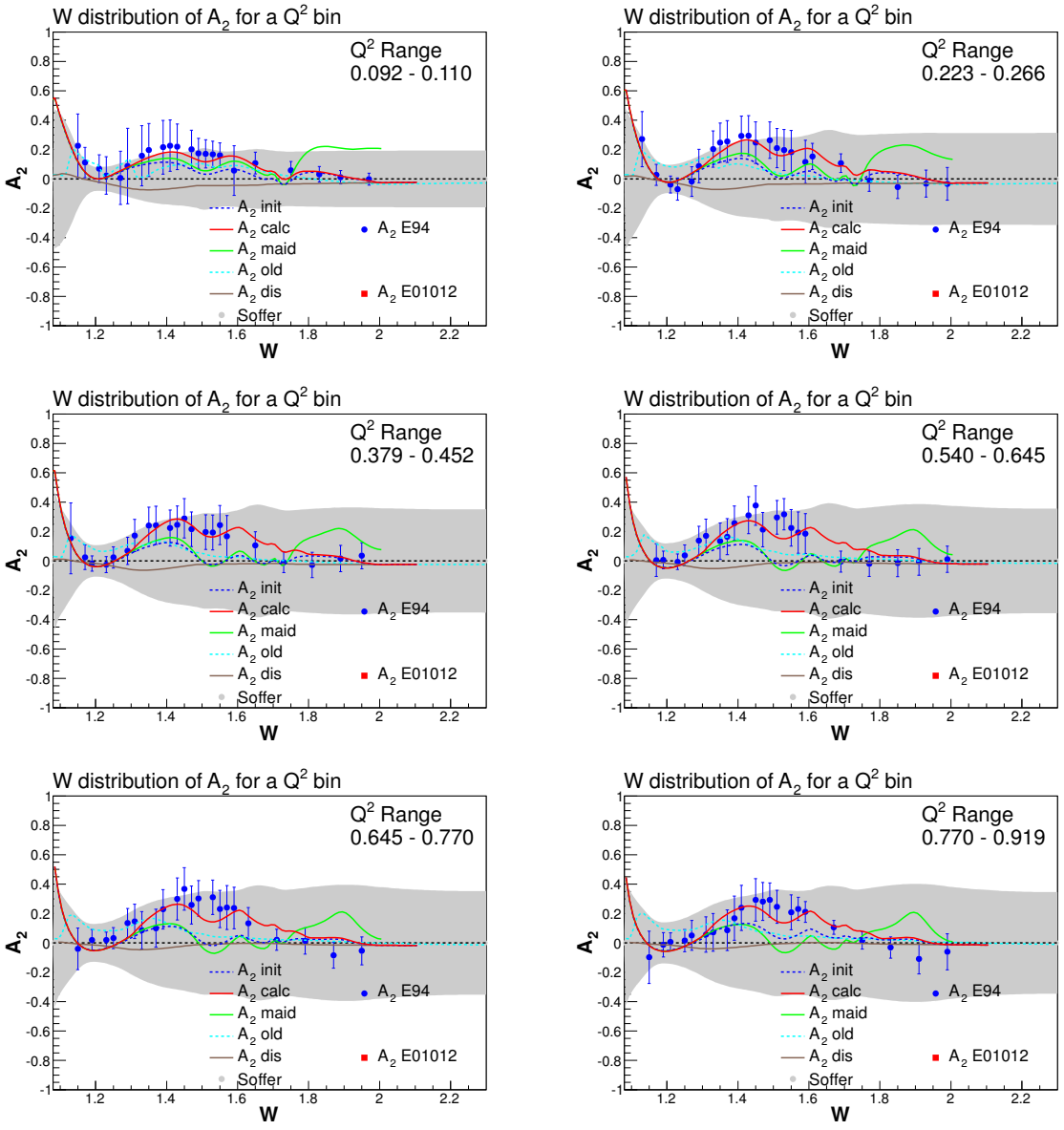

FIG. 36: A_2^n parametrization for various Q^2 bins with available data. The red line represents the fit. Blue data points are from the E94-107 experiment. The MAID model (green), the DIS extrapolation (brown) and older parametrization (cyan) are also plotted. The shaded region is the Soffer limit.

TABLE 25: Parameters for the A_2^n fit given in Eq. 113. The final $\chi^2/n.d.f \approx 1.18$ was reached at the end of this fit. The total number of data points used in the fit was 161.

ParNo	Initial	Final	Error	First Derivatives
1	0.7	-4.56143e−08	5.79134e+00	-2.72043e−09
2	1.0	-3.56573e+00	1.41421e+00	0.00000e+00
3	-2.0	6.91149e+01	1.41421e+00	0.00000e+00
4	1.0	4.64862e−01	9.00620e−02	8.86916e−05
5	1.0	-1.64811e+01	3.09743e−02	2.48725e−03
6	-1.0	-8.14488e+02	3.06294e+00	-1.08100e−05
7	0.07	6.24803e−01	2.07558e−02	-1.21569e−03
8	0.0	-5.58762e−01	1.21758e−01	9.07721e−05
9	0.2	1.36991e+00	5.60160e−02	2.78096e−04

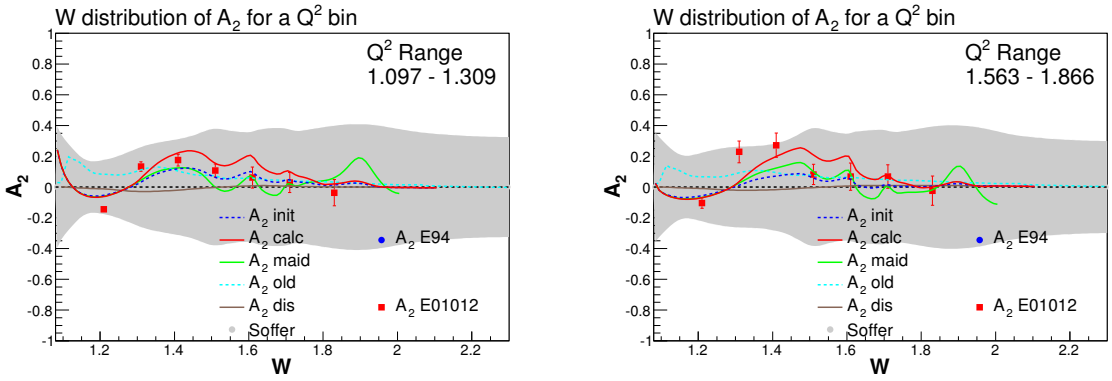

FIG. 37: A_2^n parametrization for various Q^2 bins with available data. The red line represents the fit. The data from E01-012 is also shown (red) together with the MAID model (green), the DIS extrapolation (brown) and an older parametrization (cyan). The shaded region is the Soffer limit.

III.4 PARAMETRIZATION OF A_1^n BY USING THE DEUTERON DATA

The main ingredients for a fit of A_1 for the neutron are the data on the deuteron spin structure function g_1 and the convolution procedure described in Refs. [74][141] and appendix D. Extraction of the neutron information requires a careful study of the nuclear effects, especially the Fermi motion, which is primarily considered in the convolution procedure. Of course, the D-wave correction was also applied. Moreover,

using the best possible fits to the protondata is essential for the best results with this method. Since the EG1b experiment took data on both of these targets, we have a unique opportunity to extract the neutron asymmetries and structure functions by using the results from EG1b.

The fitting mechanism for this case is quite different than in the previous cases. The fitted data come from the ratio of deuteron structure functions g_1/F_1 extracted from measurements of $A_{||}$. The results of the EG1b experiment, described in this thesis, were used as well as the measurements from the RSS [133] and E143 [46] experiments. A fit function was employed to parametrize A_1^n and the parametrized A_1^n was used in the smearing procedure, together with the A_1^p parametrization described in section III.1. The smearing function combines the information for the proton and neutron by taking nuclear effects like Fermi motion into account and calculates the deuteron structure functions g_1^d and F_1^d. The ratio of these two was compared to data to calculate the χ^2 of the fit according to Eq. (110). After the minimization of the χ^2, the resulting parameters were used in the fit function for the neutron to determine the parametrized values of A_1^n.

For the fit function, the parameterizations of A_1^p and A_2^p, described in Eqs. (111) and (113), were both tried. Eventually, the A_2^p parametrization in Eq. (113), which was also used for A_2^n, seemed to described the data best. The total number of data points for this fit was 3175. The final χ^2 was 2503.41 which yields $\chi^2/n.d.f \approx 1.26$ The current results describe the data well in most kinematics as can be seen in Fig. 38. The model for A_1^n obtained by using the final parameters is also shown in Fig. 39.

Finally, once we have reliable models for the proton and neutron structure functions, we can calculate the model g_1 for the deuteron by properly smearing the proton and neutron. As a result, we have both experimental data on the deuteron spin structure function g_1 as well as its model. We can then extract an *experimental* value for the neutron structure function g_1^n from this input using the following Equation:

$$g_1^{n[data]} = \frac{1}{1 - 1.5w_D}(g_1^{d[data]} - g_1^{d[model]}) + g_1^{n[model]} \tag{123}$$

where w_D stands for D-state probability. This assumes that any difference between the measured and model values of g_1^d is due to a difference δg_1^n between the "true" value for g_1^n and our model, since the corresponding model for g_1^p (that also enters g_1^d) is constrained with much higher precision from the free proton data. Hence,

$g_1^{n[data]} = g_1^{n[model]} + \delta g_1^n$. In principle, one would have to "unswear" this deviation δg_1^n before adding it to the model g_1^n to get the data-driven value; however, due to our fit method, this deviation is already very small and therefore it is sufficient to correct only for the reduced polarization inside deuterium (the D-state effect).

The statistical and systematic errors propagate as

$$\sigma^{stat}_{n[data]} = \frac{1}{1 - 1.5 w_D}\, \sigma^{stat}_{d[data]} \tag{124}$$

$$\sigma^{sys}_{n[data]} = \frac{1}{1 - 1.5 w_D}\, \sigma^{sys}_{d[data]}. \tag{125}$$

However, since this extraction depends on the model choice, we need to vary both the neutron and proton models and add the differences coming from model choices to the total systematic error in quadrature

$$\sigma^{systot}_{n[data]} = \left[(\sigma^{sys}_{n[data]})^2 + \left(\sum_i [g_1^{n[data]} - g_1^{n[i]}] \right)^2 \right]^{1/2}. \tag{126}$$

where summation is over different model choices and $g_1^{n[i]}$ represents the extracted result for model choice i. The results for this extraction are shown in Fig. 40 for a few Q^2 bins.

III.5 ADDITIONAL COMMENTS

The work on modeling the world data is a continuous and iterative procedure. Some of the results have certain model dependencies. For example, the EG1b results for A_1 have a slight dependence on the A_2 models (see Ref. [96]). By getting a better parametrization for A_2, the A_1 model can be improved and in turn, the A_2 parametrization can be re-visited to create a better model on this quantity. In addition, the data on these quantities are constantly improving in different kinematic ranges. The efforts will continue as these new data come into existence. In particular, the EG4 experiment [142] will allow us to extend our parameterizations of A_1^p, A_1^n into the lower Q^2 range and give us opportunity to resume our efforts. Similarly, new results from EG1-DVCS will be incorporated into improving our fits.

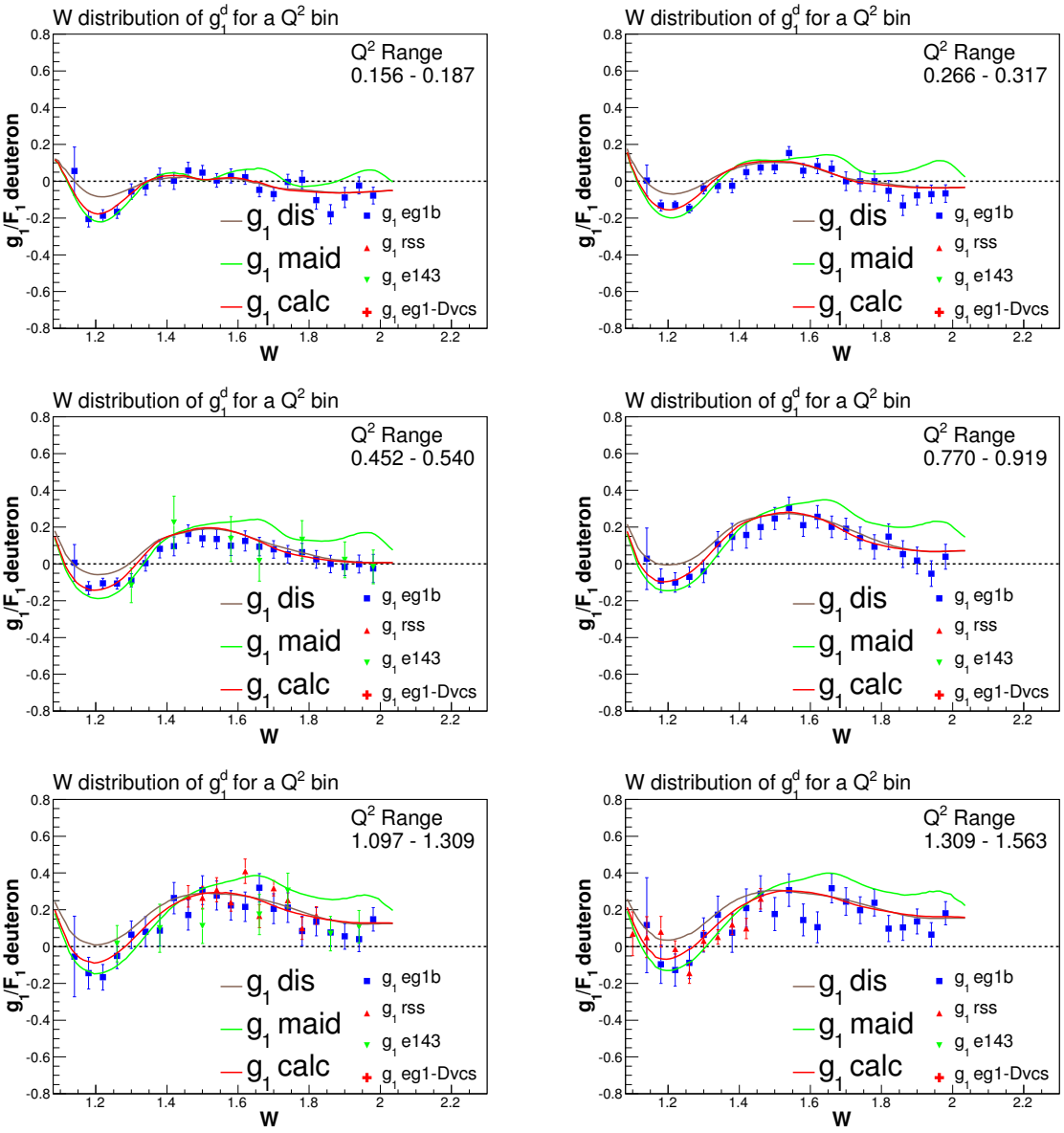

FIG. 38: The model for g_1/F_1 for the deuteron (red solid line), which was calculated from the parametrized A_1^n and A_1^p by applying the smearing procedure, is plotted together with the experimental data points for various Q^2 bins. Together with the EG1b experiment (blue), the RSS (red) and E143 (green) data are also shown. As usual, the green line represents MAID and the brown line is the DIS extrapolation.

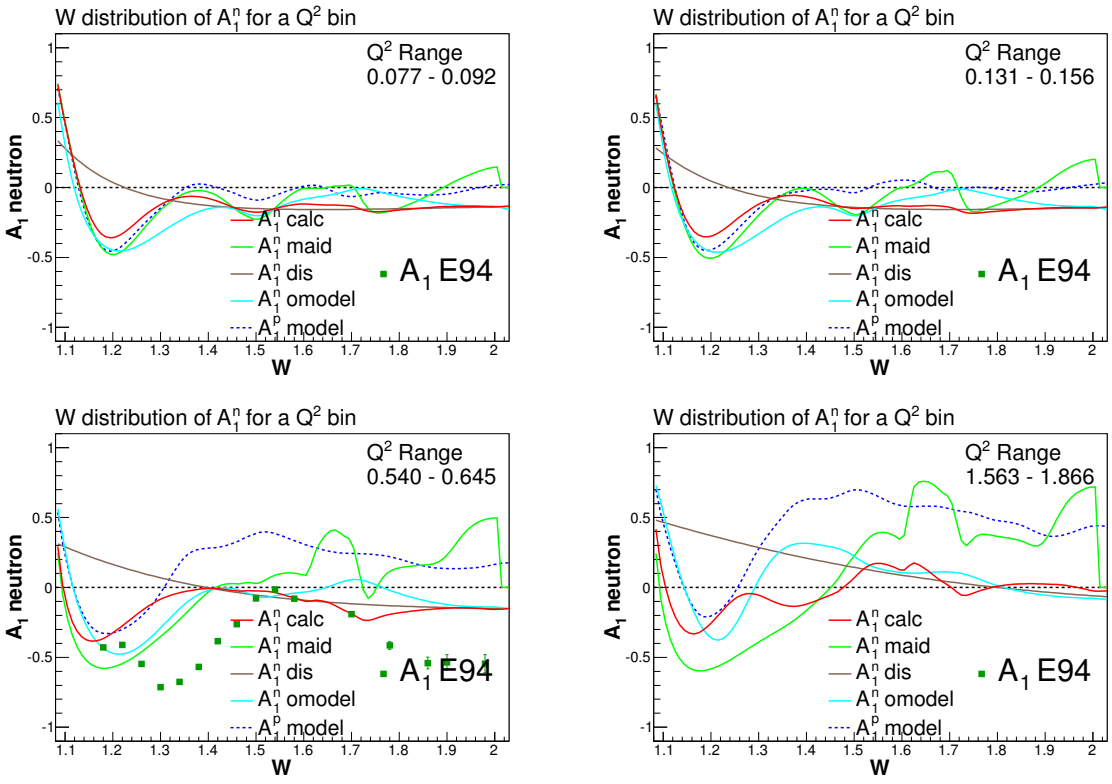

FIG. 39: The parametrized A_1 for the neutron (red curve) is shown for a few Q^2 bins. Also shown are the MAID curve (green) and the model of A_1 proton, for comparison purposes.

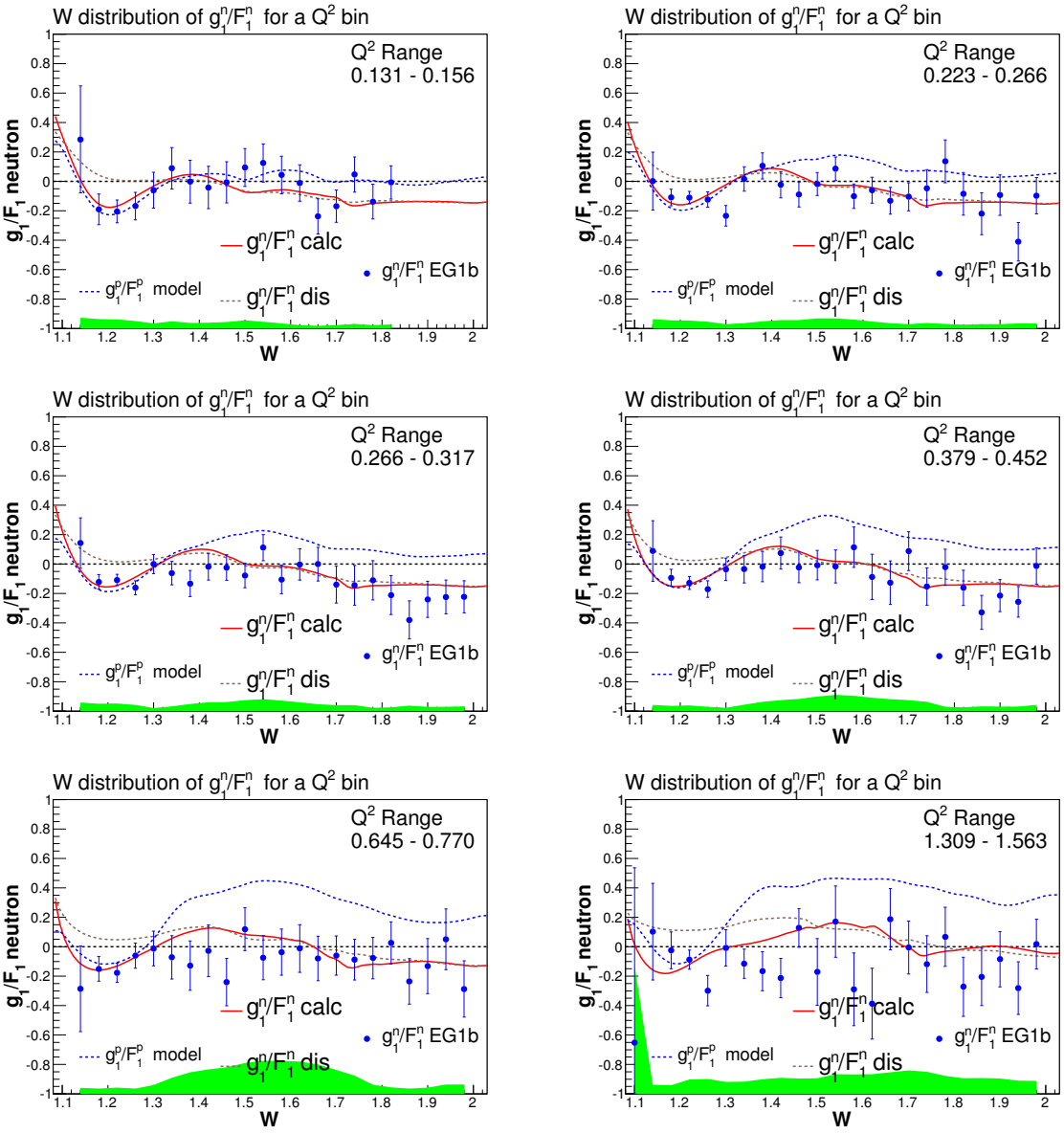

FIG. 40: Parametrized g_1/F_1 (red dashed line) for the neutron is plotted together with g_1/F_1 neutron (blue data points) extracted from the EG1b deuteron data according to Eq. (123). The systematic errors are shown as green shades at the bottom of each plot. The same quantity for proton is also shown for comparison purposes (blue dashed line).

APPENDIX A

DST VARIABLES

In the DST tables, the range (R) of a variable is defined in terms of the offset (o), the multiplier (m), the sign (s), that determines whether the variable is signed (1) or not (0), and the number of bits (n) for the variable,

$$R = \left[-\left(\frac{2^n}{m} - o \right) * s \; ; \; \left(\frac{2^n}{m} - o \right) \right]. \tag{127}$$

This is the scheme used in the DST libraries to determine the maximum and minimum acceptable values for the variables.

TABLE 26: DST variables: particle ID. SEB is the standard particle ID used in RECSIS, whereas p_id(DST) is the DST equivalent.

SEB ID	p_id(DST)	particle
11	1	electron
2212	2	proton
2112	3	neutron
211	4	π^+
-211	5	π^-
321	6	K^+
-321	7	K^-
45	8	deuteron
49	9	^3He
47	10	^4He
22	11	photon
-11	12	positron

TABLE 27: DST event headers

name	offset	multiplier	signed	bits	definition
event	0.0	1.0	0	27	event number from BOS file
n_part	0.0	1.0	0	5	number of particles in the event
start_time	0.0	100.0	1	14	event start_time
raster_x	0.0	1.0	0	16	x coordinate of the raster position
raster_y	0.0	1.0	0	16	y coordinate of the raster position
trigbits	0.0	1.0	0	16	trigger bit

TABLE 28: DST scaler variables and run information

name	offset	multiplier	signed	bits	definition
CLOCK_UG	0.0	1.0	0	31	live time ungated clock
CLOCK_G	0.0	1.0	0	31	live time gated clock
FC_UG	0.0	1.0	0	31	live time ungated faraday cup
FC_G	0.0	1.0	0	31	live time gated faraday cup
EVMin	0.0	1.0	0	27	first event of the helicity state
EVmax	0.0	1.0	0	27	last event of the helicity state
clockug	0.0	1.0	0	19	ungated clock
clockg	0.0	1.0	0	19	gated clock
fcupug	0.0	1.0	0	12	ungated faraday cup
fcupg	0.0	1.0	0	12	gated faraday cup
synchug	0.0	1.0	0	16	ungated SLM
synchg	0.0	1.0	0	16	gated SLM
PMTTop	0.0	1.0	0	10	PMT output
PMTBottom	0.0	1.0	0	10	PMT output
PMTBeamRight	0.0	1.0	0	10	PMT output
PMTBeamLeft	0.0	1.0	0	10	PMT output
BeamE	0.0	1.0	0	16	Beam energy
BeamI	0.0	10.0	0	10	Beam current
TorusI	0.0	1.0	1	12	Torus current
TargetI	0.0	1.0	1	12	Target current
BeamPol	0.0	100.0	1	7	Beam polarization
TargetPol	0.0	100.0	1	7	Target polarization
BadRun	0.0	1.0	0	32	Run flag
Target	0.0	1.0	0	7	Target type
PolPlate	0.0	1.0	0	2	Half-wave plate status

TABLE 29: DST particle variables

name	offset	multiplier	signed	bits	definition
p_id	0.0	1.0	0	4	particle identifier
p_x	0.0	10000.0	1	16	momentum
p_y	0.0	10000.0	1	16	momentum
p_z	0.0	10000.0	1	17	momentum
v_x	0.0	10.0	1	9	vertex coordinates
v_y	0.0	10.0	1	9	vertex coordinates
v_z	-57.0	10.0	1	10	vertex coordinates
q	0.0	1.0	1	1	charge
beta	0.0	1000.0	0	11	beta
sector	0.0	1.0	0	3	particle sector
chi_sqr	0.0	100.0	0	9	chi squared of track fit
cc_pe	0.0	10.0	0	10	number of photoelectrons in CC
cc_chi_sqr	0.0	1000.0	0	9	not used
trl1_theta	0.0	10.0	0	11	DC1 angle
trl1_phi	0.0	10.0	0	11	DC1 angle
trl1_x	0.0	1.0	0	9	DC1 coordinate
trl1_y	0.0	1.0	0	9	DC1 coordinate
trl1_z	0.0	1.0	0	9	DC1 coordinate
sc_e	0.0	10.0	0	10	energy deposited in SC
ec_in	0.0	100.0	0	8	EC inner energy
ec_out	0.0	100.0	0	8	EC outer energy
ec_tot	0.0	100.0	0	8	EC total energy
ec_pos_x	0.0	1.0	1	10	hit position in EC
ec_pos_y	0.0	1.0	1	10	hit position in EC
ec_pos_z	0.0	1.0	1	10	hit position in EC
ec_m2hit	0.0	1.0	0	11	m2 of EC shower
sc_paddle	0.0	1.0	0	6	TOF paddle identifier
tdc_time	0.0	100.0	0	15	time of flight
track_length	0.0	10.0	0	14	path length
flag	0.0	1.0	1	16	status_EVNT+10

TABLE 30: DST particle variables (added later to use the geometric and timing cuts).

name	offset	multiplier	signed	bits	definition
sc_x	0.0	1.0	1	10	sc position
sc_y	0.0	1.0	1	10	sc position
sc_z	0.0	1.0	1	10	sc position
sc_cx	0.0	1000.0	1	10	sc direction cosine
sc_cy	0.0	1000.0	1	10	sc direction cosine
sc_cz	0.0	1000.0	1	10	sc direction cosine
cc_time	0.0	100.0	0	15	cc time
cc_status	0.0	1.0	0	15	cc status flag
cc_r	0.0	10.0	0	15	cc radial distance
cc_sec	0.0	1.0	0	3	cc sector
sc_time	0.0	100.0	0	15	sc time
sc_status	0.0	1.0	0	15	sc status flag
sc_r	0.0	10.0	0	15	sc radial distance
sc_sec	0.0	1.0	0	3	sc sector

TABLE 31: DST variables: helicity flag

helicity flag	true helicity	state
1	1	first state of the pair
2	0	first state of the pair
3	1	second state of the pair
4	0	second state of the pair
-1	1	bad helicity flag
-2	0	bad helicity flag

APPENDIX B

FIDUCIAL CUTS

B.1 INBENDING FIDUCIAL CUTS

The fiducial cut limits for ϕ and θ are given by:

$$30^\circ - \Delta\phi < \phi < 30^\circ + \Delta\phi \tag{128}$$

and

$$\theta > \theta_{cut}, \tag{129}$$

where the cut limits $\Delta\phi$ and θ_{cut} are defined by

$$\Delta\phi = A \cdot (\sin(\theta - \theta_{cut}))^{exp} \tag{130}$$

with

$$exp = B \cdot \left(p_{el} \cdot \frac{3375\text{A}}{I_{Torus}}\right)^C \tag{131}$$

and

$$\theta_{cut} = D + \frac{E}{(p_{el} + F)\frac{3375\text{A}}{I_{Torus}}}. \tag{132}$$

These cuts are used for the part of analysis where backgrounds and contaminations are calculated. They are not used for asymmetry measurements. Instead, loose cuts that remove the direct PMT hits are used in that case. The table of loose fiducial cuts is also included below.

B.2 OUTBENDING FIDUCIAL CUTS

The following cuts are applied to the outbending data when studying backgrounds and contaminations. The parameter values for the fiducial cut are given in the table. No loose fiducial cuts were applied to the outbending data for asymmetry analysis.

$$30^\circ - \Delta\phi < \phi < 30^\circ + \Delta\phi \tag{133}$$

and

$$\theta_{cut} < \theta < \theta_{high}, \tag{134}$$

where

$$\Delta\phi = A \cdot (\sin(\theta - 6.5^\circ))^{exp} \tag{135}$$

$$exp = B \cdot \left(\frac{1}{4} p_{el}\right)^{C} \tag{136}$$

$$\theta_{cut} = D + E \cdot \left(1 - \frac{1}{4} p_{scale}\right)^{F} \tag{137}$$

$$\theta_{high} = \min(40^{\circ}, \theta_{nom}) \tag{138}$$

$$\theta_{nom} = \frac{35^{\circ}}{(\mathrm{GeV/c})^{1/3}} \cdot \left[\frac{1}{5}\left(p_{el} \cdot \frac{3375\mathrm{A}}{\mid I_{Torus} \mid} + 2.5\mathrm{GeV/c}\right)\right]^{\frac{1}{3}} \tag{139}$$

$$p_{scale} = p_{el} \cdot \frac{1500\mathrm{A}}{\mid I_{Torus} \mid}. \tag{140}$$

TABLE 32: Fiducial cut parameters for the inbending data. Momentum is in GeV and angles are in degrees. These cuts are not used for asymmetry measurements.

Parameter	p <3 GeV	p >3 GeV
A	36	36
B	0.28	0.25
C	0.30	0.30
D	10	10
E	16.72	16.72
F	0.06	0.06
ϕ_{lim}	20	20

TABLE 33: Loose fiducial cut parameters for the inbending data. These cuts remove the direct PMT hits only. They can be applied in case of asymmetry measurements but cannot be applied to any acceptance dependent measurements.

Parameter	p <3 GeV	p >3 GeV
A	41	41
B	0.26	0.26
C	0.30	0.30
D	9	8
E	16.72	16.72
F	0.06	0.06
ϕ_{lim}	21.5	21.5

TABLE 34: Fiducial cut parameters for the outbending data. Momentum is in GeV and angles are in degrees. These cuts are not used for asymmetry measurements but they are used for background analysis.

Parameter	p <3 GeV (−2250 A)	p >3 GeV (−2250 A)	−1500 A
A	34	45	34
B	0.28	0.54	0.33
C	0.22	0.21	0.22
D	5	9.5	6.2
E	3	-4	3
F	1.46	1.2	1.46
G_{upper}	0.15	0.3	0.15
H_{upper}	-0.09	0.1	-0.09
G_{lower}	0.15	0.3	0.15
H_{lower}	-0.09	0.1	-0.09
ϕ_{lim}^{hi}	21	21	21
ϕ_{lim}^{lo}	22	22	22
offset$_{outer}$	1.2	-0.6	1.2
offset$_{inner}$	0	0	0

APPENDIX C

ADDITIONAL TABLES

C.1 PION AND PAIR SYMMETRIC CONTAMINATION PARAMETERS

C.2 SYSTEMATIC ERRORS

C.3 KINEMATIC REGIONS FOR MODEL USAGE IN Γ_1^1 INTEGRATION

TABLE 35: Standard π^-/e^- ratio parameters a and b.

Target	E	Torus	a	b
ND3	1606	1500	-14.27 ± 2.968	0.211 ± 0.092
ND3	1606	-1500	-11.06 ± 2.600	0.217 ± 0.118
NH3	1606	1500	-17.27 ± 3.112	0.289 ± 0.092
NH3	1606	-1500	-11.62 ± 3.205	0.270 ± 0.146
ND3	1723	-1500	-11.06 ± 2.600	0.217 ± 0.118
NH3	1723	-1500	-11.62 ± 3.205	0.270 ± 0.146
NH3	2286	1500	-4.946 ± 1.314	0.006 ± 0.042
ND3	2561	1500	-5.190 ± 1.229	0.022 ± 0.040
ND3	2561	-1500	-4.250 ± 0.775	-0.009 ± 0.035
NH3	2561	-1500	-4.373 ± 0.815	-0.003 ± 0.037
ND3	4238	2250	-4.637 ± 2.096	0.036 ± 0.080
ND3	4238	-2250	-4.192 ± 1.008	0.026 ± 0.049
NH3	4238	2250	-5.051 ± 1.897	0.043 ± 0.073
NH3	4238	-2250	-4.656 ± 1.266	0.045 ± 0.062
ND3	5615	2250	-3.791 ± 1.577	0.023 ± 0.060
NH3	5615	2250	-4.143 ± 2.004	0.030 ± 0.076
ND3	5725	2250	-2.859 ± 1.584	-0.005 ± 0.060
ND3	5725	-2250	-4.322 ± 0.996	0.046 ± 0.047
NH3	5725	2250	-3.631 ± 1.482	0.017 ± 0.057
NH3	5725	-2250	-4.272 ± 0.872	0.042 ± 0.042
ND3	5743	-2250	-4.695 ± 1.022	0.064 ± 0.049
NH3	5743	-2250	-4.333 ± 0.844	0.040 ± 0.040

TABLE 36: Standard π^-/e^- ratio parameters c and d.

Target	E	Torus	c	d
ND3	1606	1500	6.417 ± 3.119	-0.231 ± 0.102
ND3	1606	-1500	3.986 ± 2.703	-0.271 ± 0.126
NH3	1606	1500	9.325 ± 3.013	-0.297 ± 0.093
NH3	1606	-1500	4.386 ± 3.763	-0.326 ± 0.185
ND3	1723	-1500	3.986 ± 2.703	-0.271 ± 0.126
NH3	1723	-1500	4.386 ± 3.763	-0.326 ± 0.185
NH3	2286	1500	0.218 ± 1.404	-0.048 ± 0.047
ND3	2561	1500	-0.011 ± 1.360	-0.042 ± 0.045
ND3	2561	-1500	-0.935 ± 0.828	-0.005 ± 0.036
NH3	2561	-1500	-0.727 ± 0.812	-0.015 ± 0.037
ND3	4238	2250	-0.546 ± 1.574	-0.033 ± 0.060
ND3	4238	-2250	-0.648 ± 0.785	-0.030 ± 0.037
NH3	4238	2250	0.010 ± 1.393	-0.048 ± 0.054
NH3	4238	-2250	-0.381 ± 0.983	-0.042 ± 0.046
ND3	5615	2250	-0.731 ± 1.130	-0.022 ± 0.042
NH3	5615	2250	-0.483 ± 1.402	-0.030 ± 0.053
ND3	5725	2250	-1.488 ± 1.158	0.000 ± 0.044
ND3	5725	-2250	-0.372 ± 0.749	-0.034 ± 0.035
NH3	5725	2250	-0.713 ± 1.049	-0.024 ± 0.040
NH3	5725	-2250	-0.373 ± 0.655	-0.034 ± 0.030
ND3	5743	-2250	-0.191 ± 0.775	-0.045 ± 0.036
NH3	5743	-2250	-0.342 ± 0.630	-0.035 ± 0.029

TABLE 37: Total π^-/e^- ratio parameters a and b.

Target	E	Torus	a	b
ND3	1606	1500	-5.851 ± 1.378	0.117 ± 0.042
ND3	1606	-1500	-2.563 ± 1.299	0.015 ± 0.065
NH3	1606	1500	-6.057 ± 1.484	0.118 ± 0.045
NH3	1606	-1500	-2.703 ± 1.699	0.019 ± 0.086
ND3	1723	-1500	-2.563 ± 1.299	0.015 ± 0.065
NH3	1723	-1500	-2.703 ± 1.699	0.019 ± 0.086
NH3	2286	1500	-2.423 ± 0.761	0.043 ± 0.023
ND3	2561	1500	-2.675 ± 0.663	0.055 ± 0.020
ND3	2561	-1500	-2.728 ± 0.563	0.052 ± 0.022
NH3	2561	-1500	-2.628 ± 0.600	0.046 ± 0.023
ND3	4238	2250	-0.394 ± 0.914	0.039 ± 0.031
ND3	4238	-2250	-1.112 ± 0.651	0.063 ± 0.026
NH3	4238	2250	-0.584 ± 0.881	0.043 ± 0.029
NH3	4238	-2250	-1.204 ± 0.711	0.063 ± 0.029
ND3	5615	2250	0.087 ± 0.516	0.016 ± 0.017
NH3	5615	2250	-0.043 ± 0.585	0.019 ± 0.020
ND3	5725	2250	0.176 ± 0.516	0.014 ± 0.017
ND3	5725	-2250	-0.907 ± 0.411	0.051 ± 0.016
NH3	5725	2250	0.037 ± 0.510	0.018 ± 0.017
NH3	5725	-2250	-0.921 ± 0.404	0.050 ± 0.016
ND3	5743	-2250	-1.012 ± 0.427	0.055 ± 0.017
NH3	5743	-2250	-1.078 ± 0.414	0.053 ± 0.016

TABLE 38: Total π^-/e^- ratio parameters c and d.

Target	E	Torus	c	d
ND3	1606	1500	0.692 ± 1.889	-0.106 ± 0.057
ND3	1606	-1500	-0.334 ± 1.517	-0.088 ± 0.078
NH3	1606	1500	0.950 ± 2.034	-0.110 ± 0.062
NH3	1606	-1500	-0.243 ± 1.995	-0.092 ± 0.104
ND3	1723	-1500	-0.334 ± 1.517	-0.088 ± 0.078
NH3	1723	-1500	-0.243 ± 1.995	-0.092 ± 0.104
NH3	2286	1500	-1.415 ± 0.947	-0.026 ± 0.029
ND3	2561	1500	-1.281 ± 0.788	-0.025 ± 0.024
ND3	2561	-1500	-0.875 ± 0.738	-0.039 ± 0.027
NH3	2561	-1500	-0.933 ± 0.789	-0.037 ± 0.029
ND3	4238	2250	-1.846 ± 0.705	-0.014 ± 0.023
ND3	4238	-2250	-1.066 ± 0.502	-0.041 ± 0.019
NH3	4238	2250	-1.671 ± 0.678	-0.019 ± 0.022
NH3	4238	-2250	-1.013 ± 0.552	-0.044 ± 0.022
ND3	5615	2250	-1.535 ± 0.364	-0.001 ± 0.012
NH3	5615	2250	-1.466 ± 0.418	-0.004 ± 0.014
ND3	5725	2250	-1.558 ± 0.363	0.000 ± 0.012
ND3	5725	-2250	-0.767 ± 0.293	-0.026 ± 0.011
NH3	5725	2250	-1.472 ± 0.360	-0.003 ± 0.012
NH3	5725	-2250	-0.783 ± 0.288	-0.026 ± 0.011
ND3	5743	-2250	-0.707 ± 0.306	-0.030 ± 0.012
NH3	5743	-2250	-0.681 ± 0.294	-0.030 ± 0.011

TABLE 39: e^+/e^- ratio parameters a and b.

Target	E	Torus	a	b
ND3	1606	1500	-5.630 ± 0.058	0.122 ± 0.001
ND3	1606	-1500	-0.959 ± 0.015	0.004 ± 0.000
NH3	1606	1500	-5.962 ± 0.067	0.131 ± 0.002
NH3	1606	-1500	-1.540 ± 0.015	0.014 ± 0.000
ND3	1723	-1500	0.152 ± 0.015	-0.017 ± 0.000
NH3	1723	-1500	0.079 ± 0.015	-0.015 ± 0.000
NH3	2286	1500	-2.126 ± 0.030	0.044 ± 0.000
ND3	2561	1500	-2.225 ± 0.027	0.056 ± 0.000
ND3	2561	-1500	-2.596 ± 0.008	0.063 ± 0.000
NH3	2561	-1500	-1.983 ± 0.009	0.044 ± 0.000
ND3	4238	2250	-1.591 ± 0.050	0.084 ± 0.001
ND3	4238	-2250	-2.419 ± 0.026	0.120 ± 0.001
NH3	4238	2250	-1.645 ± 0.058	0.086 ± 0.002
NH3	4238	-2250	-2.449 ± 0.024	0.118 ± 0.001
ND3	5615	2250	-1.181 ± 0.044	0.086 ± 0.001
NH3	5615	2250	-1.230 ± 0.040	0.087 ± 0.001
ND3	5725	2250	-0.929 ± 0.044	0.076 ± 0.001
ND3	5725	-2250	-2.299 ± 0.018	0.125 ± 0.000
NH3	5725	2250	-1.068 ± 0.039	0.079 ± 0.001
NH3	5725	-2250	-2.308 ± 0.017	0.123 ± 0.000
ND3	5743	-2250	-2.453 ± 0.018	0.126 ± 0.000
NH3	5743	-2250	-2.289 ± 0.017	0.128 ± 0.000

TABLE 40: e^+/e^- ratio parameters c and d.

Target	E	Torus	c	d
ND3	1606	1500	-4.707 ± 0.090	-0.032 ± 0.002
ND3	1606	-1500	-6.743 ± 0.029	0.016 ± 0.001
NH3	1606	1500	-4.221 ± 0.104	-0.046 ± 0.003
NH3	1606	-1500	-6.397 ± 0.028	0.004 ± 0.001
ND3	1723	-1500	-6.663 ± 0.028	0.025 ± 0.001
NH3	1723	-1500	-6.564 ± 0.027	0.021 ± 0.001
NH3	2286	1500	-3.952 ± 0.042	-0.003 ± 0.001
ND3	2561	1500	-3.538 ± 0.038	-0.013 ± 0.001
ND3	2561	-1500	-3.269 ± 0.013	-0.025 ± 0.000
NH3	2561	-1500	-3.908 ± 0.015	-0.013 ± 0.000
ND3	4238	2250	-1.899 ± 0.039	-0.052 ± 0.001
ND3	4238	-2250	-1.190 ± 0.022	-0.084 ± 0.001
NH3	4238	2250	-1.885 ± 0.045	-0.053 ± 0.001
NH3	4238	-2250	-1.208 ± 0.020	-0.083 ± 0.000
ND3	5615	2250	-1.079 ± 0.033	-0.065 ± 0.001
NH3	5615	2250	-1.025 ± 0.030	-0.068 ± 0.001
ND3	5725	2250	-1.169 ± 0.033	-0.061 ± 0.001
ND3	5725	-2250	-0.415 ± 0.015	-0.090 ± 0.000
NH3	5725	2250	-1.097 ± 0.029	-0.063 ± 0.001
NH3	5725	-2250	-0.434 ± 0.014	-0.089 ± 0.000
ND3	5743	-2250	-0.417 ± 0.015	-0.089 ± 0.000
NH3	5743	-2250	-0.438 ± 0.014	-0.093 ± 0.000

TABLE 41: Systematic errors $\sigma_{sys}^{percent}$ for each Q^2 bin as a percentage of statistical errors on $A_1 + \eta A_2$ for the deuteron are listed for 1 GeV data. The percentage values are calculated according to Eq. (105) and evaluated in $1.15 < W < 2.60$ GeV.

Q^2 bin	Total	Back.	Dilution	Radiative	$P_b P_t$	Model	Pol. Back.
4	11	0.02	6	3	9	0.8	1
5	11	0.02	5	3	10	0.8	1
6	13	0.04	6	4	11	1	1
7	11	0.04	3	4	9	0.8	1
8	10	0.04	3	4	8	0.9	1
9	11	0.06	3	5	9	1	1
10	11	0.06	3	6	9	1	1
11	12	0.07	3	6	10	1	2
12	13	0.08	4	6	11	2	2
13	14	0.07	5	6	11	2	2
14	13	0.07	4	6	12	2	2
15	13	0.07	4	6	11	2	2
16	12	0.05	3	7	10	2	2
17	13	0.06	4	10	8	3	3
18	14	0.05	3	11	7	3	3
19	15	0.07	4	12	8	3	3
20	16	0.07	4	13	8	3	4
21	16	0.2	4	12	9	3	4
22	16	0.2	4	12	9	3	5
23	14	0.1	4	10	8	3	4
24	13	0.1	4	10	7	3	4
25	11	0.06	3	9	6	2	2
26	10	0.05	3	7	6	2	2

TABLE 42: Systematic errors $\sigma_{sys}^{percent}(Q^2)$ on $A_1 + \eta A_2$ for the deuteron are listed for 2 GeV data. The percentage values are calculated according to Eq. (105) and evaluated in $1.15 < W < 2.60$ GeV.

Q^2 bin	Total	Back.	Dilution	Radiative	$P_b P_t$	Model	Pol. Back.
8	6	0.5	2	2	6	0.7	0.8
9	7	0.5	2	3	6	0.9	0.9
10	10	0.8	3	4	9	1	1
11	8	0.5	2	3	7	1	1
12	8	0.4	2	3	7	1	1
13	9	0.4	3	3	8	2	1
14	9	0.4	3	4	8	2	1
15	10	0.4	3	6	8	2	1
16	11	0.4	3	7	8	2	2
17	11	0.3	3	7	8	2	2
18	12	0.3	3	7	8	2	2
19	11	0.3	3	8	8	2	2
20	12	0.4	3	8	8	3	2
21	13	0.4	3	9	8	3	3
22	14	0.4	4	10	8	3	3
23	13	0.4	3	9	8	3	4
24	15	0.4	4	10	8	3	4
25	21	1	6	12	15	5	5
26	16	0.5	5	11	10	4	5
27	14	0.4	4	9	9	3	4
28	13	0.4	4	8	9	3	4
29	11	0.3	4	7	8	2	3
30	8	0.2	2	5	5	1	2

TABLE 43: Systematic errors $\sigma_{sys}^{percent}(Q^2)$ on $A_1 + \eta A_2$ for the deuteron are listed for 4 GeV data. The percentage values are calculated according to Eq. (105) and evaluated in $1.15 < W < 2.60$ GeV.

Q^2 bin	Total	Back.	Dilution	Radiative	$P_b P_t$	Model	Pol. Back.
13	15	0.9	3	3	14	2	1
14	10	0.6	2	2	9	1	1
15	11	0.5	2	2	10	1	1
16	12	0.5	2	3	11	2	1
17	11	0.4	2	3	10	2	1
18	9	0.4	2	3	8	2	1
19	12	0.5	2	4	11	2	1
20	12	0.6	2	4	11	2	1
21	10	0.4	2	4	9	2	1
22	13	0.5	2	5	11	2	2
23	12	0.4	2	5	10	2	2
24	14	0.5	2	6	12	3	2
25	14	0.5	2	6	12	3	2
26	15	0.5	3	7	12	3	3
27	15	0.5	3	7	13	3	3
28	16	0.5	3	7	13	3	3
29	16	0.5	4	6	13	3	3
30	16	0.5	4	6	13	3	3
31	16	0.5	4	6	14	3	3
32	14	0.4	3	5	12	2	3
33	12	0.3	3	4	11	2	2
34	11	0.2	3	4	10	2	2

TABLE 44: Systematic errors $\sigma_{sys}^{percent}(Q^2)$ on $A_1 + \eta A_2$ for the deuteron are listed for 5 GeV data. The percentage values are calculated according to Eq. (105) and evaluated in $1.15 < W < 2.60$ GeV.

Q^2 bin	Total	Back.	Dilution	Radiative	$P_b P_t$	Model	Pol. Back.
19	20	1	2	3	19	2	0.9
20	25	1	2	4	24	2	1
21	18	2	2	3	18	2	1
22	19	1	1	3	18	2	1
23	18	2	1	4	18	2	1
24	20	2	2	5	20	3	2
25	21	1	3	5	20	3	2
26	22	1	3	5	21	3	2
27	21	1	3	5	20	3	2
28	20	1	3	6	19	3	3
29	21	1	3	6	20	3	3
30	20	1	4	6	19	3	3
31	22	1	4	6	21	3	4
32	21	1	3	5	20	3	4
33	23	1	4	5	22	2	4
34	22	0.9	3	4	21	2	3
35	20	0.6	3	4	19	2	3
36	18	0.4	2	3	17	1	2

TABLE 45: Systematic errors on g_1 deuteron for each Q^2 bin as a percentage of the statistical errors, as given in Eq. (105). The percentage values are evaluated in $1.15 < W < 2.60$ GeV.

Q^2 bin	Total	Back.	Dilution	Radiative	$P_b P_t$	Model	Pol. Back.
6	18	0.05	8	5	15	4	2
7	11	0.03	4	4	9	2	1
8	9	0.04	2	4	8	2	1
9	11	0.1	2	5	9	2	1
10	11	0.4	3	5	9	3	1
11	11	0.3	2	5	9	2	1
12	12	0.3	3	5	10	3	2
13	11	0.3	3	5	9	3	2
14	11	0.4	3	5	9	3	1
15	10	0.4	3	6	8	3	1
16	17	0.5	3	7	15	4	2
17	12	0.4	3	9	8	4	2
18	13	0.3	2	10	7	5	2
19	16	0.3	3	13	8	7	2
20	16	0.3	3	14	7	7	2
21	16	0.4	2	14	7	7	2
22	16	0.5	2	14	8	7	2
23	16	0.6	2	13	8	8	2
24	17	0.6	2	15	8	9	3
25	18	0.6	2	16	9	10	3
26	20	0.6	2	17	9	12	3
27	18	0.6	2	15	10	10	3
28	17	0.6	3	11	12	7	3
29	17	0.7	3	9	13	5	3
30	17	0.7	3	9	14	4	3
31	19	0.8	3	9	16	4	4
32	19	0.7	3	9	16	4	4
33	22	0.9	3	9	20	4	3
34	21	0.8	3	7	19	4	3
35	20	0.7	3	6	19	3	3
36	19	0.5	4	5	18	3	2
37	18	0.3	4	4	17	3	1
38	7	0.08	3	1	6	1	0.4

TABLE 46: Systematic errors on g_1 deuteron for Q^2 bins, as a percentage of statistical errors, calculated according to Eq. (105). The percentage values are evaluated in three different regions: Total ($1.15 < W < 2.60$ GeV); Region1 ($1.15 < W < 1.30$ GeV); Region2 ($1.30 < W < 2.00$ GeV); Region3 ($2.00 < W < 2.50$ GeV).

Q^2 bin	Total	Region1	Region2	Region3
6	18	0	18	0
7	11	0	11	0
8	9	0	9	0
9	11	12	11	6
10	11	12	10	17
11	11	14	10	8
12	12	17	11	5
13	11	16	9	9
14	11	16	10	4
15	10	14	9	13
16	17	14	10	30
17	12	17	12	11
18	13	19	14	8
19	16	21	17	12
20	16	24	18	10
21	16	21	19	9
22	16	19	19	10
23	16	15	19	12
24	17	14	22	12
25	18	12	23	12
26	20	10	26	13
27	18	9	22	14
28	17	9	17	16
29	17	10	16	19
30	17	10	15	19
31	19	11	16	23
32	19	11	15	24
33	22	10	16	26
34	21	13	20	25
35	20	16	21	19
36	19	18	19	22
37	18	21	17	0
38	7	7	0	0
N_{Q^2}	Av. Total	Av. Region1	Av. Region2	Av. Region3
33	15	14	16	15

TABLE 47: W regions (in GeV) used for Γ_1 calculation. Model was used where data is not available.

bin	Q^2	model	data	model	data	model
10	0.049	1.08 - 1.14	1.15 - 1.59	1.60 - 2.99	-	3.00 - 7.10
11	0.059	1.08 - 1.14	1.15 - 1.59	1.60 - 2.99	-	3.00 - 7.74
12	0.070	1.08 - 1.14	1.15 - 1.59	1.60 - 1.84	1.85 - 1.99	2.00 - 8.45
13	0.084	1.08 - 1.14	1.15 - 1.79	1.80 - 2.99	-	3.00 - 9.23
14	0.101	1.08 - 1.14	1.15 - 1.79	1.80 - 2.99	-	3.00 - 10.10
15	0.120	1.08 - 1.14	1.15 - 1.83	1.84 - 2.99	-	3.00 - 11.00
16	0.144	1.08 - 1.14	1.15 - 1.83	1.84 - 2.99	-	3.00 - 12.00
17	0.171	1.08 - 1.14	1.15 - 2.19	2.20 - 2.99	-	3.00 - 13.10
18	0.205	1.08 - 1.14	1.15 - 2.19	2.20 - 2.99	-	3.00 - 14.30
19	0.244	1.08 - 1.14	1.15 - 2.19	2.20 - 2.39	2.40 - 2.59	2.60 - 15.60
20	0.292	1.08 - 1.14	1.15 - 2.19	2.20 - 2.99	-	3.00 - 17.10
21	0.348	1.08 - 1.14	1.15 - 2.24	2.25 - 2.99	-	3.00 - 18.70
22	0.416	1.08 - 1.14	1.15 - 2.59	2.60 - 2.99	-	3.00 - 20.40
23	0.496	1.08 - 1.14	1.15 - 2.59	2.60 - 2.99	-	3.00 - 22.30
24	0.592	1.08 - 1.14	1.15 - 2.59	2.60 - 2.99	-	3.00 - 24.30
25	0.707	1.08 - 1.14	1.15 - 2.79	2.80 - 2.99	-	3.00 - 26.60
26	0.844	1.08 - 1.14	1.15 - 2.89	2.90 - 2.99	-	3.00 - 29.00
27	1.01	1.08 - 1.14	1.15 - 2.89	2.90 - 2.99	-	3.00 - 31.80
28	1.2	1.08 - 1.14	1.15 - 2.89	2.90 - 2.99	-	3.00 - 34.60
29	1.44	1.08 - 1.14	1.15 - 2.89	2.90 - 2.99	-	3.00 - 37.90
30	1.71	1.08 - 1.14	1.15 - 2.89	2.90 - 2.99	-	3.00 - 41.30
31	2.05	1.08 - 1.14	1.15 - 2.79	2.80 - 2.99	-	3.00 - 45.30
32	2.44	1.08 - 1.14	1.15 - 2.59	2.60 - 2.99	-	3.00 - 49.40
33	2.92	1.08 - 1.14	1.15 - 2.59	2.60 - 2.99	-	3.00 - 54.00
34	3.48	1.08 - 1.14	1.15 - 2.49	2.50 - 2.99	-	3.00 - 59.00
35	4.16	1.08 - 1.14	1.15 - 2.29	2.30 - 2.99	-	3.00 - 64.50
36	4.96	1.08 - 1.14	1.15 - 1.99	2.00 - 2.99	-	3.00 - 70.40
37	5.92	1.08 - 1.14	1.15 - 1.59	1.60 - 2.99	-	3.00 - 76.90

APPENDIX D

DEUTERON STRUCTURE FUNCTIONS

D.1 EXTRACTION OF NEUTRON INFORMATION FROM A DEUTERON TARGET

One of our purposes is to extract neutron information from the deuteron and proton data. In order to extract the nucleon structure function from a measurement on a nucleus, we need to understand the effects of the nuclear medium on the nucleon structure. Once we understand these effects, we can make the necessary corrections on the deuteron structure function and extract the neutron information by using deuteron and proton data. Moreover, by comparing our results to the available neutron data from ^{3}He targets [71], for example, we can justify our understanding of the nuclear medium and its effects on the nucleon structure. The EG1b data will make an important contribution to the neutron spin structure and reduce the uncertainties substantially over a good kinematic range of x and Q^2.

In the resonance region, for spin structure functions, the most important nuclear effects are considered to be the Fermi motion and the depolarizing effect of the D-wave [72]. The correction for the depolarizing effect of the D-wave can be approximated by an overall factor $(1 - 1.5w_D)$ that describes the average polarization of nucleons inside a fully polarized deuteron. Although this is the most important correction for $x < 0.7$, the additional corrections are required, especially for larger x [73], the most important of which being the Fermi motion. There are additional effects such as off-shell mass effect and the EMC effect that should be considered. However, those are found to be relatively small corrections [72]. In the following sections, we summarize the corrections required to extract neutron information from deuteron and proton data.

Fermi Motion

Bound nucleons are moving inside the nucleus, causing kinematic shifts and Doppler broadening of peaks in the cross section. If we assume that the proton and neutron spin structure functions have similar behavior in the resonance region, the positions of the nucleon resonances should be the same for both nucleons. However, in case of the deuteron, the resonance peaks may be smeared and shifted because of the

Fermi motion of the nucleons. If one tries to extract the neutron structure functions by subtracting the proton from the deuteron, the maximum of the proton structure function may become the minimum of the neutron structure function. This turns the Fermi smearing into an important effect to consider while extracting neutron information from the deuteron and proton data.

Recently it was suggested by [74] that a convolution method can be used iteratively to take these effects into account and extract the neutron structure functions from nuclear data. The method uses convoluted proton and neutron structure functions (SFs) to model the deuteron and relies on the knowledge of the proton and deuteron to iteratively extract the neutron SFs. A predefined input function for the neutron is evolved iteratively until the function becomes stable. Currently, the convolution only corrects for the Fermi motion and the D-state of the deuteron and disregards other nuclear effects. Still, the method is suitable to incorporate other corrections as they are modeled. It has been successfully tried on the unpolarized structure functions. However, the convolution method is only well proven for functions with no sign change. On the other hand, the spin structure function g_1 has several sign changes in the resonance region. This causes the iterative method to fail in some kinematic regions. This mainly happens if one uses data with errors for the proton and deuteron. Using parameterizations of the structure functions, instead, makes the method more reliable. The results of the EG1b experiment, with both the proton and the deuteron data, provides a perfect environment to test this method. More information on this together with parameterizations of the world asymmetry data are given in chapter III.

Off-Mass Shell Effects

The deuteron is made up of a proton and a neutron. But because of the negative contribution coming from the binding energy to the overall mass of deuterium, $M_d = M_p + M_n - 2.2$ MeV, both nucleons cannot be on the mass shell at the same time. Moreover, the nucleons will also have relativistic motion and their total energy should be calculated by $\sqrt{M_p^2 + p_p^2} + \sqrt{M_n^2 + p_n^2} \gg M_d$, therefore, the mass of a bound nucleon is much smaller than that of a free one in this picture. Various corrections for this off-shell effect have been proposed. It is included in the smearing prescription of [74] up to 2nd order in the momenta.

EMC Effect

This effect can be summarized as the observed dependence of the cross section per nucleon on the nuclear medium. It was first observed by the EMC Collaboration [43]. It is due to the distortion of the free-nucleon structure function by the nuclear medium. The effect has a strong kinematical dependence being most pronounced at large $x > 0.5$. However, currently we don't have a reliable model of the EMC effect in the deuteron, thus, this effect is not included into our method to extract the neutron SF from the deuteron data. More information on the EMC effect can be found in [7][75][76].

Effects of non-nucleonic states

Effects of nucleonic resonance states and pions (meson exchange currents) as part of the structure of the deuteron should also be considered. According to the six quark bag model of the deuteron, one should include direct correlations between quarks and gluons in the proton and neutron. Finally, one could consider nuclear shadowing, which is re-scattering of the lepton from both nucleons in the deuteron or from the meson cloud within the nucleus. However, there is no universally accepted quantitative model for the deuteron which corrects for these effects.

BIBLIOGRAPHY

[1] R. Fersch, "Measurement of Inclusive Proton Double-Spin Asymmetries and Polarized Structure Functions in the CLAS EG1b Experiment", 2012. URL: http://www.jlab.org/Hall-B/secure/eg1/EG2000/fersch/softwarenote/AnalysisNote/

[2] S.E. Kuhn. "Nucleon Structure Functions: Experiments and Models," Lecture notes from HUGS (Hampton University Graduate Studies at JLab) lectures (1997).

[3] H. Fritzsch and G. Eldahoumi, "Constituent Quarks and the Spin of the Proton," arXiv:hep-ph/0906.1139 (2009).

[4] R. P. Feynman, "Proceedings of the 3rd Topical Conference on High Energy Collision of Hadrons," Stony Brook, N. Y. (1969).

[5] J. D. Bjorken and E. A. Paschos, "Inelastic Electron-Proton and $\gamma-$Proton Scattering and the Structure of the Nucleon," Phys. Rev. **185**, 1975 (1969).

[6] J. D. Bjorken, "Asymptotic Sum Rules at Infinite Momentum," Phys. Rev. **179**, 1547 (1969).

[7] J.J. Aubert *et al.*, Phys. Lett. B 123, **275** (1983).

[8] S. E. Kuhn, J. P. Chen and E. Leader, "Spin Structure of the Nucleon - Status and Recent Results," Prog. Part. Nucl. Phys. **63**, 1 (2009) [arXiv:hep-ph/0812.3535].

[9] F. Halzen and A. D. Martin, *Quarks and Leptons*, New York: John Wiley & Sons (1979).

[10] E. Leader and E. Predazzi, *An introduction to gauge theories and the "new physics"*, Cambridge university Press (1982).

[11] T. Pussieux and R. Windmolders, *A collection of formulas for spin dependent deep inelastic scattering*, (Unpublished).

[12] J. Soffer and O. V. Teryaev, hep-ph/9906455.

[13] M. Osipenko *et al.* [CLAS Collaboration], "The deuteron structure function F2 with CLAS", arXiv:hep-ex/0507098 (2005).

[14] C.S. Armstrong, *et al.*, Phys. Rev. D **63** 094008 (2001). [hep-ph/0104055].

[15] P. Hoodbhoy, R. L. Jaffe and A. Manohar, Nucl. Phys. B **312**, 571 (1989).

[16] A. Airapetian *et al.*, Phys. Rev. Lett. **95** 242001 (2005) [arXiv:hep-ex/0506018]

[17] F. E. Close, *An Introduction to Quarks and Partons*, London: Academic Press (1984). [ISBN 0-12-175150-3]

[18] Y. Prok, "Measurement of the Spin Structure Function $g_1(x, Q^2)$ of the Proton Measured in the Resonance Region," Ph.D. diss., University of Virginia, 2004.

[19] V. N. Gribov and L.N. Lipatov, Sov. J. Nucl. Phys. **15**, 138 (1972); Y.L. Dokahitzer, Sov. Phys. JETP. **16**, 161, (1977); G. Altarelli and G. Parisi, Nucl. Phys. B **126**, 298 (1977).

[20] B. W. Filippone and X. Ji, Adv. Nucl. Phys. **26**, 1 (2001).

[21] E. Leader, *Spin in particle physics*, Cambridge Monogr. Part. Phys. Nucl. Phys. Cosmol. 15 (2001).

[22] W. Melnitchouk and W. Weise, arXiv:hep-ph/0006170 (2000).

[23] B. Lampe and E. Reya, "Spin physics and polarized structure functions," Phys. Rep. **332** 1 (2000).

[24] K. Wilson, Phys. Rev. **179**, 1499 (1969); R. A. Brandt and G. Preparata, Nucl. Phys. B **27**, 541 (1971); O. Nachtmann, Nucl. Phys. B **63**, 237 (1973).

[25] Z.E. Meziani, arXiv:hep-ph/0404066 (2004).

[26] M. Osipenko, arXiv:hep-ph/0404195 (2004).

[27] A. Deur, "Higher-twist analysis of moments of spin structure function," arXiv:nucl-ex/0508022 (2005).

[28] X. Ji and P. Unrau, Phys. Lett. B **333**, 228 (1994).

[29] C. E. Carlson and N. C. Mukhopadhyay, Phys. Rev. D **58**, 094029 (1998).

[30] J. Edelmann, G. Piller, N. Kaiser and W. Weise, Nucl. Phys. A **665**, 125 (2000).

[31] A. Thomas and W. Weise, *The structure of the nucleon*, Wiley-VCH, Berlin (2001).

[32] E.D. Bloom and F.J. Gilman, "Scaling, Duality, and the Behavior of Resonances in Inelastic electron-Proton Scattering," Phys. Rev. Lett. **25** 1140 (1970).

[33] W. Melnitchouk, R. Ent, and C. Keppel, Phys. Rep. **406**, 127 (2005).

[34] F.E. Close and W. Melnitchouk, "Symmetry breaking and quark-hadron duality in structure functions," Phys. Rev. C **68** 035210 (2003).

[35] J. Blmlein and A. Tkabladze, Nucl. Phys. B **553**, 427 (1999).

[36] I. Niculescu *et al.*, Phys. Rev. Lett. **85**, 1186 (2000).

[37] P.E. Bosted *et al.*, "Quark-hadron duality in spin structure functions g_1^p and g_1^d," Phys. Rev. C **75**, 035203 (2007).

[38] T.A. Forest, GDH 2004 Proceedings, p84, World Scientific (2004).

[39] De Rujula, H. Georgi and H.D. Politzer, Ann. Phys. **103**, 315 (1977).

[40] F. E. Close and N. Isgur, Phys. Lett. B **509**, 81 (2001).

[41] Z. Dziembowski and J. Franklin, Nucl. Part. Phys. 17 **213**, (1991).

[42] David Griffiths, *Introduction to Elementary Particles*, New York: John Wiley & Sons (1987).

[43] M. Anselmino, A. Efremov, E. Leader, CERN Reports TH/7216/94 (1994).

[44] P. L. Anthony *et al.*, E142 Collaboration, Phys. Rev. D **54**, 6620 (1996).

[45] B. Adeva *et al.*, Spin Muon Collaboration, Phys. Rev. D **58**, 112001 (1998).

[46] K. Abe *et al.*, E143 Collaboration, Phys. Rev. D **58**, 112003 (1998) [arXiv:hep-ph/9802357].

[47] K. Abe *et al.*, E154 Collaboration, Phys. Lett. B **405**, 180 (1997).

[48] P. L. Anthony *et al.*, E155 Collaboration, Phys. Lett. B **493**, 19 (2000); arXiv:hep-ex/9904002.

[49] A. Airapetian *et al.*, HERMES Collaboration, Phys. Rev. D **75**, 012007 (2007); Phys. Lett. B **404**, 383 (1997).

[50] V. Y. Alexakhin *et al.*, COMPASS Collaboration, Phys. Lett. B **647**, 8 (2007).

[51] K. V. Dharmawardane *et al.* [CLAS Collaboration], Phys. Lett. B **641**, 11 (2006) [arXiv:nucl-ex/0605028].

[52] S. L. Adler, Phys. Rev. **177**, 2426 (1969).

[53] R. D. Carlitz, J. C. Collins and A. H. Mueller, Phys. Lett. B **214**, 229 (1988).

[54] S.B. Gerasimov, Sov. J. of Nucl. Phys. **2**, 430 (1966).

[55] S.D. Drell and A.C. Hearn, Phys. Rev. Lett. **16**, 908 (1966).

[56] K. Helbing, "The Gerasimov-Drell-Hearn sum rule," Prog. Part. Nucl. Phys. **57**, 405 (2006) [arXiv:nucl-ex/0603021].

[57] D. Drechsel, B. Pasquini, and M. Vanderhaeghen, Phys. Rep. **378**, 99 (2003).

[58] H. Arenhovel *et al.*, GDH 2004 Proceedings, p294, World Scientific (2004).

[59] X. Ji and J. Osborne, J. Phys. G **27**, 127 (2001) [arXiv:hep-ph/9905410].

[60] X. Ji, C. Kao, and J. Osborne, Phys. Lett. B **472**, 1 (2000).

[61] V. Bernard, T.R. Hemmert, and U.G. Meisner, Phys. Lett. B **545**, 105 (2002).

[62] Drechsel, D., S. S. Kamalov, and L. Tiator, Phys. Rev. D **63**, 114010 (2001).

[63] M. Anselmino, B.L. Ioffe and E. Leader, Sov. J. Nucl. Phys. **49**, 136 (1989).

[64] V. D. Burkert and B. L. Ioffe and E. Leader, Phys. Lett. B **296**, 223 (1992).

[65] J. J. Sakurai, *Currents and Mesons*, University of Chicago Press, Chicago (1969).

[66] J. Soffer and O. V. Teryaev, Phys. Rev. D **51**, 25 (1995); J. Soffer and O. V. Teryaev, Phys. Rev. D **56**, 7458 (1997).

[67] H. Burkhardt and W.N. Cottingham, Ann. Phys. (NY) **56**, 453 (1970).

[68] J. Yun *et al.*, Phys. Rev. C **67**, 055204 (2003).

[69] R. Fatemi *et al.*, "Measurement of the Proton Spin Structure Function $g_1(x, Q^2)$ for Q^2 from 0.15 to 1.6 GeV^2 with CLAS," Phys. Rev. Lett. **91**, 2220022 (2003).

[70] O.A. Rondon, Phys. Rev. C **60**, 035201 (1999).

[71] X. Zheng, GDH 2004 Proceedings, p73, World Scientific (2004); X. Zheng *et al.*, Phys. Rev. Lett. 92, 012004 (2004).

[72] C. Ciofi degli Atti, L. P. Kaptari, S. Scopetta and A. Y. Umnikov, "The Neutron Spin Structure Function from the Deuteron Data in the Resonance Region," Phys. Lett. B **376**, 309 (1996) [arXiv:nucl-th/9601045].

[73] W. Melnitchouk, Nucl. Phys. A **631**, 296C (1997) [arXiv:hep-ph/9708484].

[74] Y. Kahn, W. Melnitchouk and S. A. Kulagin, "New method for extracting neutron structure functions from nuclear data," Phys. Rev. C **79**, 035205 (2009) [arXiv:nucl-th/0809.4308].

[75] D. F. Geesaman, K. Saito and A.W. Thomas, Annu. Rev. Nucl. Part. Sci. **45** 337 (1995).

[76] W. Bentz, I. C. Cloet and A. W. Thomas, "The polarized EMC effect," AIP Conf. Proc. **892**, 248 (2007).

[77] B. A. Mecking, *et al.*, "The CEBAF large acceptance spectometer (CLAS)," Nucl. Instr. Meth. **A 503**, 513 (2003).

[78] V. Dharmawardane, "Spin Structure Functions of the Deuteron Measured with CLAS In and Above the Resonance Region," Ph.D. diss., Old Dominion University (2004).

[79] M. D. Mestayer *et al.*, Nucl. Instr. and Meth. A **449**, 81 (2000).

[80] L. Qin *et al.*, CLAS-NOTE **1996-018** JLAB (1996).

[81] E. S. Smith *et al.*, Nucl. Instr. and Meth. A **432**, 265 (1999).

[82] G. Adams *et al.*, Nucl. Instr. and Meth. A **465**, 414 (2001).

[83] M. Amarian *et al.*, Nucl. Instr. and Meth. A **460**, 239 (2001).

[84] C. D. Keith *et al.*, "A polarized target for the CLAS detector," Nucl. Instr. and Meth. A **501**, 327 (2003).

[85] S. Stepanyan, "Simple Event Builder (SEB) in the framework of RECSIS,"

`http://www.jlab.org/~stepanya/seb_man.html`

[86] Jefferson Lab Computing,

`https://wiki.jlab.org/cc/external/wiki/index.php/Scientific_Computing`

[87] Harut Avagyan, *et al.*, "The CLAS Calibration Database," CLAS-NOTE **2001-003** JLAB (2001).

[88] E.S. Smith *et al.*, "The time-of-flight system for CLAS," Nucl. Instr. Meth. **A 432**, 265 (1999).

[89] E.S. Smith, V.Dharmawardane, *et al.*, "Calibration of the CLAS TOF System," CLAS-NOTE **1999-011** JLAB (1999). (Updated in 2001).

[90] C. Smith, EC Energy Calibration,

`http://www.jlab.org/~lcsmith/EC_Energy_Calibration.html`

[91] L.M. Qin *et al.*, "Prototype studies and design considerations for the CLAS Region 2 drift chambers," Nucl. Instr. Meth. **A 411**, 265 (1998).

[92] Dieter Cords *et al.*, "CLAS Event Format with BOS," CLAS-NOTE **1994-005** JLAB (1994).

[93] "HELicity Physics analysis for EG1b,"

`http://www.jlab.org/~claseg1/analysis/eg1b/HelP.html`

[94] S. Kuhn and N. Guler, "False Asymmetry Studies for EG1b Experiment," CLAS-NOTE **2005-005** JLAB (2005).

[95] W.M. Yao *et al.*, (Particle Data Group), "The Review of Particle Physics," J. Phys. G**33**, 1 (2007).

[96] Robert Fersch, "Measurement of Inclusive Proton Double-Spin Asymmetries and Polarized Structure Functions in the CLAS EG1B Experiment," Ph.D. diss., The College of William and Marry (2008).

[97] "Quality Checks for the EG1b 4.2 and 2.5 GeV data sets,"

http://www.jlab.org/Hall-B/secure/eg1/EG2000/nevzat/QUALITY_CHECKS/

[98] "Quality Checks for the EG1b experiment,"

http://www.jlab.org/Hall-B/secure/eg1/EG2000/fersch/QUALITY_CHECKS/

[99] M. Osipenko, A. Vlassov and M. Taiuti, "Matching between the electron candidate track and the Cherenkov counter hit," CLAS-NOTE **2004-020** JLAB (2004).

[100] "Geometric and Timing Cuts for EG1b,"

http://www.jlab.org/Hall-B/secure/eg1/EG2000/nevzat/GEOM_CC_CUTS/

[101] A. Vlassov, "CLAS Cherekov Counter study,"

http://www.jlab.org/~vlassov/cc/index.html

[102] Peter Posted, S. Kuhn, Y. Prok, "Raster Corrections for EG1B," CLAS-NOTE **2003-008** JLAB (2003).

[103] M. Bellis, "Reliability and Limitations of GSIM," CLAS-NOTE **2002-016** JLAB (2002).

[104] P. Bosted and H. Avakian, "Multiple Scattering and Stray Magnetic Field Corrections for Tracking in the Presence of Target Field," CLAS-NOTE **2006-006** JLAB (2006). (The magnetic field correction is updated later.)

[105] H. Avakian, personal correspondence.

[106] "Hall A Absolute Beam Energy Measurements,"

http://hallaweb.jlab.org/equipment/beam/energy/absolute_beam_energy.html

[107] Glenn F. Knoll, *Radiation Detection and Measurement*, New York: John Wiley & Sons (2000).

[108] W.M. Yao *et al.*, (Particle Data Group), "The Review of Particle Physics," J. Phys. G**33**, 1 (2007).

[109] William R. Leo, *Techniques for Nuclear and Particle Physics Experiments*, Berlin: Springer-Verlag (1994)

[110] S.E. Kuhn, A.V. Klimenko, "Momentum corrections for E6," CLAS-NOTE **2003-005** JLAB (2003).

[111] CEBAF Hall B Conceptual Design Report (1990).

[112] F. James, "MINUIT Function Minimization and Error Analysis Reference Manual,".

`http://wwwasdoc.web.cern.ch/wwwasdoc/minuit/minmain.html`

[113] P. Bosted and R. Fersch *et al*, "Ratios of ^{15}N/^{12}C and ^{4}He/^{12}C inclusive electroproduction cross-sections in the nucleon resonance region," Phys. Rev. C **78** 015202 (2008) [arXiv:nucl-ex/0712.2438v3].

[114] S. Kuhn, "Data Analysis for EG1" (analysis document),

`http://www.jlab.org/Hall-B/secure/eg1/AnalysisDoc/EG2000DataAnalyis.pdf`

[115] D.R. Lide, ed. *CRC Handbook of Chemistry and Physics, 78th Ed.* Boca Raton, FL: CRC Press (1997).

[116] Peter Posted, "Pair Symmetric and Pion Backgrounds for EG1B," CLAS-NOTE **2004-005** JLAB (2004).

[117] J. Arrington, "Implications of the discrepancy between proton form factor measurements," Phys. Rev. C **69**, 022201 (2004).

[118] "$P_b P_t$ studies for EG1b,"

`http://www.jlab.org/Hall-B/secure/eg1/EG2000/nevzat/PBPT/Comparisons`

[119] M. Mayer, CLAS NOTE 2012 - 004 (2012).

[120] K. Abe *et al.*, Phys. Rev. D **58**, 112003 (1998).

[121] T.V. Kuchto and N.M. Shumeiko, "Radiative Effects in Deep Inelastic Scattering of Polarized Leptons by Polarized Nucleons," Nucl. Phys. **B219**, 412 (1983).

[122] L.W. Mo and Y.S. Tsai, "Radiative Corrections to Elastic and Inelastic *ep* and μp Scattering," Rev. Mod. Phys. **41**, 205 (1969).

[123] F.R. Wesselmann, "Precision Measurement of the Spin Structure of the Proton and the Deuteron in the." Ph.D. diss., Old Dominion University (2000).

[124] P.E. Bosted and M.E. Christy, "Empirical Fit to Inelastic Electron-Deuteron and Electron-Neutron Resonance Region Transverse Cross Sections," Phys. Rev. C **77**, 065206 (2008).

[125] M.E. Christy and P.E. Bosted, "Empirical Fit to Precision Inclusive Electron-Proton Cross Sections in the Resonance Region," arXiv:0712.3731 (2007).

[126] D. Gabbert and L. De Nardo, DESY report **07-107**, hep-ph/0708.3196v1, (2007).

[127] K. Abe *et al.*, Phys. Lett. **B452**, 194 (1999).

[128] H. Dutz *et al.*, Phys. Rev. Lett. 91, 192001 (2003).

[129] H. Dutz *et al.*, Phys. Rev. Lett. 94, 162001 (2005).

[130] H. Dutz *et al.*, Phys. Rev. Lett. 93, 032003 (2004)

[131] `http://wwwkph.kph.uni-mainz.de/MAID//maid2007/`

[132] Octavian Florin Filoti, Ph.D. diss., pages 190-194, University of New Hampshire (2007).

[133] K. Slifer *et al.* [Resonance Spin Structure Collaboration], "Spin Structure Moments of the Proton and Deuteron," arXiv:0812.0031 [nucl-ex].

[134] O. A. Rondon, AIP Conf. Proc. **842**, 395 (2006).

[135] `http://www.jlab.org/Hall-B/secure/eg1/EG2000/nevzat/MODELS/`

[136] Oscar A. Rondon and Karl Slifer, personal correspondence.

[137] M. Amarian *et al.*, "The Q2 Evolution of the Neutron Spin Structure Moments using a 3He Target", Phys. Rev. Lett. **92** 022301 (2004).

[138] K. Slifer *et al.*, (The Jefferson Lab E94-010 Collaboration), "He-3 Spin-Dependent Cross Sections and Sum Rules", Phys. Rev. Lett. **101**, 022303 (2008) [arXiv:nucl-ex/0803.2267].

[139] P. Solvignon *et al.* [Jefferson Lab E01-012 Collaboration], Phys. Rev. Lett. **101**, 182502 (2008) [arXiv:nucl-ex/0803.3845].

[140] Patricia Solvignon, "Measurement of the 3He Spin Structure Functions in the Resonance Region: A Test of Quark-Hadron Duality on the Neutron," Ph.D. diss., Temple University (2006).

[141] S. A. Kulagin and W. Melnitchouk, Phys. Rev. C **77**, 015210 (2008) [arXiv:nucl-th/0710.1101].

[142] M. Anghinolfi *et al.*"The GDH Sum Rule with Nearly-Real Photons and the Proton g_1 Structure Function at Low Momentum Transfer," CLAS Proposal PR-03-006 (2003).

[143] `http://clasweb.jlab.org/physicsdb/`

[144] K. Abe *et al.*, "Measurements of $R = \sigma_L/\sigma_T$ for $0.03 < x < 0.1$ and fit to world data." Phys. Lett. **B452** 194 (1999).

[145] S. Kuhn, "Model for the Asymmetry A_2." Technical note (2001).

`http://www.jlab.org/Hall-B/secure/eg1/Models/A2technote.ps`

[146] G. Adams *et al.*, "CLAS detector", Preprint submitted to Elsevier Science, July 15, (2002).

[147] R.M Gibbons, D.I Nathan, "Thermodynamic Data of Helium-3", Tech. Report AFML-TR-67-175, Air Force Materials Laboratory, October 1967, Reproduced by U.S. Department of Commerce.

[148] D. Lawrence, M.D. Mestayer, "CLAS Drift Chamber Calibration Procedures," CLAS-NOTE **1999-011** JLAB (1999).

[149] A.V. Klimenko "Electron Scattering from a High Momentum Neutron in Deuterium," Ph.D. diss., Old Dominion University (2004)

[150] J.M. Musolf *et al*, Phys. Rep. **239**, 1 (1994).

[151] Peter Renton, *Electroweak Interactions: An Introduction to the Physics of Quarks and Leptons* Cambridge University Press, 1990.